A deep, multi-epoch X-ray analysis of the unobscured Seyfert 1 galaxy HE 0436-4717

by

Kirsten Bonson

A Thesis Submitted to
Saint Mary's University, Halifax, Nova Scotia
in Partial Fulfillment of the Requirements for
the Degree of Master of Science in Astronomy
(Department of Astronomy and Physics)

August 26$^{\text{th}}$, 2013; Halifax, Nova Scotia

Approved: Dr. Luigi Gallo (Supervisor)

Approved: Dr. Roby Austin (Examiner)

Approved: Dr. Robert Thacker (Examiner)

Date: August 26$^{\text{th}}$, 2013

"I can say I am a scientist. I find excitement in discovery. The excitement is not in the fact that you've created something, but that you have found something beautiful that's always been there. So scientific stuff affects every part of my life... Because I'm an integrated person and I can't tell you whether for instance my skepticism is the reason I am interested in science or my science is the reason I am skeptical. Those things are impossible. But I want to know what is true. That is why I look into things. To see and to find out what is going on."

∼Richard Feynman

(*Feynman's Rainbow* by L. Mlodinow)

Acknowledgements

I would like to thank my adviser, Dr. Luigi Gallo, for his support and admirable patience these last two years. It has been quite an adventure and I am sincerely looking forward to working together in the future. Dr. Robert Thacker and Dr. Roby Austin have my gratitude for taking the time to read, edit, and discuss this work as my panel members. I would also like to thank Dr. Dirk Grupe for kindly providing the processed *Swift* data and Dr. Ranjan Vasudevan for generously sharing his SED plotting technique.

Thank you Faculty of Graduate Studies (FGSR) at Saint Mary's for funding this research and big thanks to Shane Costantino for supplying forms, food, and calm reassurances.

I also would not have had this opportunity without the support of my family and friends. I will be forever grateful for the love and laughter given to me by my Bonson clan, and no little thanks goes to the Lorentz family for their kinds words and encouragement.

I would like to thank my brothers, Al and Pat, especially for their inspiring discussions and general science shenanigans. You two will do great things and I am thoroughly enjoying watching you take on the world. Brad Lorentz also deserves my deepest thanks for his support – on so many levels – throughout this process. Thank you Brad, for helping me keep my sanity: it worked. Bazinga!

Contents

List of Figures

List of Tables

Abstract

A deep, multi-epoch X-ray analysis of the unobscured

Seyfert 1 galaxy HE 0436-4717

by Kirsten Bonson

This work presents a deep analysis of HE 0436-4717: a "bare" Seyfert 1 galaxy with strong variability and moderate soft excess. Data included a 200 ks observation with *XMM-Newton* EPIC instruments, a *Swift* BAT detection up to 100 keV, and multi-epoch observations with both *Chandra* and the *XMM* slew. The multi-epoch, multi-band spectra spanned from the optical up to X-ray regime and provided an unprecedented look at the object. We performed X-ray and broadband spectral fitting along with spectral variability analysis. Both a partial covering absorption model and a blurred reflection interpretation describe the 0.5 - 10.0 keV data statistically well. However, timing studies and model extrapolations favor the blurred reflection scenario. However, blurred reflection requires a very low iron abundance in HE 0436-4717. We consider the possibilities that this is an artifact of the fitting process, but it seems possible that it is intrinsic to the object.

August 26^{th}, 2013

Chapter 1

Introduction

1.1 Active Galactic Nuclei

Active galactic nuclei (AGN) are some of the most exotic astronomical objects in the Universe. They have become the focus of an increasing number of scientific publications since their discovery in 1943, when Carl Seyfert first reported observing some galaxies with very bright nuclei and broad optical emission lines (Seyfert 1943). Despite the now substantial field of AGN astronomy, there continue to be many characteristics, dynamics, and even simple geometry that elude full understanding.

Observations of stellar and gas kinematics have shown that the centers of most galaxies contain a supermassive black hole (SMBH) with masses ranging from around 10^6 - $10^9\,\mathrm{M}_\odot$ (e.g. Kormendy & Richstone 1995, Magorrian et al. 1998, Schödel et al. 2002, Ghez et al. 2003). The mass of a central black hole has been shown to scale with the bulge properties of its host galaxy. The luminosity (Marconi & Hunt 2003), mass (Häring & Ricks 2004), and stellar velocity dispersion (Tremain et al. 2002) of a classical bulge have the strongest correlations to black hole mass and so a coevolution between the central SMBH and host galaxy seems very likely.

Stellar-mass black holes have also been observed in black hole binary (BHB) systems located in the Milky Way (Fender & Belloni 2012), in globular clusters (Sippel & Hurley 2012), and in the

nearby galaxy M31 (Middleton et al. 2013). With masses ranging from a few to tens of solar masses, the properties of stellar-mass black holes are similar to their supermassive analogues, but will not be discussed in detail here.

If matter is in the process of being gravitationally attracted and accreted onto the SMBH, the black hole is said to be active and will be surrounded by an optically thick, geometrically thin disk of gas described by Shukura & Sunyaev (1973). The Shakura-Sunyaev or "standard" accretion disk is thought to extend to an innermost stable circular orbit (ISCO) defined as the closest distance to the SMBH that material can complete a closed orbit. Within the ISCO, the disk begins to disperse under the extreme forces exerted by the black hole and the material effectively freefalls across the event horizon. Together, the SMBH and accretion disk form the foundation of an AGN's central engine. This central engine drives the extreme behavior manifested over a wide range of spatial scales and energies.

Not all galaxies are active and even AGN can look deceptively similar to bright distant sources such as stars, galactic star forming regions, or X-ray transients. The last few decades of study and technological advances have provided ways of distinguishing AGN and despite the wide variety of AGN, there is a collection of characteristics (i.e. observation angle, presence of radio jets) that hold true for most of these objects.

AGN are the observable consequences of black hole and accretion disk dynamics and thus they exhibit very high luminosities ($10^{42} - 10^{48}\,\mathrm{erg\,s^{-1}}$ or up to 10^4 times greater than that of a galaxy) originating from extremely small volumes ($\sim$10 pc across compared to $\sim$30 kpc Galactic diameter). The efficiency of accretion is governed by the "compactness" ($\mathrm{M_{BH}}$ / $\mathrm{R_s}$, where $\mathrm{R_s}$ is the Schwarzschild radius or radius surrounding non-rotating black hole) and thus an accretion disk around a black hole is the most efficient mechanism in the Universe for converting matter into energy. The efficiency can be as high as about 6% for non-spinning SMBHs (Davis & Laor 2011); in comparison, the nuclear fusion reactions in stars limit the efficiency to around 0.1%. AGN also have signature broadband emission that continues strong over ten orders of magnitude in energy: from radio to gamma rays. Such emission can also be quite variable and often found to be weakly

polarized. Many AGN have bolometric luminosities that simply overwhelm the radiation of the host galaxy (i.e. quasars). These traits, among others, allow AGN to be differentiated from other objects.

Surveys such as the optical Sloan Digital Sky Survey (SDSS, 2000-present) have provided the identification of an unprecedented number of AGN (e.g. Adelman-McCarthy et al. 2008, Anderson et al. 2003, and Fan et al. 1999). The SDSS online archive[1] alone now has over 120,000 quasars on record. The abundance of data has led to further growth in the field and interest in these powerful objects. Nowhere else in the Universe can one observe environments of such extreme temperatures, luminosities, and gravitational forces.

Figure 1.1: An example of an AGN in the radio galaxy Centaurus A or NGC 5128. This composite radio and optical image illustrates the vast distances covered by such radio jets – which seem to be launched within a few tens of gravitational radii (Urry 2003) and can reach galactic scales. NGC 5128 is classified as a Type II radio loud quasar according to the AGN unifying classification scheme (see Table 1.1). Image credit: NASA/CXC/CfA (X-ray); MPIfR/ESO/APEX (submillimeter); ESO/WFI (optical).

[1] www.sdss.org

1.1.1 Classification

One of the characteristics that makes AGN so attractive also makes them some of the most difficult objects to analyze: they can be both geometrically and physically complex. In addition to the ubiquitous black hole, an accretion disk, and a powerful primary X-ray emitter, the inner workings of an AGN can include regions with both ionized and neutral absorbers, a toroidal-shaped cloud of gas and dust surrounding the furthest reaches of the engine, and possible radio jets known to reach kiloparsec scales (see Fig. 1.1). If and when these components are present in any individual AGN can be difficult to predict. Several distinct classifications have been developed based on such components and observed behavior (see Table 1.1).

There are a number of AGN classes with a wide variety of observable characteristics. These characteristics are rather general since there are more than a few objects exhibiting features that fall in between classes, but they do well in outlining the basic distinctions of AGN as a whole. Type I Seyfert galaxies, for example, display both broad and narrow optical emission lines while the optical spectra of Type II Seyfert galaxies have only narrow features. There are also radio-loud and radio-quiet objects, with many radio-loud AGN exhibiting jets of synchrotron radiation that are ejected along the black hole axis of rotation. Radio loudness is defined as $R = F_{5\,\mathrm{GHz}} / F_{\mathrm{B}}$ (Kellerman et al. 1989) where $F_{5\,\mathrm{GHz}}$ is the flux density at 5 GHz and F_{B} is the B-band flux density at 4400 Å. Objects with $R > 10$ are considered "radio-loud" and even radio-quiet AGN emit some radio emission, although most AGN are jet-less and classified as radio-quiet.

1.1.2 The Unified Model

A question arising from AGN classification addressed why some objects have only narrow optical/UV emission lines. Rowan-Robinson was one of the first to suggest that Type II AGN were simply obscured Type I based on his work with Seyfert 2 galaxies. In his 1977 paper, Rowan-Robinson observed that Seyfert 2 galaxies have more dust emission than Seyfert 1s with comparable optical luminosity. Optically thick dust – such as that in a toroidal cloud – could block

Table 1.1: Classification of active galactic nuclei (AGN) with some *very general* characteristics.

Class	**Subclass**	**Radio Loud**	**Optical / UV Emission Lines**	**Other Features**
Low-ionization Nuclear Admitting Region	N/A	no	narrow, low-ionization	similar to low-luminosity Seyfert 2 galaxies, may in fact be starburst or HII region emission
Seyfert	Type I	no	broad + narrow	primarily found in late type galaxies, strong X-ray emission, quite variable
	Type II	no	narrow	same as Type I Seyferts except weaker, non-variable X-ray emission
Quasars	Radio-Quiet (QSO)	no	broad + narrow	strong in X-rays, weakly polarized, variable – considered high-luminosity end of Seyfert 1 galaxies
	Radio-Loud (QSR)	yes	broad + narrow	weaker X-ray emission and polarization than QSOs, variable
Ultra-Luminous Infrared Galaxies	N/A	yes	heavily absorbed / obscured	Type II QSO candidates – the high-luminosity end of Seyfert 2 galaxies, redshifted starburst galaxies, or both
Radio Galaxies	Broad-Line (BLRG)	yes	broad + narrow	primarily found in early type galaxies, weakly polarized, variable
	Narrow-Line (NLRG)	yes	narrow	same as BLRGs except no polarization and not variable
Blazars	BL Lacertae (BL Lacs)	yes	almost none	primarily found in early type galaxies, strongly polarized, very rapid variability
	Optically Violently Variabile Quasars	yes	broad + narrow	same as BL Lacs except much more luminous

the broad emission lines in Type II AGN, leaving only the observed narrow features. This scenario became the foundation of the Unified Model that continues to be championed and challenged to this day.

A number of publications from the late 1970's onward attempted to tackle broad-line identification in Seyfert galaxies. Many studies focused on the obscuring dust (e.g. Osterbrock 1978 & 1984, Lawrence & Elvis 1982, and Ferland & Osterbrock 1986). The turning point for the Unified model came with the discovery of weak, broad emission lines in the linear polarization spectrum of Seyfert 2 galaxy NGC 1068 (see Fig. 1.2; Miller et al. 1991). Although the total nuclear spectrum of NGC 1068 continued to look like that of a normal Seyfert 2 galaxy, the linearly polarized spectrum appeared to be that of a Seyfert 1 galaxy (i.e. with both broad and narrow lines, and a strong AGN continuum). Such spectra can be interpreted as a Type I AGN viewed along the plane of an obscuring dusty torus that blocks most of the broad-line emission except a small amount that is scattered into the line of sight. Dust scattering polarizes radiation and so the weak broad-line features were only seen in the linearly polarized spectrum. Similar features have been observed in other Seyfert 2 galaxies (e.g. Tran et al. 1992), adding credibility to the Unified Model. While uncertainties in the mechanisms behind radio-loud galaxies prevents a truly seemless unification of all AGN types, most researchers agree the primary classification of AGN is dependent upon viewing angle (see Fig. 1.3).

Seyfert 1 galaxies in particular are excellent objects in which to study the innermost regions of AGN because of the fortuitous line of sight to the central engine. The central emission from Seyfert 1 galaxies is minimally impacted by jet activity, accretion disk winds, patchy warm absorbers, hot spots, and other spectral anomalies. Broadly speaking, Seyfert 1 galaxies provide the best conditions for central engine analysis right down to the ISCO.

1.1.3 Geometry

The radiation comprising the AGN spectrum is a composite of emission from a variety of processes originating at a range of distances from the central black hole. In the Type I AGN scenario,

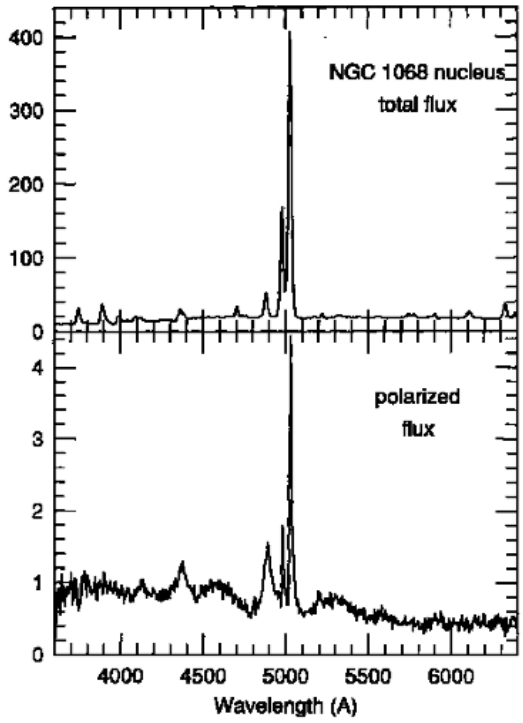

Figure 1.2: Direct (upper) and polarized (lower) optical spectra from the Seyfert 2 galaxy NGC 1068. The broad lines that can be seen in the polarized spectrum indicate the Type I/II classification of AGN is dependent upon viewing angle. Type II objects have Type I nuclei whose broad lines are obscured by a dusty torus in the line of sight. Image credit: Miller, Goodrich, and Mathews 1991.

emission passes directly from the central core through an area of optically-thick gas known as the Broad-Line Region (BLR) where photoionization and recombination will produce optical features such as Hα and Hβ Balmer lines (see Peterson 2006 for a review). These broad emission lines are created by allowed atomic transitions only and are variable on timescales of less than a month for typical Seyfert 1 galaxies. Variations in the lines have been seen to follow continuum fluctuations – a delay induced by the light travel time across the BLR (Clavel et al. 1990). Measurements of the light travel time constrains the size of the BLR itself which has been shown to be as small as $\sim$1/2 pc up to several parsecs depending on the luminosity of the object. The broad nature of the lines indicate that the region lies within the gravitational potential well of the SMBH.

From the BLR, central engine emission will continue further out through the Narrow-Line Region (NLR): an area similar to yet distinct from the BLR. Optical emission lines produced in

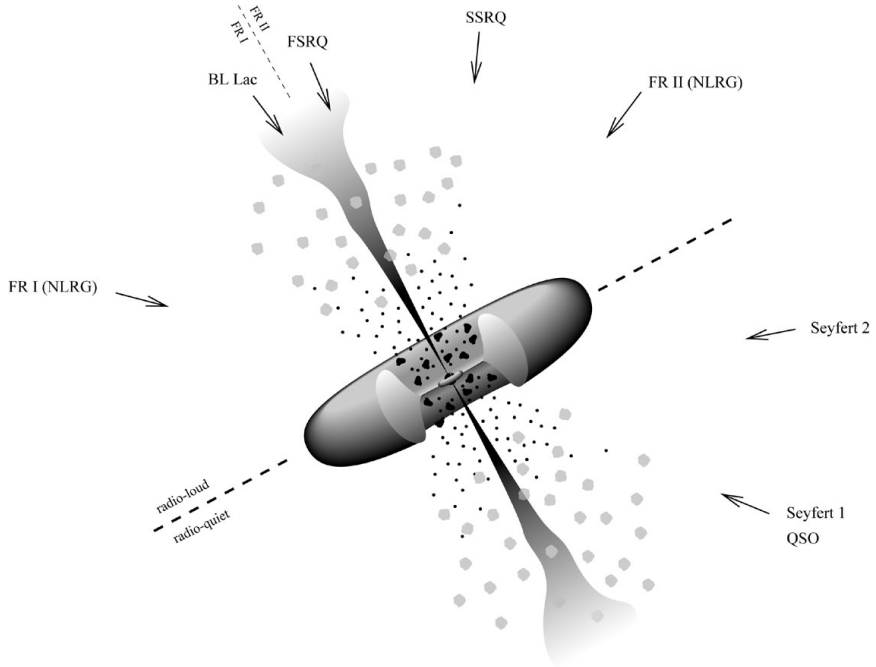

Figure 1.3: The central engine geometry of AGN according to the Unified Model. The line of sight with respect to the torus will dictate the type of AGN observed. Type I AGN are viewed at shallower observing angles near the axis of rotation. Type II AGN are viewed at angles near the plane of the torus that obscures the central engine. HE 0436-4717 is a Type I Seyfert galaxy (i.e. Seyfert 1 galaxy). Note that not all AGN have jets and that the diagram is not to scale. Image credit: *Active Galactic Nuclei* by Krolik.

the NLR may be both permitted and forbidden (e.g. [O III]λ5007) indicating the NLR has an extremely low density[2]. NLR features are not variable and their narrow profiles indicate the NLR must originate from further distances from the central engine than the BLR. In the NLR, motion is governed by the host galaxy and the variability of ionizing radiation from the AGN has been diluted during its travel from the central source (Wilson et al. 1993).

Central radiation from a Type II AGN passes through the BLR as well before encountering the dusty torus on its way to the observer. The torus hides the BLR from view and absorbs/scatters some of the radiation (Fig. 1.3). The torus also appears to be opaque to soft X-rays and so AGN viewed from such an angle (e.g. Seyfert 2 galaxies) have harder X-ray spectra.

The exact natures of both the BLR and NLR are debated. It has been hypothesized that the

[2]About $10^{10}\ \mathrm{m}^{-3}$ electron density compared to $10^{16}\ \mathrm{m}^{-3}$ in the BLR (Laor 2006).

BLR is an extension of accretion disk winds or a collection of supermassive stars deep in the central engine (Peterson 2006). Radio jets and outflows have been invoked to explain the origin of the NLR (e.g. Müller-Sánchez et al. 2011, Augusto et al. 2001). Unfortunately, radio jets (if present) and the NLR in nearby AGN are the only components that current instruments are able to directly observe (Fig. 1.4). Calculations based on variability studies (e.g. Peterson 1993, Wandel et al. 1999, and Zoghbi et al. 2010) have consistently produced reduced primary emitting regions that are fractions of a parsec from the black hole, depending on mass.

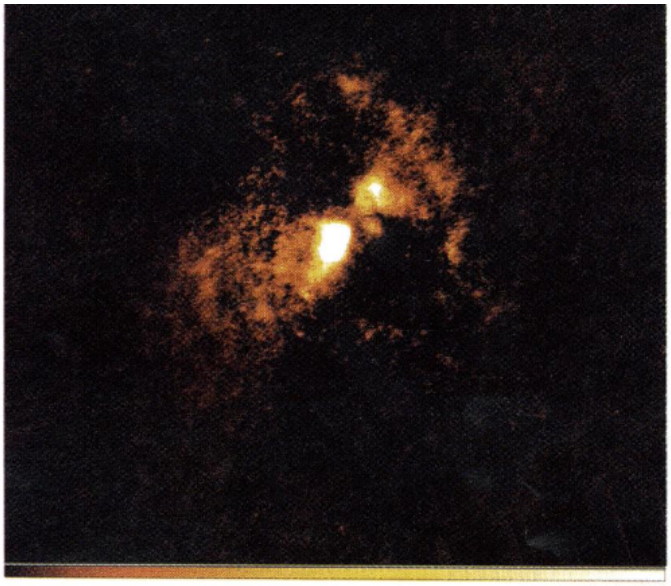

Figure 1.4: HST Hα and [N II] image of the NLR in NGC 5728. The biconical structure suggests the presence of an (unresolved) torus along the line of sight, although whether the NLR is ejected through an intrinsically spherical torus or instead a ring of dusty gas funnels the NLR into conical shapes is unkown. Image credit: Wilson et al. 1993.

1.1.4 Broadband Spectrum

The primary source of information from an AGN is its spectrum; its spectrum is used to estimate temperatures, chemical makeup, spatial scales, black hole spin, and other parameters depending on the quantity and quality of data. Different classes of AGN have their own characteristic spectra, although there are certainly those that have unusual spectral properties for their class or

exhibit as-of-yet unexplained phenomena. Using spectroscopy in conjunction with imaging and timing analysis, the physical properties of a central engine can be extrapolated despite the limits of spatial resolution and a deeper understanding of these objects can be developed.

Typical AGN emission covers nearly ten orders of magnitude in frequency in the electromagnetic spectrum and is composed of several key structures that illustrate the complex emission from these objects (Fig. 1.5). AGN are brightest in the UV-band, the wavelength at which their accretion disks intrinsically radiate. The temperature of a standard accretion disk is inversely proportional to the quarter root of black hole mass: $kT \sim 10(\dot{m}/M_8)^{\frac{1}{4}}$ where $\dot{m}$ is mass accretion rate and M_8 is black hole mass in units of $10^8\,\mathrm{M}_\odot$. The relation implies stellar-mass black hole accretion disks emit intrinsically in the X-ray while disks around the much more massive AGN emit in the UV.

The intrinsic UV radiation from an AGN accretion disk is thermal emission caused by viscosity[3] where differential rotation of the gas accreting around the supermassive black hole causes shearing friction. In the process, angular momentum is transferred outward, causing some material to fall closer to the black hole while radiating locally. As the cycle continues, a composite spectrum of thermal emission from all radii in the accretion disk forms a profile well modeled by a black body between 1 - 10 eV called the "Big Blue Bump". A smaller bump in the infrared is often seen as well and is believed to be thermal emission from dust rather than gas, radiating at a wide range of temperatures from about 50 - 1000 K. The visible dip around 1 eV is caused by sublimation of the dust at $\sim$2000 K (Sanders et al. 1989).

At energies higher than 0.1 keV, the spectrum can be well modeled by a power law of the form: $F_\nu \propto \nu^{\Gamma-1}$ where Γ is the photon index and typically has values between 0.5 - 2.0. The power law extends to higher energies, but is modified in the hard X-ray band by an excess of emission followed by a turn off around 100 keV. X-ray emission typically accounts for $\sim$10% of the total AGN emission, but variability studies suggest the X-rays originate from within light-hours of the central black hole. The following section discusses the X-ray emission in detail.

[3]The source of viscosity (i.e. molecular, dynamical) is debated.

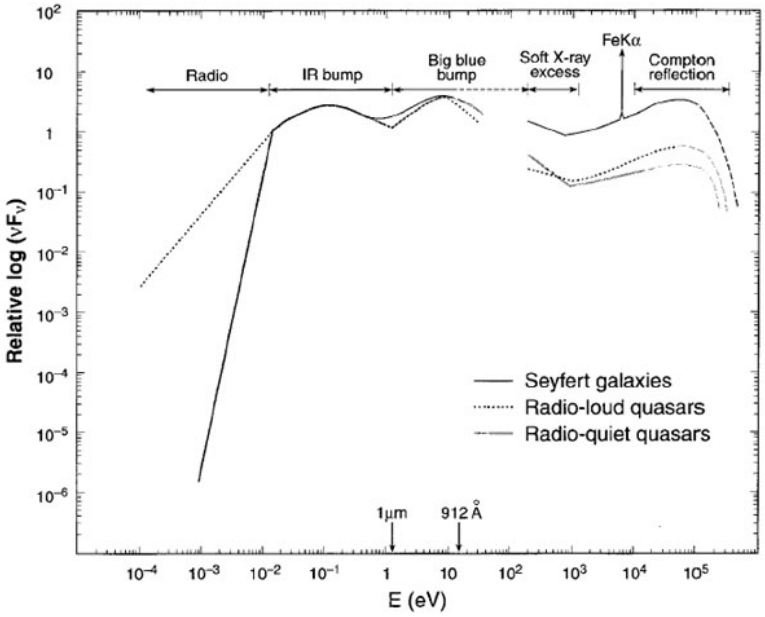

Figure 1.5: Diagram of a typical AGN broadband spectrum with features emphasized for clarity. Most AGN are radio quiet and so follow the lower soft-energy tail. The gap around 912 Å is due to neutral hydrogen absorption in the Milky Way. Image credit: Carroll & Ostlie 2007.

1.2 X-ray Spectral Components

1.2.1 X-ray Continuum

The central engines of AGN appear to include at least three related yet distinct elements: the SMBH itself, its accretion disk, and an optically thin "corona" of hot electrons from which the X-rays are thought to originate. The corona is so named because of its similarity to the upper layer of the Sun that produces the X-rays observed from the star. Several different geometries have been considered for this structure including a collection of smaller coronal clouds in a "pill box" configuration or a single extended slab of plasma that "sandwiches" the disk (Fig. 1.6). Such dispersed sources could be related to outflows or an atmosphere above the accretion disk (Reynolds & Nowak 2003). Observations suggest the most likely geometry is a variation on the "lamppost" model where the corona is a single, compact region located along the axis of rotation above the black hole and emits isotropically. This configuration may be an aborted jet (Ghisellini et al. 2004)

or some hotspot above the disk (Iwasawa et al. 2004). It is true that a perfectly homogenous and isotropic emitter is unrealistic, and the physical corona of a radio-quiet AGN is likely to be more complex (see Wilkins & Fabian 2012 for details). That being said, the quality of most AGN spectral data to date can be adequately described with the idealized lamppost model.

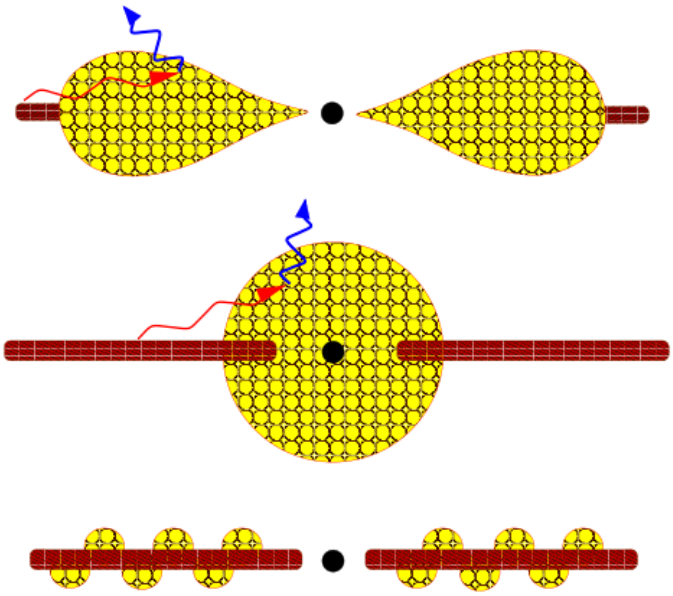

Figure 1.6: Illustrations of the possible geometries for the AGN corona: an optically thin region of plasma (yellow) that is in some orientation above the accretion disk (red). The corona Compton up-scatters intrinsic disk UV radiation (red arrows) into the X-rays (blue arrows), producing the primary X-ray emission in AGN. Image credit: Renolds & Nowak 2003.

A simple cartoon illustrating the lamppost coronal model and its relation to the black hole and accretion disk is shown in Fig. 1.7. Of these three components, only the accretion disk produces its own strong, inherent emission. As matter in the accretion disk orbits the black hole, viscosity between regions of differential rotation heats the disk and transfers angular momentum from the inner to outer radii; thus allowing matter to fall inward. This viscous heating produces the radiation emitted from the disk, seen in the UV spectrum as the Big Blue Bump (Section 1.1.4).

Some of the UV emission from the accretion disk becomes Compton up-scattered when it

interacts with the energetic electrons in the corona. After multiple collisions, the energized emission is remitted from the corona as non-thermal X-rays. Such coronal X-rays are considered the primary X-ray emission and manifest as the power law profile in high energy spectra. Assuming the corona is an isotropic emitter, some of the primary emission also gets directed back to the accretion disk and is reprocessed as the reflected spectrum.

Fig. 1.7 illustrates the AGN X-ray spectrum resulting from the potential geometry discussed. The primary emission is shown as the red power law, the reflected emission is the yellow reflection hump plus iron line, and the black curve shows the sum of the total spectral profile created by all the components.

The power law extends throughout the X-ray regime and has both a low- and high-energy turnover. The cutoff in the UV regime arises from the blackbody turnover in the disk spectrum (i.e. seed photons). The high-energy tail of the power law represents the energy cap of the coronal electrons and their inability to scatter photons of the same energy. When the power law of the primary emitter is extrapolated into the soft X-ray band an excess of emission is seen below 1 keV in most Type I AGN spectra (Fig. 1.7; left panel, blue curve). The identity of soft excess is complicated and will be discussed in later sections.

The power law continuum extends throughout the broadband spectrum, but is modified in the hard X-ray by an excess of emission before the turn off at 100 keV. This excess is attributed to a fraction of the X-ray primary emission from the central source being reflected back into the line of sight by the accretion disk – hence the term “reflection hump” or “Compton hump”. The Compton hump profile illustrates the balance between photon scattering and absorption in the accretion disk. At energies below $\sim$10 keV, any scattered light is absorbed by metals in the disk. Photoelectric absorption diminishes above 10 keV however, and the scattering dominates, appearing in the spectrum as the hump which peaks between 30 - 40 keV. Around 40 keV the Klein-Nishina limit is reached where the scattering cross section diminishes rapidly due to electron recoil (D’Onofrio, Marziani, and Sulentic 2012).

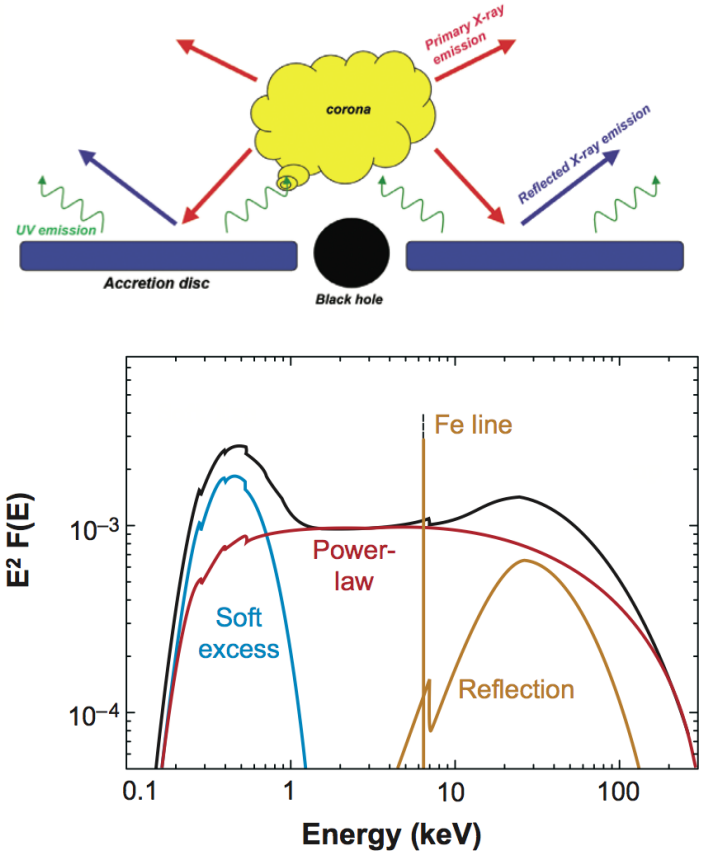

Figure 1.7: Simple illustration of AGN central engine geometry (left) and how it relates to the X-ray spectrum (right), assuming a lamppost model for the corona. Instrinsic UV emission from the accretion disk (green) becomes Compton up-scattered in the corona and remitted as primary, non-thermal X-rays (red). Some of the primary radiation gets observed directly while a significant fraction gets reflected off the accretion disk to produce thermal, softer X-rays (blue). The corona is assumed to be homogenous and isotropically emitting. Image credit: Gallo 2011 (left) and Miller 2007 (right).

As a cooler, gaseous reflector, the accretion disk is expected to contribute atomic features to an AGN spectrum and those can indeed be seen. Below 10 keV, where photoelectric absorption dominates, both emission lines and absorption edges in the spectrum are possible. The most common X-ray atomic feature caused by accretion disk reflection is the Fe Kα emission line at an intrinsic energy of 6.4 keV (Fig. 1.7). The large fluorescent yield and high cosmic abundance of iron allows it to be a prominent feature in many AGN X-ray spectra and it can be a useful tool for probing the environment close to the black hole, as will be discussed in the following section.

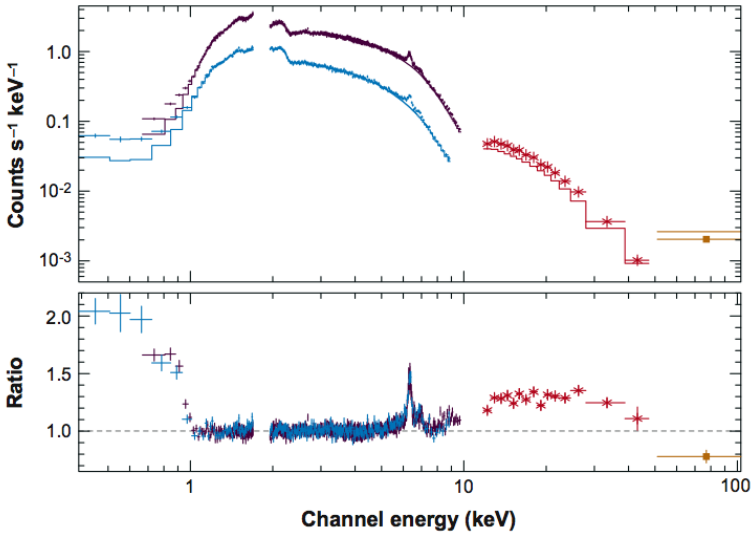

Figure 1.8: The high-energy spectrum of Seyfert 1 galaxy MCG 5-23-16 from the *Suzaku* X-ray telescope. The spectrum has been fit with an absorbed power law and the model residuals plotted beneath. The residual features show common features of AGN X-ray spectra: a soft excess below 1 keV, an iron line around 6 keV, and the Compton hump above 10 keV. Different colors correspond to different instruments. See Miller 2007 for details.

Both the primary and reflected components are nearly always observed in Seyfert 1 galaxies and the power law component typically dominates. However, many examples exist showing cases where the reflection component is stronger than the primary power law (e.g. Zoghbi et al. 2008). Model fitting can be used to determine which emission source dominates the spectrum at the time of observation and can provide valuable insight into the possible spectral state of AGN. Recent models of disk reflection (e.g. Miniutti & Fabian 2004, Wilkins & Fabian 2012) suggest that an

X-ray spectrum dominated by the reflection component could be caused by the corona migrating closer to the black hole. As the corona lowers along the axis of rotation, gravitational effects direct some of the primary (i.e. power law) photons to the black hole and accretion disk via light bending. The power law component diminishes, but more hard X-rays illuminate the accretion disk, boosting the reflected flux so that it dominates over the primary power law in the spectrum. If the corona rises back to larger heights the reflected flux lessens and the spectrum is dominated by the primary component. What would cause the corona to migrate at all remains an open question.

An example X-ray spectrum from Seyfert 1 galaxy MCG 5-23-16 is shown in Fig. 1.8. In this case, the spectrum has been fit with an absorbed power law only and the model residuals are plotted below. The residual features show an excess of soft emission below 1 keV, an Fe Kα line around 6.4 keV, and the reflection hump above 10 keV.

1.2.2 X-Ray Reflection

AGN spectra frequently sport a variety of atomic features like emission/absorption lines and absorption edges. The presence of particular features, the line ratios, and profile shapes can be used to determine composition, densities, pressure, origin, and motion of the emitting regions.

The strength and identity of emission lines observed depends on the ionization of the gas. The ionization parameter, ξ, describes the point at which the rate of photoionization is balanced by recombination: $\xi = L / nr^2$ where L is the ionizing luminosity, n the electron number density, and r the distance of the material from the ionizing source (Turner & Miller 2009).

For ξ below $100\,\mathrm{erg\,cm\,s^{-1}}$ emission lines can be seen. As ξ rises between 100 - $500\,\mathrm{erg\,cm\,s^{-1}}$, Auger destruction dominates and Fe Kα emission lines are diminished. Auger destruction diminishes at higher ionization parameters and Fe Kα lines become visible again. Finally, if ionization continues to increase, iron becomes helium- and hydrogen-like and recombination takes over as the process by which emission lines are formed. At $\xi >$ 5,000 $\mathrm{erg\,cm\,s^{-1}}$ all elements are completely ionized and emission lines will be absent (see Fig. 1.9). Thus the presence and strength of atomic features alone in AGN spectra can be used to

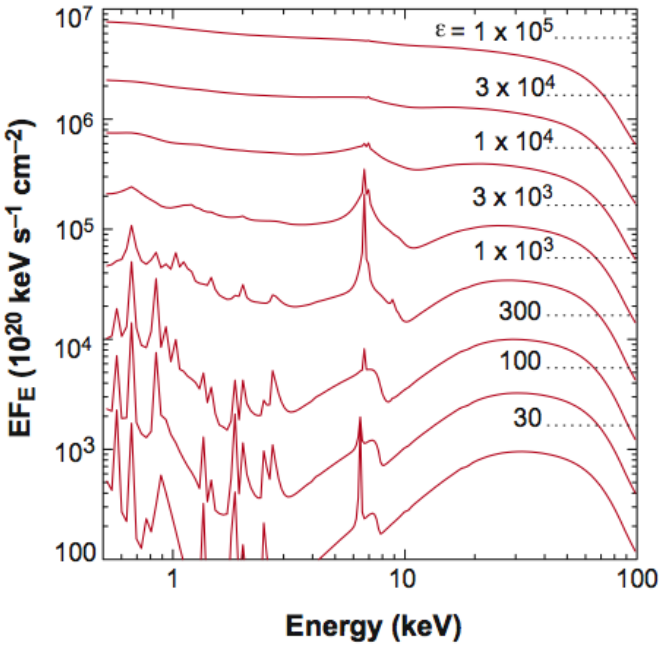

Figure 1.9: The effects of ionization on the reflection spectrum of an accretion disk. As the ionization parameter, ξ, rises Auger destruction dominates and emission lines diminish. The lines strengthen again around $\xi = 10^3\,\mathrm{erg\,cm\,s^{-1}}$ before recombination becomes the primary mechanism for emission lines before the features fade entirely as all elements become completely ionized and no photoelectric absorption is possible. Image credit: Miller 2007.

determine gas temperature, ionization, and atomic abundance.

The shape of an X-ray emission line can also provide valuable information. An intrinsic emission line will be quite narrow and well defined. If the emission is coming from the accretion disk, however, the radiation will experience Doppler broadening caused by the rotation along the plane of the disk producing a symmetric, double-peaked profile dependent on the observing angle. At smaller radii the disk material begins to move at a significant fraction of the speed of light and disk radiation will be beamed as the emitter rotates towards the observer and dimmed as it rotates away. At these closer radii the light also begins to feel the influence of the gravitational potential well and is redshifted. If the emission line is produced within a few gravitational radii ($\mathrm{R_g}$ = *GM* / c^2) of the ISCO, it will experience strong general relativistic redshifting (see Fig. 1.10).

Depending on where it originates in the disk, a line profile can be substantially modified. Thus,

light from the innermost regions of an accretion disk may be identified and analyzed based on the degree of "smearing" an observed feature may exhibit. One must keep in mind, though, that an accretion disk radiates across its entire surface – from the innermost regions to the outer edges – and so any emission, whether inherent or reflected, will actually be a composite of radiation over a range of radii. It is difficult to resolve individual atomic features since broadening can blend multiple features together.

1.2.3 Absorption Effects

Radiation from the central engine passes through many regions of gas and dust with varying degrees of density and temperature before finally reaching the observer. The primary X-ray emission may be absorbed and reprocessed many times throughout its journey, not only by the accretion disk but possibly by the BLR and NLR, the torus, by dust and gas from both the host galaxy and the Milky Way, and more. Assuming the primary emission is relatively isotropic, absorption is only visible along the line of sight and so absorption features seen in spectra are heavily dependent upon geometry. Since oxygen is the most abundant element in the soft X-ray band below $\sim$1 keV, common features include O VII and O VIII K absorption edges around 0.74 and 0.87 keV, respectively. Warm or ionized absorbers are also common in many AGN and add additional complexity to both the broadband and X-ray spectrum (e.g. Halpern 1984, Netzer 2008).

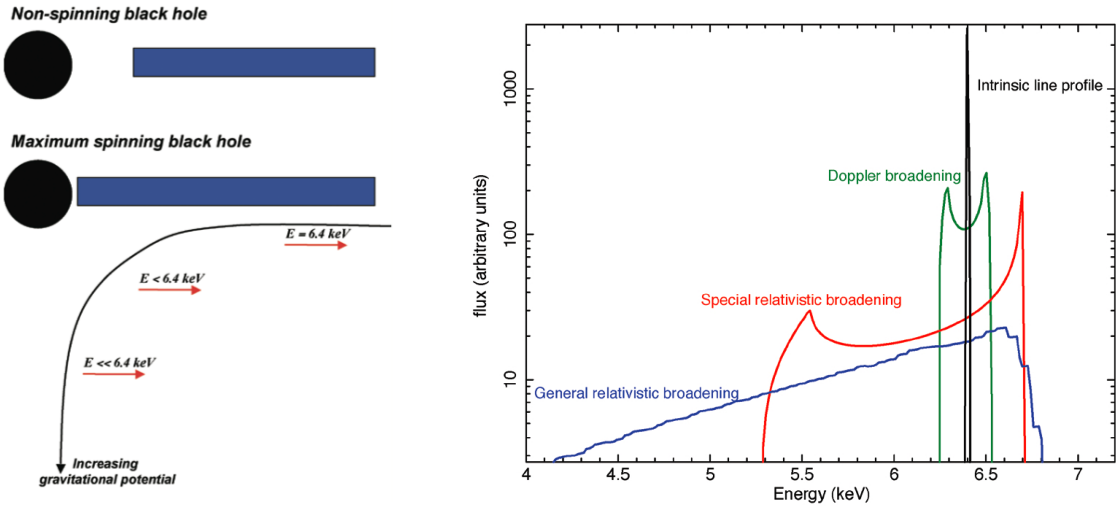

Figure 1.10: The possible broadening effects on an intrinsic Fe Kα emission line due to accretion disk rotation and the distance from the central supermassive black hole. *Left*: Radiation from closer radii is heavily redshifted as it originates deeper in the black hole's gravitational potential well. In some cases, radiation may come from only a few R_g away as the ISCO also extends to closer radii in spinning black holes. *Right*: an intrinsic line profile (black) experiences Doppler broadening (green), special relativistic broadening (red), and general relativistic broadening (blue) based on the radius of its origin. These models illustrate the changes to a single line, the source of which is located at a specific radius along the accretion disk; a true disk spectrum would be a composite of lines from a range of radii. Image credit: Gallo 2011.

1.2.4 The Soft Excess

The nature of the soft excess is vehemently debated. Both ionization and absorption effects have been used in attempts to explain the feature in AGN X-ray spectra. The black body-like profile of the excess initially suggests it is thermal emission from the disk, i.e. the high-energy tail of the Big Blue Bump extending into the observable soft X-ray band. However, the absence of the luminosity-temperature relation (Porquet et al. 2004) indicates the origin of the soft excess is not black body emission (Fig. 1.11). Photon trapping in a super-Eddington slim disk has been suggested to account for the temperature difference (Mineshige et al. 2000 and Gallo et al. 2004) although the discrepency remains too high.

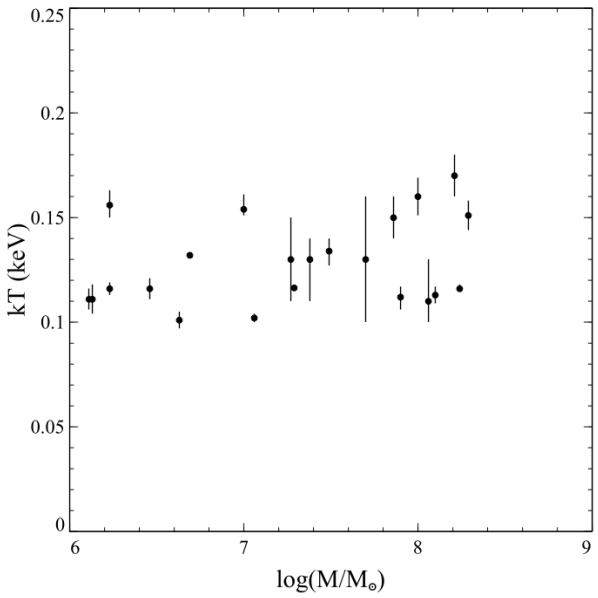

Figure 1.11: The soft excess black body temperature in relation to black hole mass for a sample of Type I AGN. Despite a range of 3 orders of magnitude in M_{BH}, the soft excess temperature changes by less than 50%. This indicates the origin of the soft excess is not black body emission from a standard accretion disk. Figure credit: Crummy et al. 2006, Fig. 3.

The fact that this component is relatively invariable and remains at a constant energy over a wide range of M_{BH} suggests atomic processes could be responsible. Atomic features would be seen at constant energies dependent only upon the intrinsic radiation energy and the ionization and density

of the source material. If the features were then smeared in some way – either through high velocities along the line of sight or through relativistic effects – the collection of features would be blended to produce the smooth hump. Whether these atomic features arise from absorption (e.g. Gierliński & Done 2004) or reflection (e.g. Crummy et al. 2006) has proven very difficult to determine.

Blurred Absorption

In the absorption scenario, moderately ionized material absorbs the primary X-ray continuum and reduces the flux substantially in the intermediate energy range. This produces an apparent excess at soft energies when the hard X-ray power law is extrapolated redward (see Fig. 1.12). If this material is attributed to outflowing accretion disk winds, turbulent velocities will smear out individual spectral features creating the soft excess. High velocity winds have been observed in AGN and stellar mass black holes (King et al. 2013).

Absorption models have fit many AGN spectra well (Middleton et al. 2007) and warm absorbers are reportedly seen in up to 40% of Type I AGN (Cappi et al. 2009), although they are not without challenges. Assuming the standard accretion disk model, the absorbing material must be strongly relativistic with an accretion rate compared to at *least* the Eddington rate to smooth atomic features enough to match observations. In addition, the material would need to be in total pressure equilibrium to keep the soft excess constant over time and consistent from object to object. Such extremes may be possible in a few cases, but is unlikely for the majority of AGN where a soft excess is observed. An alternative theory allows for a lower accretion rate and slower velocities, but requires instead an inhomogenous accretion flow with close to spherical geometry – unlikely conditions for the accretion disk based on current understanding (Chevallier et al. 2006).

Blurred Reflection

The reflection interpretation of the soft excess requires an optically thick emission source (i.e. the accretion disk) rather than an optically thin absorber. The presence of a Compton hump $\gtrsim$ 20 keV in many AGN spectra suggest the soft excess could be the lower energy part of the reflection

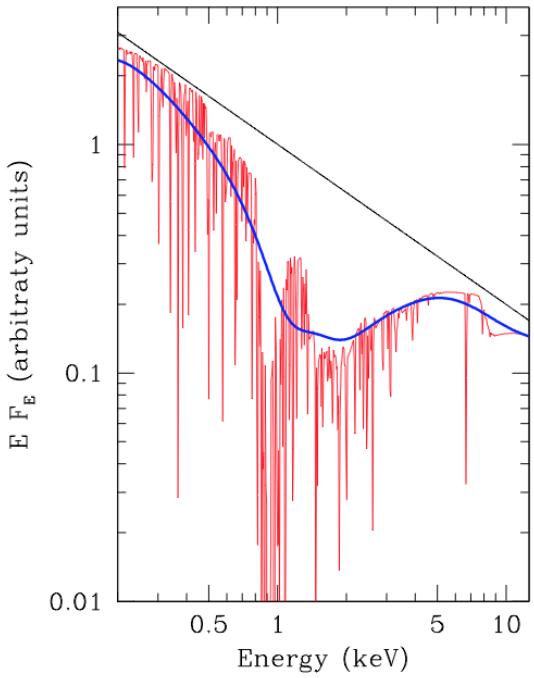

Figure 1.12: A model spectrum illustrating how ionized absorption could produce the soft X-ray excess. The thin black line represents the primary power law component and the red line shows absorption features predicted by XSTAR model with hydrogen column density $N_{\rm H}$= $33\times10^{22}\,{\rm cm}^{-2}$ and ξ = $460\,{\rm erg\,cm\,s}^{-1}$. The blue line is the profile of the absorption features convolved with a Gaussian component. Details can be found in Gierliński & Done 2004, Fig. 2.

spectrum. As seen in Fig. 1.9, at low levels of ionization there are several strong reflection features below $\sim$2 keV. The emission lines must originate in compact regions under strong gravitational effects that smooth the profile. Relativistic blurring of the reflection component can thus generate a soft excess in the spectrum (see Fig. 1.13).

The extreme nature of the soft excess in this case requires that the disk be far from hydrostatic equilibrium (Middleton et al. 2007) and reflection alone limits the soft excess flux to less than that observed in most AGN with this feature (Chevallier et al. 2006). However, the inner radii of the accretion disk are deep enough into the black hole potential well that gravitational light bending is expected to occur (Miniutti & Fabian 2004). Following the null geodesic, emission from the isotropic primary X-ray source will bend along curved spacetime and illuminate the accretion disk

at closer radii. As seen by the observer, such light bending results in an anisotropic primary emitter and enhanced reflection from the inner disk.

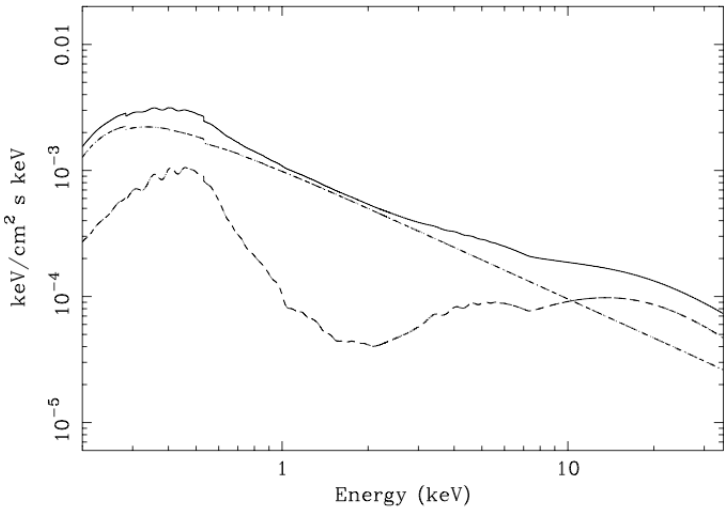

Figure 1.13: An example of a reflection model accounting for the soft excess in an AGN spectrum. The dashed line is the reflection component which includes both the soft excess $\lesssim$4 keV and the smaller Compton hump above 10 keV. The primary X-ray component is the dot-dashed line and the solid line is the total model profile. Small dips at lower energies are due to Galactic absorption. Type 1 AGN PG 1202+28 was the object being examined in this case. Figure credit: Crummy et al. 2006, Fig. 13.

Comptonization

Both the absorption and reflection models for the soft excess have faced criticism for their extreme scenarios. As exotic objects, one could argue that the innermost regions of AGN could quite reasonably be extreme places, but nevertheless alternative theories have also been tested that interpret the soft excess as a completely separate spectral component.

Walter & Fink (1993) were one of the first to suggest a second, cooler Comptonizing region that would scatter the intrinsic UV emission into the soft X-ray regime just as the hotter corona scatters the UV emission into the hard. The morphology of this cooler Compton component is debated. Magdziarz et al. (1998) suggested a transitional area between the traditional optically thick disk and an optically thin inner region. Janiuk et al. (2001) prescribed a “warm skin” on the accretion disk

based on their study of quasar PG 1211+143. Done et al. (2012) point out that it would be difficult for either of the two scenarios to keep the soft excess at constant temperature, as is observed. Instead, they suggest the cooler Compton component resides in the accretion disk itself as a consequence of increased dissipation in the upper layers. The soft X-ray spectrum of an AGN would thus be a combination of the tail end of intrinsic disk emission from larger radii, the primary X-rays from the hot corona, and the softer X-rays from the disk at smaller radii (see Fig. 1.14).

A second, cooler Compton region has been used to explain the soft X-ray spectra observed in a handful of objects so far (Done et al. 2012, 2013; Zhong & Wang 2013) and as the models develop further they will prove valuable in helping to constrain the nature of the soft excess as well as that of AGN accretion disks.

1.3 Seyfert 1 Galaxy HE 0436-4717

HE 0436-4717 (hereafter HE 0436) appears to be a rather typical Seyfert 1 galaxy at $z = 0.053$ first observed by the Einstein Slew Survey in 1992 (ESS, Elvis et al. 1992). It has been included in numerous surveys and catalogues since the ESS including: the *ROSAT* All-Sky Survey (Grupe et al. 1998), the Hamburg/ESO Survey for bright QSOs (Wisotzki et al. 2000), and the Palermo Swift-BAT Hard X-ray Catalogue (Cusumano et al. 2010) (e.g. see Table 1.2). Despite its frequent inclusion in such wide-field studies, HE 0436 has been the subject of deep analysis in only two publications.

Halpern & Marshall (1996) monitored the object in the extreme UV with the *EUVE* satellite for 20 continuous days and were able to produce an unusually long light curve. Their timing analysis of the light curve revealed possible flaring with a period of about 0.9 days. In addition, the authors also analyzed spectra from *EUVE*'s short-wavelength spectrometer and found no emission line features in the 70 - 110 Å range. The column density listed in that work is comparable to Galactic extinction alone, indicating no intrinsic extinction in the object was observed.

The second deep analysis of HE 0436 was done by Wang et al. (1998) using data from *ASCA*

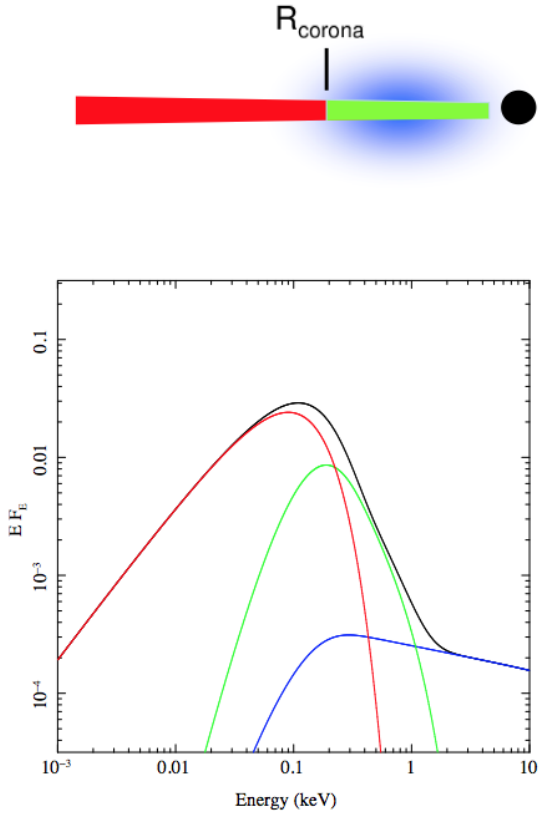

Figure 1.14: The geometry (top) and corresponding model spectrum (bottom) for the possible cooler Compton component soft excess source. Emission from the accretion disk at larger radii (red), the primary X-ray component (blue), and the cooler Compton component (green) together form the broad band spectrum. The accretion disk transition radius is labeled $R_{\rm corona}$ and the corona is shown as the sandwich model. Figure credit: Done et al. 2012, Fig. 5.

and *ROSAT* observations. The authors found the 0.4 - 10.0 keV spectrum was well modeled by a single power law with slope of $\Gamma = 2.65 \pm 0.20$ or by a sum of a $\Gamma = 2.85 \pm 0.20$ power law convolved with a weak black body of temperature $\sim$146 eV. The authors describe also finding an Fe Kα feature with an equivalent width of around 430 eV and two absorption edges: one at $E \sim 0.28$ keV with an optical depth of $\tau \sim 0.26$ from the *ROSAT* spectrum, and one at $E \sim 0.83$ keV with $\tau \sim 3.46$ from the *ASCA* – the latter of which was attributed to a combination of O VII and O VIII edges. The paper also mentions a multi-epoch comparison between *ASCA* observations 4 months apart, where a 47% flux change was seen. However, aside from the change in flux, all other spectral parameters remained constant.

In this study, HE 0436 was observed independently by the *XMM-Newton*, *Chandra*, and *Swift* observatories at epochs between 2002 - 2013. The combined analysis of these data is presented here as the deepest investigation of this object to date using the most current instruments and analysis tools.

Following this introductory section, Chapter 2 offers a brief history of X-ray astronomy and explains the data processing used in this work for all instruments. An initial broadband spectral analysis of the *XMM-Newton* EPIC data can be found in Chapter 3, including a more detailed look at the 3 - 10 keV band. Spectral analysis was extended into the UV band in Chapter 4 with $\alpha_{\rm ox}$ calculations and spectral energy distribution (SED) modeling using *Swift* data. Chapter 5 describes an in-depth X-ray analysis of the *XMM-Newton* MOS spectra, including extensive absorption (Sec. 5.2) and reflection (Sec. 5.3) model fitting. Chapter 6 details the timing analysis of the *XMM-Newton* light curves and specifically examines hardness ratios (Sec. 6.2), fractional variability (Sec. 6.3), and flux-resolved spectra (Sec. 6.4). Discussion and concluding remarks in Chapter 7 complete this work.

Table 1.2: HE 0436-4717 X-ray Observation History.

Observation	**Designation**	**Exposure (s)**	**Reference**
ROSAT All-Sky Survey	RX J0437-4	649	Grupe et al. 1998
ROSAT pointed observation	RX J0437.4-4711	6142	Halpern & Marshall 1996
Einstein Slew Survey	1ES 0435-472	14.1	Elvis et al. 1992
ASCA serendipidous captures	RX J0437.4-4711	24×10^3	Wang et al. 1998
XMM-Newton slew survey	J043728.0-471128	$\sim$6	Saxton et al. 2008
2^{nd} Palermo *Swift* -BAT catalogue	2PBC J0437.8-4713	$\sim 10^3 - 10^4$	Cusumano et al. 2010
Swift serendipidous capture	RXJ0437.4-4711	~ 200	N/A

Chapter 2

Observations and Data Processing

2.1 High Energy Telescopes

2.1.1 A Brief History

Any X-ray detector attempting to collect high-energy astronomical emission must escape Earth's atmosphere. The atmosphere absorbs and scatters the majority of high-energy radiation and would render any ground-based X-ray telescopes moot. E.O. Hulburt at the U.S. Naval Research Laboratory was the first to propose sending a high-energy detector into the upper atmosphere aboard a rocket in the late 1920s[1]. It soon became known that the Sun is a strong X-ray source, but it was not until 1962 that the first cosmic X-ray source, Scorpius X-1, was detected (Giacconi et al. 1962). It is now known that Sco X-1 is a low-mass X-ray binary system composed of a late-type donor star and a neutron star (Hynes & Britt 2012).

Sounding rockets continued to be used for the next decade until the first X-ray satellite was launched. *Uhuru* was not an imaging device, but used two sets of proportional counters – high-energy analogues of Geiger counters – to detect X-ray photons as they passed through the detectors (Giacconi et al. 1971). The first satellite dedicated solely to X-ray astronomy, *Uhuru*

[1] http://xweb.nrl.navy.mil

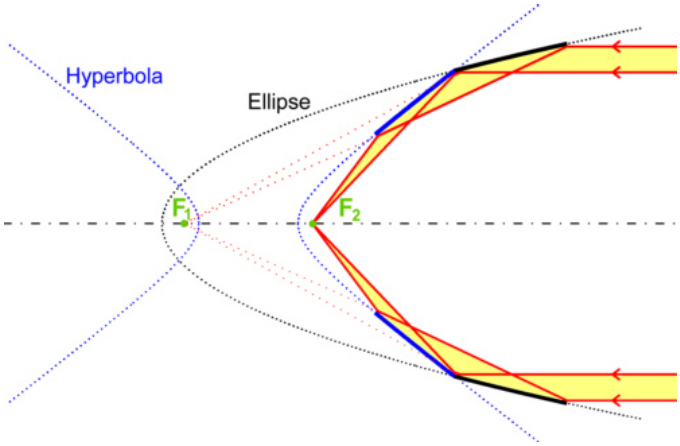

Figure 2.1: Illustration of Wolter I optics used to reflect and focus high-energy radiation for imaging. Elliptical and hyperbolic mirrors are used to provide the grazing incident angles necessary to reflect photons (about 2° or less depending on the material) while nested mirrors provide an increased effective area. Image credit: Arndt Last.

performed the first all-sky survey with an unprecedented sensitivity of $2.4\times10^{-8}\,\mathrm{erg\,cm^{-2}\,s^{-1}}$ in the 2 - 10 keV band.

The *Einstein Observatory* satellite was launched in 1978 and contained the first fully-imaging X-ray telescope dedicated to observing sources other than the Sun. *Einstein* was revolutionary in that it was the first large-scale instrument to utilize grazing incidence optics (Tucker & Giacconi 1980). Unlike lower energy optical or UV light, X-ray photons require very small incident angles for reflection, typically 2° or less depending on the reflecting material. Traditional optics will simply transmit or absorb higher-energy X-rays. The extreme incident angle causes only a small fraction of incoming light to get reflected as the grazing angle allows much of the radiation to pass by undeterred. The Wolter I optics system utilized in X-ray telescopes is composed of a set of nested mirrors used to increase effective area and capture as much of the incident light as possible (Fig. 2.1).

The effectiveness of Wolter Optics and the invention of CCD detectors both bolstered the success of X-ray telescopes. The twenty years following the launch of *Einstein* saw a boom in high-energy astronomy with instruments like *EXOSAT* (Turner & Pounds 1989), *ROSAT* (Trümper et al. 1991), and *RXTE* (see NASA's Science Highlights[2]) leading the way in AGN research. Two

[2]http://heasarc.gsfc.nasa.gov/docs/xte/Snazzy/snazzy_sci.html

telescopes launched in 1999, *XMM-Newton* (Jansen et al. 2001) and *Chandra* (Weisskopf et al. 2002), are not only still active but are workhorses in the field and continue to supply some of the highest quality X-ray data. The gamma-ray telescope *Swift* (Gehrels et al. 2004), launched in 2004, and *Suzaku* satellite (Mitsuda et al. 2007), launched in 2005, are also currently active and providing valuable observations. In this work, data from *XMM-Newton*, *Chandra*, and *Swift* are examined in detail.

2.1.2 *XMM-Newton*

The European Space Agency's (ESA) X-ray Multi-Mirror Mission (hereafter *XMM-Newton*) is the largest satellite ever built in Europe dedicated solely to science (see Fig. 2.2). The observatory flies in a highly elliptical orbit allowing for long, uninterrupted observations: its perigee and apogee are around 6,000 km and 115,000 km respectively. *XMM-Newton* carries three co-aligned, Wolter I imaging X-ray telescopes that are each composed of 58 nested mirrors with gold reflective coating and were designed to have the highest possible effective collection area over the widest range of photon energies; particular care was taken to maximize the collecting area at $\sim$7 keV. The X-ray telescopes observe calibrated energies spanning 0.3 - 10.0 keV.

Half of the incident radiation focused by two of the X-ray telescopes is diverted to reflection grating spectrometers (RGS, den Herder et al. 2001), which diffract the light before it reaches the detectors. The radiation not diverted to the RGS continues to metal oxide semiconductor (MOS, Turner et al. 2001) cameras with CCD detectors that have a combined surface area 62 mm in diameter, equivalent to 28.4 arcmin on the sky. The third X-ray telescope allows light to travel uninterrupted to a pn camera (Strüder et al. 2001) with CCDs that were specifically designed and built for *XMM-Newton* and have a combined imaging area of 36 cm^2, covering 97% of the telescope's 30 arcmin field of view. The three X-ray cameras, two MOS and single pn, make up the European Photon Imaging Camera (EPIC) system. In total, the combined instruments reach an effective area of around 2500 cm^2 at low energies depending on the filter used (see the ESA's

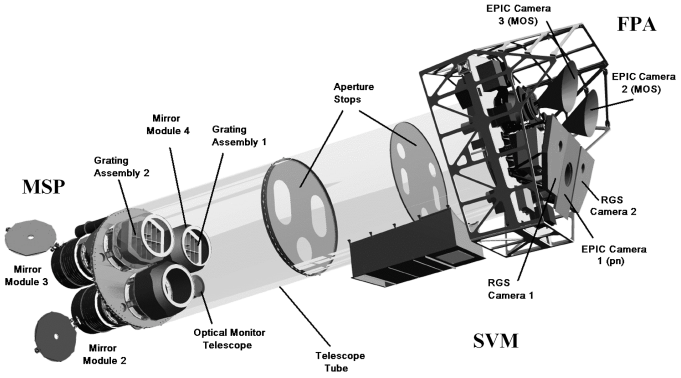

Figure 2.2: An illustration of the *XMM-Newton* X-ray satellite and its primary instruments. *XMM-Newton* contains three X-ray telescopes in addition to an optical/UV monitor with all four instruments observing simultaneously. Two of the X-ray telescopes are equipped with reflection grating spectrometers. Image credit: Lumb et al. 2012.

technical documentation for more details[3]).

In addition to the EPIC instruments, *XMM-Newton* also sports an optical/UV monitor (OM). This fourth telescope covers between 170 - 650 nm of a 17 arcmin^2 field of view. The OM is mounted alongside the X-ray instruments and is used simultaneously thus having the potential to provide X-ray, optical, and UV observations of all targets. It is this ability for simultaneous, multiwavelength observations that make *XMM-Newton* particularly useful for multiwavelength AGN astronomy.

One of the ongoing projects of the observatory makes use of the data recorded as the telescopes slew from one pointed observation to the next. The first *XMM-Newton Slew Survey* (XMMSS) was released in May 2006 and has since seen numerous updates, the most recent of which was in June 2011 (XMMSL1d5). The XMMSS is a shallow survey covering 52.5% of the sky at last count (Warwick et al. 2012), although the 2 - 10 keV band sensitivity in particular is about an order of magnitude deeper than any other dedicated all-sky surveys to date. Only data from the pn instrument is recorded in the catalogue as the MOS have longer readout times that smear the point spread function during a $\sim 90^{\circ}$/ hour slew. XMMSS observations thus range from 0.2 - 10.0 keV and exposure times vary from around 1 - 11 seconds. The catalogue had around 80 Seyfert 1 galaxies

[3]http://xmm.esac.esa.int

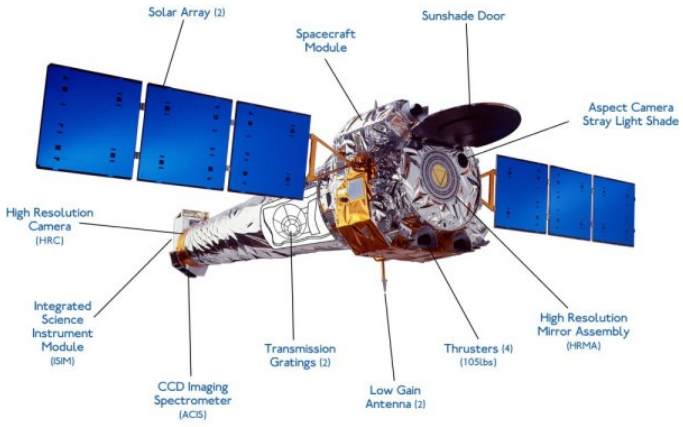

Figure 2.3: An illustration of the *Chandra* X-ray satellite with its primary instruments. *Chandra* is a single, X-ray telescope working in conjunction with four primary instruments: two detectors and two grating spectrometers. The variety of observational tools on board allow for unprecedented X-ray imaging and high- and low-energy spectroscopy. Image credit: NASA.

listed as of December 2012 and continues to provide valuable X-ray data for AGN studies.

2.1.3 *Chandra*

Chandra is the U.S. National Aeronautics and Space Association's (NASA) high energy telescope that was designed to create X-ray images in unprecedented detail (Fig. 2.3). Its single X-ray telescope uses Wolter I optics as four nested pairs of iridium-coated mirrors. Four scientific instruments work in conjunction with the telescope, two primary detectors and two grating spectrometers.

The High Resolution Camera (HRC) can be positioned at the telescope focus and is a microchannel plate with its own two unique detectors. The HRC-I is used for high-quality imaging and the HRC-S for low-energy spectroscopy. The HRC-I has the largest field of view of any *Chandra* instrument at 40 arcmin^2. The HRC in general has a maximum energy range of 0.06 - 10.0 keV and also has the highest spatial and temporal resolutions on the telescope at $<$ 0.5 arcsec and 16 ms, respectively.

The Advanced CCD Imaging Spectrometer (ACIS) can be swapped for the HRC and is used for imaging ($\sim$1 arcsec resolution) and high-energy spectroscopy. The use of CCDs in this instrument,

unlike the HRC, gives ACIS the highest intrinsic spectral resolution of the two. ACIS has a maximum energy range of 0.08 - 10.0 keV and a field of view of 16 arcmin^2 depending on the CCD array used.

One of two grating spectrometers can be placed in the path of incident light behind the mirrors and readout to either the HRC or ACIS. The High Energy Transmission Grating (HETG) is optimized for the 0.4 - 10.0 keV band and delivers high-resolution spectroscopy of bright sources. The HETG is most often used with the ACIS detector. The softer energy bands are studied using the Low Energy Transmission Grating (LETG) that has the highest spectral resolution of all the instruments and is utilized with the HRC-S. The LETG is optimized for the 0.07 - 2.0 keV band.

As the user must choose one detector and one grating spectrometer at a time, *Chandra* cannot provide simultaneous, multi-instrument observations. However, it is also in a high-Earth orbit with a perigee around 10,000 km and apogee around 139,000 km. *Chandra*'s large field of view and high spatial resolution also makes it ideal for observing massive, diffuse objects. The *Chandra* Deep Field surveys are some of the deepest observations ever obtained in X-rays, reaching up to 4 Ms in exposure time, and contributing to the identification of AGN populations (Brandt & Hasinger 2005).

2.1.4 *Swift*

NASA's other high-energy telescope was launched five years after *Chandra* and had a primary objective to detect cosmic gamma-ray bursts (GRB) as quickly as possible in order to catch their afterglows. Both pre-determined objects and targets of opportunity are observed. *Swift*, *Chandra*, and *XMM-Newton* often work in conjunction, where *Swift* will catch the initial GRB and *Chandra* or *XMM-Newton* will follow up with pointed observations as the afterglow falls from gamma into the softer X-ray bands.

Swift is a collection of three telescopes, the first being its Burst Alert Telescope (BAT) observing in the 15 - 150 keV band (see Fig. 2.4). The BAT uses a coded aperture mask instead of an optics system in order to have a large detection range and wide field of view for trigger capabilities (see

the HEASARC webpage for details[4]). As soon as a burst is detected, the BAT calculates the source position to within 1 arcmin, decides whether a burst justifies observation, and sends coordinates to the spacecraft all within a few seconds. It has been detecting about 100 GRBs a year since the launch of *Swift* in 2004.

The X-ray Telescope (XRT) onboard *Swift* covers the softer energy ranges from 0.3 - 10 keV and will be observing a source within 20 - 70 seconds of triggering from the BAT. It utilizes a Wolter I optical system with gold-coated mirrors to focus incoming X-rays onto a CCD detector, similar to the *XMM-Newton* MOS instrument. With a 23.6 arcmin^2 field of view, the images produced by the XRT are used to refine source positions for further analysis (Burrows et al. 2000).

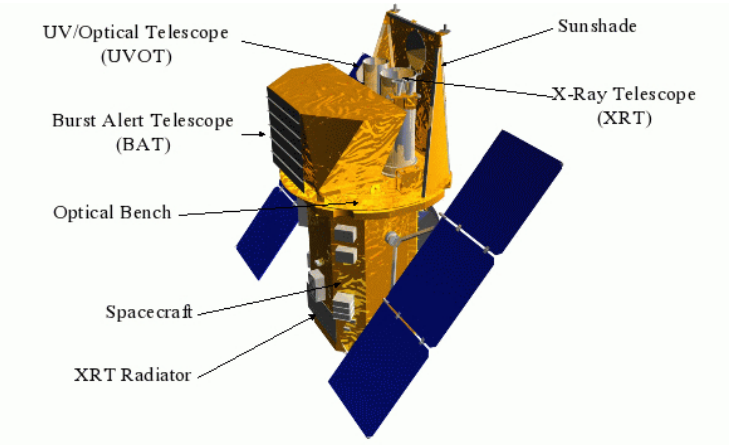

Figure 2.4: An artist's conception of the *Swift* gamma-ray satellite. Three telescopes make up the *Swift* system and cover gamma, X-ray, and UV/optical energy bands for nearly simultaneous observations across an energy range almost five orders of magnitude. Image credit: NASA.

The third telescope in the *Swift* system is the UV/Optical Telescope (UVOT) and is essentially the same instrument as the OM onboard *XMM-Newton*. It covers observations on the tail end of burst afterglows in the 170 - 600 nm range. The UVOT has a 17 arcmin^2 field of view and can begin observations of a source within $\sim$150 seconds after the spacecraft has slewed to the pointed position.

As both the XRT and UVOT are triggered by the BAT, *Swift* provides a nearly-simultaneous,

[4]http://heasarc.nasa.gov/docs/swift/about_swift/bat_desc.html

multiwavelength observations over almost five orders of magnitude in energy. Unlike *Chandra* and *XMM-Newton*, however, *Swift* is in a nearly-circular low-Earth orbit. While *Swift* was primarily built to detect and observe GRB as quickly as possible, its ability to scan the gamma-ray sky has proven invaluable to AGN research as well. The *Swift*-BAT 70 Month Hard X-ray Survey (a continuation of the 54-month catalogue) observed at a flux level of $1.34\times10^{-11}\,\mathrm{erg\,cm^{-2}\,s^{-1}}$ in over 90% of the sky making it the largest and deepest high-energy all-sky survey to date (Baumgartner et al. 2012, in process). Around 711 AGN are in the catalogue[5], 292 of which are Seyfert 1 galaxies.

2.2 *XMM-Newton* Data

The *XMM-Newton* observations of HE 0436 were serendipitous during the targeted observation of the pulsar PSR J0437.4-4711 about 4.2 arcmin away. The first observation (hereafter XMM1) was during revolution 0519 on the 9^{th} of October 2002 and spanned 70.5 ks. Two MOS detectors operated in full-frame mode with a thin filter. Due to the variable nature of the pulsar target, the pn camera was set to timing mode also with a thin filter in place. The Optical Monitor (OM) simultaneously collected data from HE 0436 during this observation although the object was outside the field of view of the reflection grating spectrometers (RGS1 and RGS2). The OM data were limited to observations in the UVW1 ($\lambda_{\max}$ = 2675 Å) and V ($\lambda_{\max}$ = 5235 Å) filters.

The second *XMM-Newton* observation (hereafter XMM2) was during revolution 1835 on the 15^{th} of December 2009 and spanned 130 ks – roughly double that of the first observation. The EPIC instruments operated in the same manner as in the first observation. Unfortunately, during XMM2 only the MOS instruments observed HE 0436 as the source fell outside of the pn narrower field of view used for timing mode.

The ESA has developed a Science Analysis System (SAS) to process *XMM-Newton* raw data. SAS is made up of a vast collection of libraries, tasks, and scripts designed to reduce, calibrate, and analyze observational files. Raw data obtained from *XMM-Newton* instruments manifest as

[5]http://swift.gsfc.nasa.gov/docs/swift/results/bs70mon/

both calibrated and uncalibrated data that can be manipulated in a number of ways. To ease the process, SAS has been designed to be fully compliant with the most common astronomical analyses packages such as FTOOLS, XANADU, and DS9 although it does not include any analysis tools itself. The system is compatible with Windows, Linux, and Unix machines and also includes an optional graphical user interface. SAS is updated and patched frequently, the most current version being SAS 13.0.1 released on May 8^{th} 2013 and patched on June 19^{th}.

Data files from both epochs were processed to produce calibrated event lists using the *XMM-Newton* Science Analysis System (SAS) version 12.0.0. The data were examined for background flaring and pileup; only minor flaring was seen in the very beginnings of XMM2 MOS data and those periods were ignored. No pileup was detected. For the MOS data, source photons were extracted from a circular region 35 arcsec in radius and centered on the object. The background photons were extracted from a larger circular area 50 arcsec in radius close to the object and then scaled appropriately.

Due to the timing mode, source photons from the pn data were extracted from a rectangular region 2° in width centered on the object and the background photons from a larger rectangular region and also scaled. Single-quadruple events were selected for the MOS data while single and double events were selected for the pn; events next to a bad pixel or the CCD edge were omitted (i.e. data quality flag set to zero). The entire process was then repeated for XMM2. Spectra from the MOS data were limited to the 0.5 - 10.0 keV range based on cross-calibration uncertainties, while the pn spectra were limited further in the soft band from 0.6 - 10.0 keV because of the less accurate calibration in timing mode[6]. Data from the pn instrument above 8 keV were ignored in the analysis as well due to the source becoming background dominated.

XMM-Newton slew data were also available via the first *XMM-Newton* slew survey (XMMSL1). During the slew capture of HE 0436, the pn instrument operated in full-frame mode with a medium filter. The total 0.2 - 10.0 keV count rate recorded for the object was $8.28 \pm 0.95\,\mathrm{count\,s^{-1}}$ with

[6]See *XMM-Newton* Calibration Technical Note 0018 (XMM-SOC-CAL-TN-0018) section 11.2.2 for details

$7.58\pm0.91\,\mathrm{count\,s^{-1}}$ of the total being the soft band (0.2 - 2.0 keV) rate. The WebPIMMS[7] HEASARC tool was used to estimate the corresponding fluxes assuming a basic power law spectral model. A power law was fit to the XMM1 pn spectrum from 0.6 - 2.0 keV to get an appropriate value for Γ. Galactic extinction, as defined by hydrogen column density N_{H}, was determined from the Leiden/Argentine/Bonn (LAB) Survey of Galactic HI (Kalberla et al. 2005). A value of N_{H} = $1.03\times10^{20}\,\mathrm{cm^{-2}}$ was adopted. Estimated slew fluxes were determined to be $(5.02\pm1.31)\times10^{-12}$ $\mathrm{erg\,cm^{-2}\,s^{-1}}$ from 0.5 - 2.0 keV and $(8.11\pm3.02)\times10^{-12}\,\mathrm{erg\,cm^{-2}\,s^{-1}}$ from 2 - 10 keV.

2.3 *Chandra* Data

The pulsar PSR J0437.4-4711 is used as a calibration source for the *Chandra* observatory. Of the eleven observations between 2000 - 2006, HE 0436 falls in the field of view during six: ObsIDs 742, 1850, 6155, 6156, 6157, and 7216. ObsIDs 742 and 1850 were observed with the HRC-I and -S detectors and thus only imaging data are available; these are ignored.

The *Chandra* team developed their own data processing system called the Chandra Interactive Analysis of Observations (CIAO). While CIAO can be used in conjunction with FTOOLS and other analysis systems, some *Chandra*-specific programs have been made including the plotting tool ChIPS and model fitting tool Sherpa. The most recent version of CIAO was released June 28^{th} 2013 as v. 4.5.3 [8].

The ACIS-S data were processed using the most recent version of CIAO at the time (v. 4.4.0) and preliminary spectra were extracted. After analyzing the spectra it was clear that the data were piled up. Several reprocessing methods were attempted, however the quality of the data were not high enough to justify any further analysis and the *Chandra* data are no longer used in this work.

[7] http://heasarc.gsfc.nasa.gov/Tools/w3pimms.html
[8] http://cxc.harvard.edu/ciao/index.html

2.4 *Swift* Data

HE 0436 has been observed by *Swift* three times with the first two observations in 2007 and the most recent (hereafter Sw3) being in June 2013. The first observation (hereafter Sw1) had the highest exposure time for all three instruments, followed by the second observation (hereafter Sw2).

Raw *Swift* data is run through the Swift Processing Pipeline before becoming available for use, after which certain *Swift*-specific HEASARC analysis tools are recommended (see HEASARC webpage for details). The BAT, XRT, and UVOT processed data for Sw1 and 2 was kindly provided by D. Grupe. The XRT spectra were found to be comparable and since Sw1 held the highest count rates of all three observations, it was used in all subsequent analyses. The Sw1 XRT observation was performed in photon counting mode with a 500×500 pixel window frame.

A summary of the data used in this work is shown in Table 2.1.

Table 2.1: HE 0436-4717 Data Analysis Log.

Telescope	**ObsID**	**Instrument**	**Filter**	**Start Date**	**Duration** (s)	**GTI** (s)
XMM-Newton	0112320201	pn	thin	09/10/2002	68177	67210
		MOS 1	thin		69167	68270
		MOS 2	thin		69167	68380
		OM	UVW1		34996*	N/A
			V		25000*	N/A
	9129900003	pn slew	none	01/12/2007	8	N/A
	0603460101	MOS 1	thin	12/15/2009	129141	126900
		MOS 2	thin		129146	123600
Swift	00035763001	XRT	none	12/07/2007	10090	9732
		UVOT	V		838	838
			B		840	840
			U		840	840
			UVW1		1681	1681
			UVM2		2286	2286
			UVW2		3369	3369
	54-mo survey	BAT	none	09/21/2010	N/A	N/A

*Individual filters exposed for a range of 1998 - 5001 s each with a sum of 10 exposures for UVW1 and 5 exposures for V.

Chapter 3

XMM-Newton Initial X-ray Spectral Analysis

3.1 Broadband First Look

All spectral model fitting was performed using the X-ray spectral fitting package XSPEC v. 12.8.0. Spectral models assume a cosmology of $H_{\rm o}$ = 70 $\rm km\,s^{-1}\ Mpc^{-1}$, $q_{\rm o}$ = 0, and $\Lambda_{\rm o}$ = 0.73 and all parameters are given in the rest frame of HE 0436 unless otherwise noted. A redshift of z = 0.053 was adopted. All models also include a Galactic column density of $N_{\rm H}$ = 1.03$\times10^{20}\,\rm cm^{-2}$. Errors on model parameters correspond to a 90% confidence level (i.e. $\Delta\chi^2$= 2.7 criterion). Significance is defined as $\Delta\chi^2\geq$ 3 for a change in one parameter.

Before attempting model fitting with all three EPIC spectra, the MOS spectra alone were analyzed to see if the data were consistent within their respective epochs. The cross-calibration between both MOS instruments is expected to be within 4%[1] between 0.3 - 10.0 keV. To test for consistency, the MOS 1 and MOS 2 spectra for XMM1 were fit independently using the basic toy models that were planned to be tested over all instruments – including a power law, broken power law, and power law plus black body. The best fits were found for each model and, if parameters

[1] See XMM-SOC-CAL-TN-0018 section 4.0 for details

normally agreed within measurement uncertainty, they were linked in future fitting. The procedure was then repeated for XMM2. In both cases, nearly all parameters agreed within uncertainty as expected.

Once the initial MOS calibration checks were complete, the pn data were included in XMM1 and the spectra from both epochs were fit with a basic power law over 2 - 10 keV in an effort to model only the primary X-ray emission. The pn spectrum alone was truncated because of high background reducing the signal quality above 8 keV. After fitting, the model was extrapolated down to the 0.6 keV lower limit to observe the broadband residuals. Residual features from this initial fit show an excess below 2 keV and ∼6.0 keV (see Fig. 3.1). A basic power law does not explain the spectral shape alone and further models are required. Comparable results were found for XMM2.

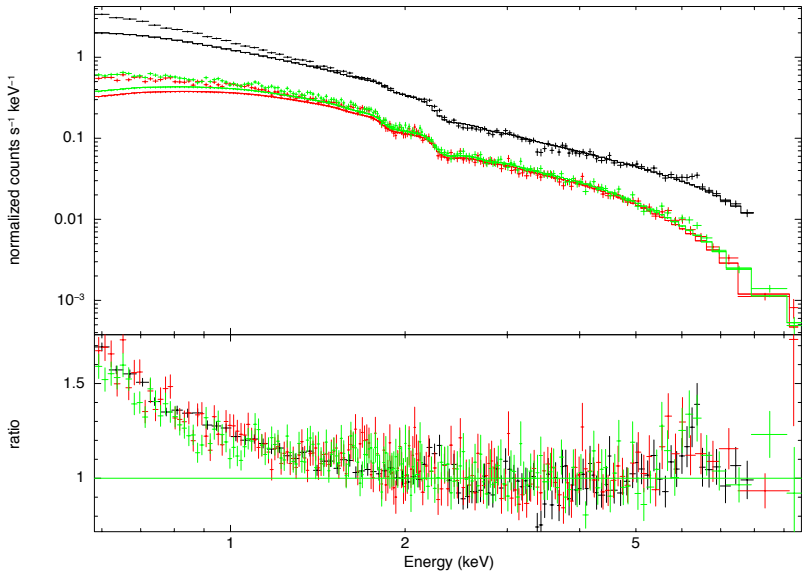

Figure 3.1: XMM1 EPIC X-ray spectra broadband initial look. Spectra are fit from 2-10 keV with a power law that is then extrapolated to the full 0.6-10.0 keV band. The pn data (black) are truncated at 8 keV due to high background. MOS 1 and MOS 2 data are red and green, respectively. Clear positive residual features are seen below 2 keV and around 6 keV, illustrating the soft excess and iron line features common in Seyfert 1 galaxies.

Wang et al. (1998) note some absorption features in addition to the soft excess and iron line

in their broadband analysis of HE 0436. One edge was seen in a 1992 *ROSAT* spectrum and was consistent with neutral carbon, with an energy around 0.28 keV and optical depth (τ) around 3.46, in the source frame. An *ASCA* 1994 spectrum showed a different absorption edge around $E \sim 0.83$ keV with $\tau \sim 0.27$. The authors note that the this feature is consistent with a possible combination of O VII and O VIII edges, however the $\sim$0.8 keV edge is not seen in earlier *ASCA* epochs.

The authors also test for the presence of any intrinsic X-ray column density by allowing the Galactic X-ray column density to vary during spectral fits. They found that Galactic column density alone (they adopted a value of $2\times10^{20}\,\mathrm{cm}^{-2}$) described the data well, indicating the absence of intrinsic X-ray column density.

To see if such a (potential) oxygen feature could be detected here, the EPIC spectra from XMM1 were fit simultaneously from 0.6 - 10.0 keV with a model composed of a power law, black body, and Gaussian line in an attempt to account for the residual features seen in Fig. 3.1. The pn data were truncated at 8 keV and the MOS data were linked after an initial fitting confirmed the model parameter values for each instrument were comparable. This foundation model described the data well, with χ^2 = 853 for 813 degrees of freedom (d.o.f.), and no residual features remaining (Fig. 3.2, a). The pn model parameters had a black body temperature of $kT = 0.10^{+0.02}_{-0.03}$ keV, a power law slope of $\Gamma = 2.13^{+0.10}_{-0.05}$, and an emission line energy of $E = 6.25^{+0.38}_{-1.01}$ keV. The linked MOS model had parameter values that agreed with those of the pn.

An absorption edge was added to the foundation model with values frozen at those discovered in the 1994 *ASCA* spectrum: E = 0.83 keV and τ = 0.27. The feature predicted by the *ASCA* observation is not seen in the scenario described by the current parameters, as it over-predicts the data between 0.8 - 0.9 keV (Fig. 3.2, b). When all parameters but those of the edge were allowed to vary, the fit statistic worsened considerably by a change in χ^2 ($\Delta\chi^2$) of 106 with no additional free parameters and residual features remained below $\sim$1 keV (Fig. 3.2, c). Lastly, if the edge parameters were allowed to vary as well, the fit improved by $\Delta\chi^2$ = 8 for two additional free parameters and the residuals were comparable to the initial fit without any absorption at all. The feature was insignificant, however, as $\tau = 0.08^{+0.04}_{-0.05}$ for an edge at $E = 0.75^{+0.04}_{-0.03}$ keV. Comparable

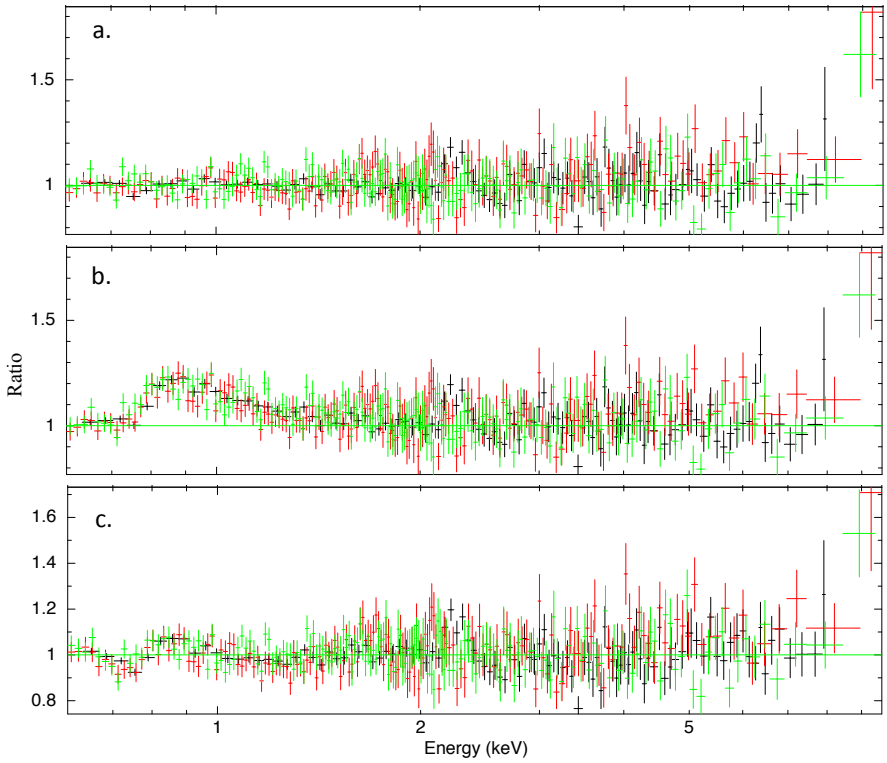

Figure 3.2: Initial absorption edge analysis for the broadband X-ray spectra of *XMM-Newton* . A foundation model consisting of a power law, black body, and Gaussian line described the data well as can be seen by the top residuals (a). If an absorption edge describing the feature seen in the 1994 *ASCA* spectrum (Wang et al. 1998) is inserted, the model under-predicts the data between 0.8 - 0.9 keV (b). Allowing model parameters to vary with the same edge does not improve the goodness-of-fit (c). If all parameters are allowed to vary, the residuals are consistent with (a) however the feature is insignificant with $\tau = 0.08^{+0.04}_{-0.05}$. Only XMM1 is shown for clarity and XMM2 had consistent results.

results were found for the XMM2 MOS spectra.

As Galactic column density alone described the data well in foundation model (Fig. 3.2, a), it is expected that no other X-ray column density is required. Intrinsic X-ray column density was also tested independently by adding a separate column density at the redshift of the source, in addition to that of the Milky Way already present in the foundation model described above. The best fit in this case had negligible intrinsic column density as $N_{\rm H} < 10^{20}\,{\rm cm}^{-2}$ with a fit statistic of χ^2 / d.o.f. = 8850 / 811.

An initial test for absorption edges in the broadband X-ray spectra of HE 0436 concludes that no absorption features are required to describe these data. In addition, no intrinsic X-ray column density is significantly detected.

3.2 The 3 - 10 keV Analysis

The 3 - 10 keV band alone was analyzed in an effort to examine the iron line spectral region, first using simple Gaussian lines and then using more complex models. Due to the minor, but noticeable calibration difference between the MOS and pn instruments, a constant factor was introduced. This constant factor was applied to the MOS models alone and the MOS models were then fully linked to the pn. The factor was 1.23$\pm$0.03 for all fits.

A simple power law gave a fit of χ^2 = 478 for 447 d.o.f. in XMM1 and 501 for 491 d.o.f. in XMM2. It was significantly improved by the addition of a single narrow (σ = 1 eV) Gaussian line frozen at E = 6.4 keV to correspond with neutral Fe Kα emission. The fit improvement for one additional free parameter was $\Delta\chi^2$ = 4 and $\Delta\chi^2$ = 10 for XMM1 and XMM2, respectively. Allowing the line to broaden improved the fits further for an additional free parameter, with $\Delta\chi^2$ = 7 for XMM1 and $\Delta\chi^2$ = 12 for XMM2. A narrow line with energy allowed to vary was not a significant improvement at either epoch. However, if both the energy and width of the line were variable, the goodness-of-fit was comparable to the broad Fe Kα line. This simple exercise confirmed that a broader line is favored over a narrow one and that the feature appears comparable at both epochs.

It is possible that multiple emission lines can be present instead of a single broad line; depending on the quality of the data it can be difficult to resolve multiple components, especially if there are several sources of emission from a range of distances. Fe Kβ features in particular have been seen in more than 30% of Seyfert 1 galaxies (Guainazzi et al. 2006) and the Fe XXV and Fe XXVI ions have been attributed to BLR clouds (Miller 2007). The Fe Kα - *K*β relationship in particular is interesting as the strength of the *K*β line is known to be 17% that of *K*α and thus can help constrain possible additional features in a spectrum where a Fe Kα line is present.

Two Gaussian lines representing Fe Kα and Fe Kβ – with normalizations scaled appropriately – did not significantly change the goodness-of-fit for either epoch in comparison to the single broad line (see Fig. 3.3). Tests for narrow Fe XXV and Fe XXVI worsened the fit, with one additional free parameter yielding $\Delta\chi^2$= 11 for XMM1 and $\Delta\chi^2$= 10 for XMM2, and returned insignificant equivalent widths (EW) for Fe XXVI. Other combinations of possible lines were tried, including all three iron features at once, but none returned significant values. The most reasonable fits are detailed in Table 3.1.

It is difficult to pinpoint the most acceptable iron line model from toy fits of the 3 - 10 keV region. XMM2 data can be explained equally well by all of the scenarios and that of XMM1 can be modeled by both a single broad line or multiple line components. The XMM1 iron feature in particular seems to favor at least one broad line, as none of the narrow line models improved the goodness-of-fit.

The full-width half-maximum (FWHM) of the iron line was calculated for both the pn and linked MOS spectra. The measured FWHM corresponded to velocities of $\sim$0.45 c and $\sim$0.31 c for pn and MOS, respectively. Grupe et al. (2010, hereafter G10) measured the FWHM of the optical Hβ line in HE 0436 and determined the BLR velocity to be around 3990 $\mathrm{km\,s^{-1}}$ or about 0.01 c. Thus, while the exact nature of the iron feature and the possibility of multiple lines remained uncertain, it is clear the line(s) are not originating from the BLR but instead display disk-like velocities ($\gtrsim$ 0.1 c, Miller 2007).

As a broad line appears to be favored in the XMM1 spectra, more realistic models were applied

Model	Component	Parameter	XMM1	XMM2
Power Law	continuum	Γ	1.76±0.05	1.97±0.05
		χ^2_ν/ d.o.f.	1.07 / 447	1.02 / 491
Power Law	narrow Fe Kα	Γ	1.78±0.05	1.99±0.05
+ Gaussian		χ^2_ν/ d.o.f.	1.06 / 446	1.00 / 490
	broad Fe Kα line	Γ	$1.85^{+0.07}_{-0.06}$	$2.05^{+0.07}_{-0.09}$
		σ (keV)	$0.38^{+0.21}_{-0.13}$	$0.47^{+0.36}_{-0.47}$
		χ^2_ν/ d.o.f.	1.02 / 445	1.00 / 489
	narrow line	Γ	1.79±0.05	1.99±0.05
	(free energy)	E (keV)	$6.62^{+0.08}_{-0.10}$	6.42±0.08
		χ^2_ν/ d.o.f.	1.04 / 445	1.01 / 489
	free line	Γ	$1.84^{+0.07}_{-0.06}$	$2.03^{+0.07}_{-0.06}$
		E (keV)	$6.52^{+0.12}_{-0.14}$	$6.55^{+0.17}_{-0.29}$
		σ (keV)	$0.31^{+0.40}_{-0.27}$	$0.30^{+0.21}_{-0.17}$
		χ^2_ν/ d.o.f.	1.01 / 444	1.00 / 488
Power Law +	Fe Kα & Fe Kβ	Γ	$1.86^{+0.07}_{-0.06}$	$2.01^{+0.06}_{-0.05}$
2 Gaussians		σ (keV)	$0.35^{+0.20}_{-0.12}$	$0.10^{+0.59}_{-0.10}$
		χ^2_ν/ d.o.f.	1.01 / 445	1.00 / 489
	narrow Fe XXV & Fe XXVI	Γ	$1.78^{+0.06}_{-0.05}$	1.99±0.05
		χ^2_ν/ d.o.f.	1.04 / 445	1.02 / 489

Table 3.1: Fe line basic spectral models for *XMM-Newton* data, applied to the 3-10 keV band. The pn data were truncated at 8 keV due to high background. XMM1 models were linked across all three EPIC instruments and a constant factor applied to the MOS to account for calibration discrepancies. The constant factor remained at 1.23±0.03 for all fits. XMM2 models were directly linked as only MOS data is available. Normalization of the Kβ line was set at 17% that of Kα. Other combinations of the Kα, Kβ, XXV, and XXVI iron lines were tested but were not significant. For simplicity, only variable parameters are shown. All narrow lines had σ frozen at 0.001 keV and specific features were set at their intrinsic energy locations.

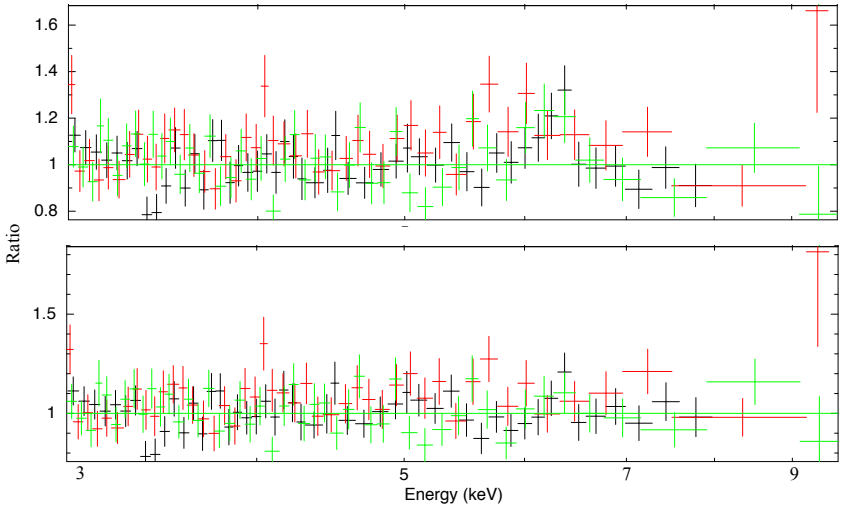

Figure 3.3: XMM1 toy model residuals from 3-10 keV with a power law (top) and power law plus broad Fe Kα line (bottom). The pn data are truncated at 8 keV due to high background. An iron feature is seen in the power law only model. A broad line takes care of the $\sim$6 keV excess completely. Comparable results were found for XMM2

to the 3 - 10 keV region in order to compare the results of distant and blurred reflection. Curvature from absorption can also create the appearance of a broadened line, as was discussed previously, and such a scenario will be tested later (see Section 5.2).

In the first step up from a basic Gaussian, a *laor* (Laor 1991) and *diskline* model (Fabian et al. 1989) were both used to describe a single emission line from a relativistic accretion disk. The two models have similar defining parameters including inner ($R_{\rm in}$) and outer ($R_{\rm out}$) disk radius, inclination (θ), and emissivity (q). Emissivity scales as R^{-q} where q is chosen between q = 3 or 2 in *diskline* for radii far from or close to the primary emitter, respectively. The parameter is allowed to vary freely in *laor*. The *diskline* calculations, however, consider only a non-rotating (i.e. Schwartzschild) black holes and thus restrict the inner radius parameter to a minimum radius of 6 $R_{\rm g}$. Laor expanded on the calculations in *diskline* to include spinning (i.e. Kerr) black holes

and thus the inner radius parameter in *laor* can reach the minimum value of $1.235\,R_{\rm g}$. By using the *laor* model, one can investigate the scenario of maximum black hole spin which appears to be increasingly relevant as recent studies have suggested that most supermassive black holes have high spin values (Walton et al. 2013).

XMM1 spectra were fit well by either a single relativistic line or a distant plus blurred reflection combination. The *laor* and *diskline* models were statistically indistinguishable, although it is worth noting that the best fit for *diskline* required its minimum inner radius of $6\,R_{\rm g}$ (see Table 3.2).

Distant reflection was also modeled two ways: with *pexmon* (Nandra et al. 2007) and with *reflionx* (Ross et al. 1999, Ross & Fabian 2005). Nandra et al. (2007) combined a model of smooth (i.e. featureless) neutral power law reflection (*pexrav*, Magdziarz & Zdziarski 1995) with the self-consistently generated spectral features Fe Kα, Fe Kβ, Ni Kα, and the Compton Hump. The *pexmon* model does not include ionization effects nor any features in the soft band.

The *reflionx* model is also a power law reflection model, but incorporates the effects of ionization by including fully ionized features and many forbidden lines throughout a 1 eV - 1 MeV range. In practice, the two models should be nearly identical when the ionization effects of *reflionx* are minimized. The ionization parameter, ξ, is calculated over the range of 3×10^{1} - $1\times10^{4}\,\mathrm{erg\,cm\,s^{-1}}$ and is defined as $\xi = \frac{4\pi F}{n}$, where F is the total illuminating flux and n is the number density of hydrogen. By setting $\xi = 1\,\mathrm{erg\,cm\,s^{-1}}$ in *reflionx*, one minimizes ionization and essentially mimics neutral reflection instead. The model *reflionx* includes a much wider range of spectral features, however, and so perhaps can be considered more realistic.

To model distance reflection, iron abundances were set to solar values and power law slope to the canonical value of $\Gamma = 1.9$ in both *pexmon* and *reflionx*. The ionization parameter was also frozen at $1\,\mathrm{erg\,cm\,s^{-1}}$ in *reflionx*. As expected, the values defined by the *pexmon* model were comparable to those found using *reflionx* with minimal ionization (see Fig. 3.4).

The initial iron line investigation favors the presence of a broad line; the cause of the broadening is addressed later. This preliminary exercise proved that the *reflionx* and *pexmon* models are comparable and therefore justifies the use of the *reflionx* model exclusively in the future.

Model	Component	Parameter	XMM1	XMM2
laor	single	Γ	1.85±0.06	2.08±0.07
	relativistic line	E (keV)	6.21±0.08	$6.38^{+0.21}_{-0.14}$
		χ^2_ν/ d.o.f.	1.01 / 444	0.99 / 488
diskline	single	Γ	$1.84^{+0.06}_{-0.09}$	$2.03^{+0.06}_{-0.05}$
	relativistic line	E (keV)	$6.24^{+0.07}_{-0.08}$	$6.27^{+0.18}_{-0.21}$
		χ^2_ν/ d.o.f.	1.01 / 444	1.00 / 488
pexmon	reflection	$\Gamma_{\rm power\ law}$	1.82±0.06	$2.06^{+0.08}_{-0.06}$
	spectrum	Γ_{pexmon}	1.90	...
		Fe (solar)	1.00	...
		χ^2_ν/ d.o.f.	1.05 / 445	1.00 / 489
reflionx	reflection	$\Gamma_{\rm power\ law}$	1.83±0.06	2.05±0.06
	spectrum	$\Gamma_{reflionx}$	1.90	...
		Fe (solar)	1.00	...
		ξ (erg cm s^{-1})	1.00	...
		χ^2_ν/ d.o.f.	1.05 / 446	1.00 / 490

Table 3.2: Fe line reflection models for *XMM-Newton* spectra, applied to the 3-10 keV band. The pn data are truncated at 8 keV due to high background. XMM1 models were linked across all three EPIC instruments and a constant factor applied to the MOS to account for calibration discrepancies; the constant factor remained at 1.23±0.03 for all fits. XMM2 models were directly linked as only MOS data is available for that epoch. The *laor* model was fit with maximum spin and both *laor* and *diskline* had an inclination angle set to 30°. A *reflionx* model used for distant reflection should be equivalent to *pexmon* however *pexmon* does not consider atomic features in the soft band. Ellipses represent constant values across the epochs.

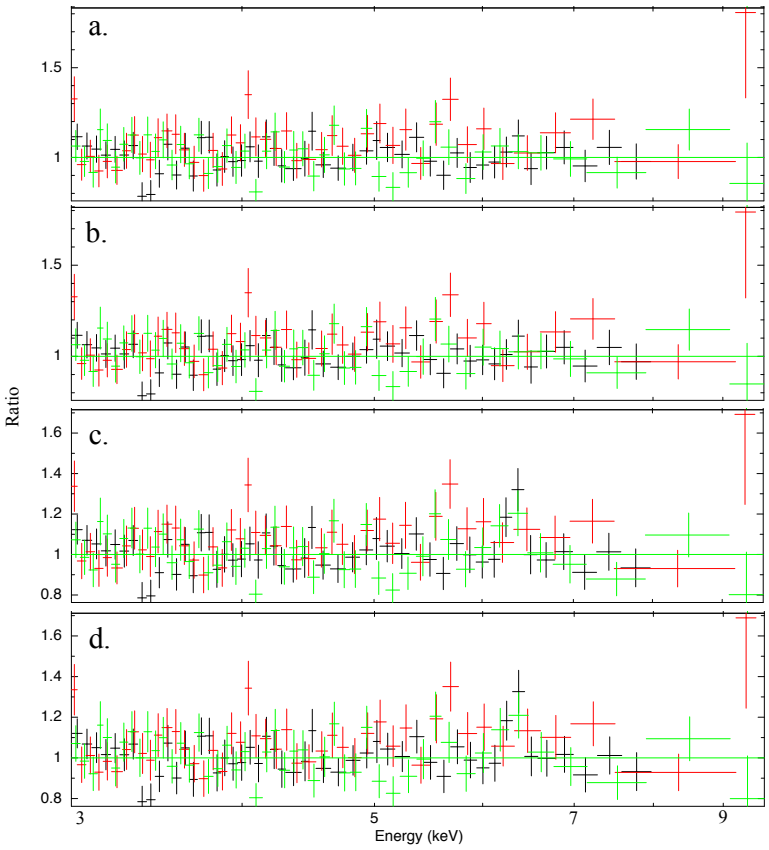

Figure 3.4: XMM1 physical model residuals from 3-10 keV with a power law plus laor line (a), diskline (b), pexmon (c), and reflionx (d) models. A relativistic line accounts for the iron residual feature fully while a distant reflector leaves slight positive residual feature around 6 keV. A distant emission feature may still be present, however some kind of broad line is required. The *reflionx* and *pexmon* models are consistent and so *reflionx* was used in all subsequent reflection models. Comparable results were found for XMM2.

Chapter 4

UV/X-ray Spectral Energy Distribution

X-ray emission provides valuable insight into the accretion process in the inner regions closest to the black hole. However, the bolometric emission is dominated by UV radiation from the disk. Disk accretion directly affects black hole growth, long-term variability, and may also influence features such as jets, winds, and disk atmospheres. To better understand AGN accretion mechanisms, the optical/UV and X-ray bands (as well as IR for heavily absorbed, Type II objects) must be investigated as a whole in an attempt to capture as much of the total accretion emission as possible.

4.1 Initial Exploration Using $\alpha_{\rm ox}$

One method for probing the disk-corona relationship is to measure the slope of a hypothetical power law connecting the X-ray and UV spectral bands ($\alpha_{\rm ox}$). Specifically, $\alpha_{\rm ox}$ = 0.3838 log($\frac{F_{\rm X}}{F_{\rm UV}}$) where $F_{\rm X}$ is the flux density measured at 2 keV and $F_{\rm UV}$ is the flux density measured at 2500 Å, in the rest frame (Avni & Tananbaum 1982). Values seem to range from approximately -1.15 to -1.40 for Type I AGN (Grupe et al. 2010, hereafter G10).

Measurements of $\alpha_{\rm ox}$ in a variety of objects have shown that AGN bolometric luminosity is indicative of the relative strength of emission in the X-ray vs. UV bands: more luminous AGN emit

less X-ray radiation per unit UV than AGN that are less luminous (Vagnetti et al. 2010). The physical mechanisms behind this relationship are still being investigated. Vagnetti et al. (2010) demonstrated that variations in $\alpha_{\rm ox}$ ($\Delta\alpha_{\rm ox}$) increases on longer timescales, implying that $\alpha_{\rm ox}$ variability is due at least in part to the disk-driven variability.

Using the *XMM-Newton* MOS data and the OM data from the UVW1 filter, $\alpha_{\rm ox}$ was estimated for both epochs and found to be $\alpha_{\rm ox,XMM1}$ = -1.27 and $\alpha_{\rm ox,XMM2}$ = -1.26. The two MOS spectra were linked during spectral fitting for this measurement. The values show no significant deviation between XMM1 and XMM2. The higher X-ray flux in XMM2 predicts that the $\alpha_{\rm ox}$ slope be shallower for that epoch – as is the case. These $\alpha_{\rm ox}$ slopes found for HE 0436 are reasonable (Vagnetti et al. 2012) and all fall within the span of values calculated by G10 for 92 Type I AGN. The $\alpha_{\rm ox}$ values indicate that HE 0436 is behaving "normally" (Gallo 2006) and extreme absorption or extreme relativistic effects are not likely to be present.

4.2 Detailed SED Modeling Using *Swift*

Calculations such as $\alpha_{\rm ox}$ are useful in determining how AGN X-ray flux relates to that of the UV. The $\alpha_{\rm ox}$ slope is a limited tool, however, as it can only give an approximated broadband profile. Ideally, one would like to analyze a broadband spectral energy distribution (SED) that can be used in model fitting directly (e.g. Elvis et al. 1994). The SED, along with a robust value for black hole mass, can then be used to estimate the accretion rate of an AGN defined by the Eddington ratio: $L_{\rm Bol}$ / $L_{\rm Edd}$. $L_{\rm Bol}$ is the bolometric luminosity and $L_{\rm Edd}$ = 1.38×10^{38} $\rm M_{BH}/M_{\odot}$ is the Eddington luminosity, which is the maximum luminosity a black hole of mass $\rm M_{BH}$ can have and remain in equilibrium.

Swift data (Sw1) were used for the broadband analysis of HE 0436 to remain as consistent as possible with instrumental calibrations. The *XMM-Newton* X-ray data have better signal-to-noise than the *Swift* XRT, but the OM observed in only two filters whereas the UVOT instrument on *Swift* captured HE 0436 in all six of its filters. In addition, *Swift* BAT data are also available for coverage

up to 100 keV.

Following the procedures outlined in Vasudevan & Fabian (2009) and then expanded upon by Vasudevan et al. (2009) (hereafter V09), the basic model to be applied to the SED was a broken power law plus a simple black body accretion disk. The broken power law representing the primary X-ray emission was convolved with the Galactic column density while the disk component included Galactic extinction as well. Parameters defined in the black body accretion disk model included $R_{\rm in}$, the disk normalization (K), and the maximum temperature of the accretion disk ($T_{\rm max}$). $T_{\rm max}$ was allowed to vary and the inner radius was set to $6\,{\rm R_g}$, the ISCO of a Schwarzschild black hole. K is defined as $\frac{M_{BH}^2\,cos\,i}{D_{\rm L}^2\,\beta^4}$ where i is the inclination of the disk, $D_{\rm L}$ the luminosity distance to the source in kpc, and β the color/temperature effective ratio. The black hole mass for HE 0436 was adopted from G10 as $\rm M_{BH} = 5.9{\times}10^7\,M_\odot$ and a luminosity distance of 233.1 Mpc was found using Ned Wright's Cosmological Calculator[1] for z = 0.053 with the cosmology: $H_{\rm o} = 71\,{\rm km\,s^{-1}\ Mpc^{-1}}$, $\Omega_{\rm M}$ = 0.27, and $\Omega_{\rm vac}$ = 0.73. V09 demonstrated that cos i and β could be set to 1 for Type I AGN, and thus the value for K was calculated and fixed. Assuming a Comptonization origin for the X-rays, the break in the power law corresponded to $T_{\rm max}$ of the disk component. Galactic absorption was set to $N_{\rm H}$ = $1.03{\times}10^{20}\,{\rm cm^{-2}}$ and intrinsic extinction was considered in various ways.

It should be noted that one conclusion from the UVOT processing investigation (Section 2.4) was that the optical/UV spectrum appeared quite flat. G10 suggested that a flat spectrum may indicate that light from the host galaxy was significant. While complete separation of AGN emission from the host galaxy is beyond the scope of this work, for practical purposes the influence of such host light is normally negligible and does not effect AGN spectral fits. In this case, however, the optical filters (V, B, and U) were omitted from the fitting because of concern over possible contamination. The flat slope of the UVOT data was determined to not be a result of processing techniques (D. Grupe, private correspondence) and was, in fact, the true shape of the UVOT spectra. The XRT data were also fit over a reduced range of 2 - 10 keV. This limit was placed to ensure the primary X-ray emission was fit rather than the soft excess, which likely has a different origin.

[1] http://www.astro.ucla.edu/ wright/CosmoCalc.html

The first model tested (see A; Fig. 4.1, top) described the simplest case where only Galactic extinction modified the intrinsic broadband spectrum. This scenario did not describe the data well, returning a χ^2 = 102 / 30 d.o.f. The luminosity over the SED range of 0.001 - 100 keV, $L_{0.001-100\,\mathrm{keV}}$, is a good approximation for L_{Bol} as the majority of AGN emission is in the UV and this is not a heavily-absorbed object. With $L_{0.001-100\,\mathrm{keV}} = 6.39\times10^{44}\,\mathrm{erg\,s^{-1}}$, the Eddington ratio for this model is 0.08. Neither the Eddington ratio nor L_{Bol} are unusual values, however the poor fit indicates Galactic extinction alone can not explain these data.

Intrinsic extinction was then added to the UV spectrum and allowed to vary (see B; Fig. 4.1, bottom). The fit improved by $\Delta\chi^2$= 71 for an additional free parameter. The extinction that described the SED best was $E_{\mathrm{B-V}} = 0.095\pm0.011$. Luminosity decreased significantly, where $L_{0.001-100\,\mathrm{keV}} = 1.52\times10^{45}\,\mathrm{erg\,s^{-1}}$ giving a value of 0.02 for the Eddington ratio. This scenario statistically describes the broadband spectra very well, however it is inconsistent with the X-ray analysis performed in Section 3.1. With the measured UV extinction, the corresponding column density can be calculated using the relationship outlined by Predehl & Schmidt (1995): $N_{\mathrm{H}} = 5.3\times10^{21}\,\mathrm{cm^{-2}}\,E_{\mathrm{B-V}}$. For $E_{\mathrm{B-V}}$ ranging from 0.084 - 0.105, $N_{\mathrm{H}} = (5.04\pm0.58)\times10^{20}\,\mathrm{cm^{-2}}$ – magnitudes simply not seen in the X-ray spectra. In addition, G10 measures extinction from the Balmer decrement and finds $E_{\mathrm{B-V}}$ = 0.04 which is outside the range required for the goodness-of-fit in this case. Therefore, while this model is statistically favorable it is at odds with several independent measurements and other scenarios should be considered.

Next, the extinction value measured from the Balmer decrement was used (see C; Fig. 4.2, top) and K was allowed to vary. With no change in d.o.f., the fit improved marginally in comparison to Model B by $\Delta\chi^2$= 1. The best value for K was $(52.16\pm14.30)\times10^{-4}\,\mathrm{M_\odot{}^2\,kpc^{-2}}$ and $L_{0.001-100\,\mathrm{keV}} = 4.99\times10^{45}\,\mathrm{erg\,s^{-1}}$. With the larger luminosity, L_{Bol} / L_{Edd}= 0.07. This variation provides a better goodness-of-fit overall and has some physical justification with the use of the Balmer decrement.

There remains the final possibility that any variation between the UV and X-ray bands could be attributed to the disk flux alone. Therefore, a final model was tested that included only

Table 4.1: SED model fitting for *Swift* Epoch 1 UVOT and XRT broadband analysis.

	Model Variations			
	A	**B**	**C**	**D**
χ^2_ν/ d.o.f.	3.50 / 30	1.06 / 29	1.03 / 29	1.02 / 29
$L_{0.001-100\,\mathrm{keV}}$ ($\times 10^{44}\,\mathrm{erg\,s^{-1}}$)	6.39	1.52	6.47	4.99
$E_{B-V,int}$	0	0.095±0.011	0.04	0
$E_{B-V,Gal}$	0.009	...	...	...
T_{max} ($\times 10^{-4}$ keV)	52.63±0.02	68.48±2.08	31.14±2.47	23.45±1.43
K ($\times 10^4\,\mathrm{M_\odot}^2\,\mathrm{kpc^{-2}}$)	6.41	6.41	52.87±14.30	107.54±25.77
power law norm. ($\times 10^{-2}$) ($\mathrm{ph\,keV^{-1}\,cm^{-2}\,s^{-1}}$)	1.36±0.06	0.63±0.06	6.22±1.42	14.16±2.59
L_{Bol} / L_{Edd}	0.08	0.02	0.09	0.07

Galactic extinction and allowed *K* to vary (see D; Fig. 4.2, bottom). The fit statistic was the same as that for Model C and *K* = (107.54±25.77)$\times 10^5$ $\mathrm{M_\odot}^2\,\mathrm{kpc}^{-2}$. In this case, $L_{0.001-100\,\mathrm{keV}}$ = $4.99\times10^{44}\,\mathrm{erg\,s^{-1}}$ and so L_{Bol} / L_{Edd}= 0.07. This fourth scenario also describes the data well and has no apparent inconsistencies.

A summary of the model variations with their respective parameters and Eddington ratios are listed in Table 4.1. The SED models with high extinction values do fit the data, but they seem at odds with the X-ray analysis (Sec. 3.1), extinction measured from the Balmer decrement (G10), and the UV spectral analysis (Halpern & Marshall 1996). The SED can also be explained, however, if we assume the source is not reddened but that the ($\mathrm{M_{BH}}$ / D_{L})^2 is uncertain.

Swift BAT data were placed on the SED plots to see the high energy trend, but the data were not included in any of the spectral fits. Although the uncertainty in the BAT data allow for a wide spread, the highest energy spectrum does fall along the projected models for the most sensitive points. Model D (i.e. no intrinsic extinction and *K* allowed to vary) was plotted along with the BAT data to show both the observer and source frame (see Fig. 4.3).

The Eddington ratios determined from the *Swift* SED analysis agree with the value of 0.08 found by G10 for this object. An Eddington ratio around 0.08 is not unusual, although it does fall on the lower end of the probability distribution described by V09 in their analysis of 26 low-z AGN (see V09 Fig. 15, lefthand panel). A lower Eddington ratio implies HE 0436 is not a rapid accreter.

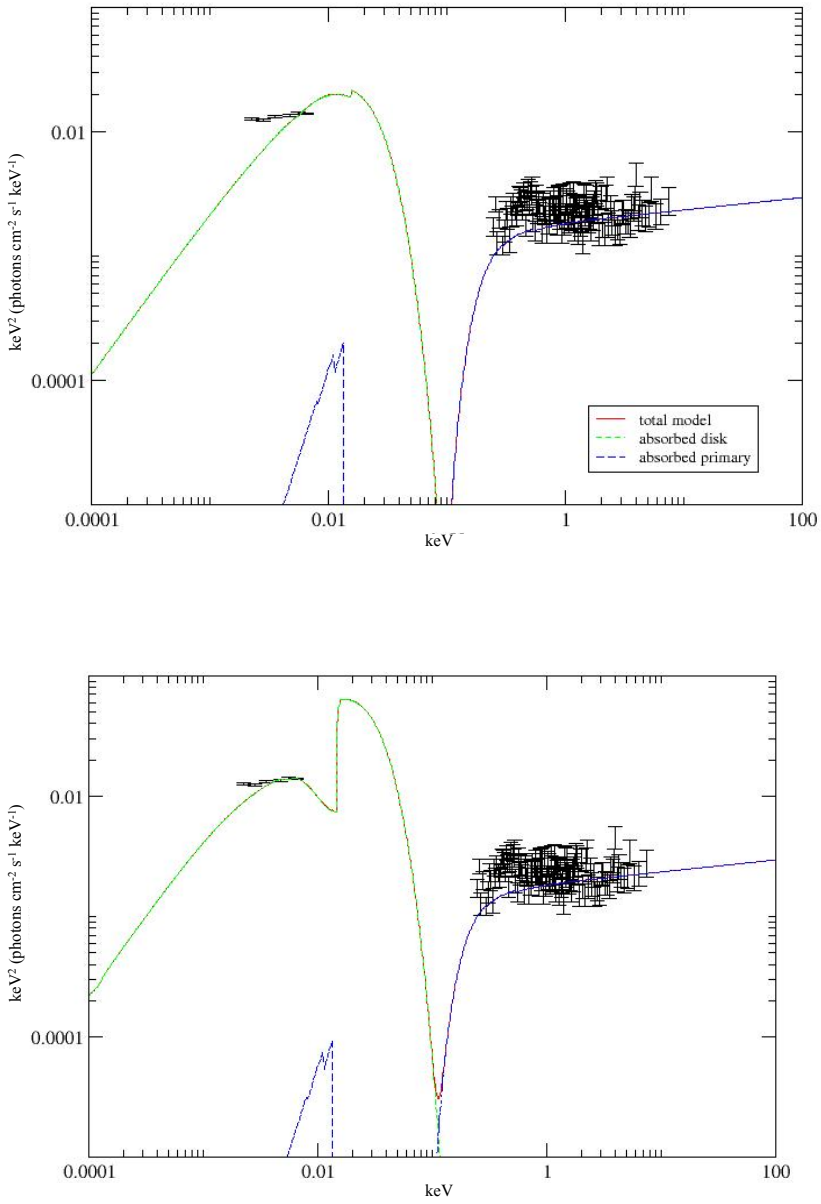

Figure 4.1: *Swift* UV/X-ray Spectral Energy Distribution model fits. UVOT and XRT data are fit with a composition of a broken power law plus disk reflection. The optical UVOT filters are not included in the fits for fear of host galaxy contamination. Likewise, the XRT data are fit only in the 2-10 keV range to prevent influence from the soft excess. Model A (top) includes only Galactic extinction while Model B (bottom) includes both Galactic and intrinsic UV extinction. The solid red line illustrating the total model follows the curves of the disk emission (green dotted line) and primary X-ray component (blue dotted line).

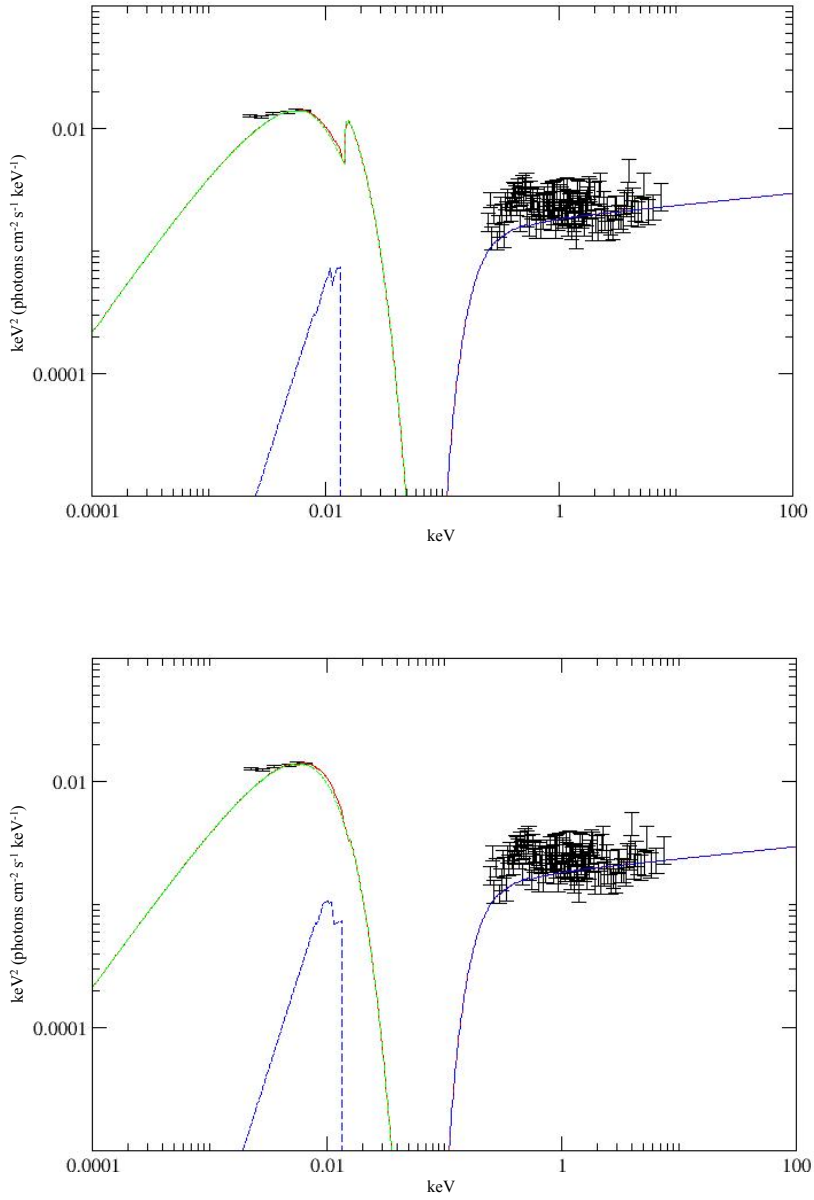

Figure 4.2: *Swift* UV/X-ray Spectral Energy Distribution model fits. UVOT and XRT data are fit with a composition of a broken power law plus disk reflection. The optical UVOT filters are not included in the fits for fear of host galaxy contamination. Likewise, the XRT data are fit only in the 2-10 keV range to prevent influence from the soft excess. Both models allow K to vary. Model C (top) also has UV extinction set to the value measured from the Balmer decrement and Model D (bottom) includes only Galactic extinction. The solid red line illustrating the total model follows the curves of the disk emission (green dotted line) and primary X-ray component (blue dotted line).

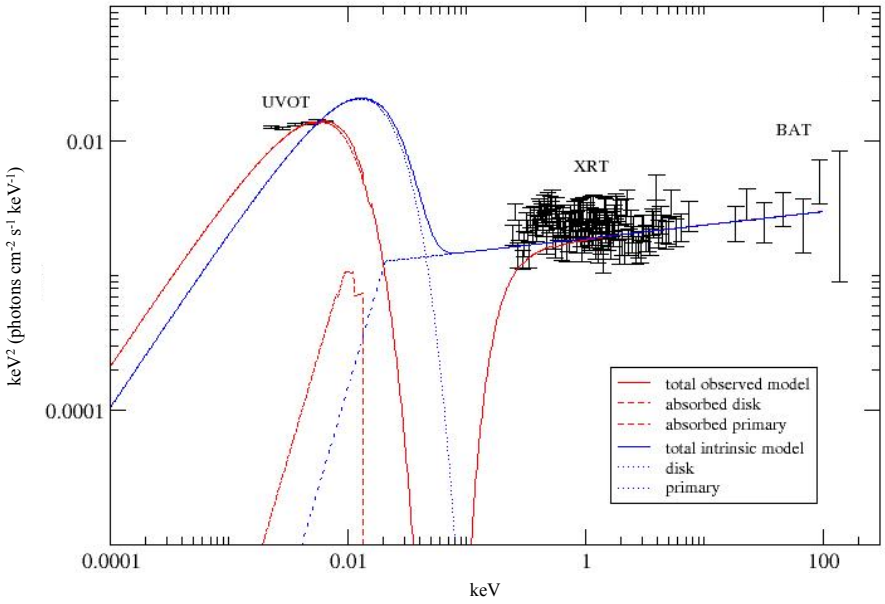

Figure 4.3: An SED comparison of Model D with no intrinsic extinction and K allowed to vary. The blue lines represent the intrinsic model in the source frame. Red lines represent the observed model. Only the XRT data from 2.0-10.0 keV and the UV data of the UVOT were fit to the model, the rest of the models were extrapolated and the BAT data overlaid.

Chapter 5

Broadband X-ray Spectral Analysis

The first glance at the broadband X-ray spectra of HE 0436 in Chapter 3 showed the presence of multiple components. A modest but clear soft excess can be seen by extrapolating a 2 - 10 keV power law to lower energies. In addition, an iron line feature of some kind is present. Attempts to resolve the iron line region alone using simple models did not distinguish between many of the possible line scenarios. Statistically, a single broad feature was preferred over a single narrow feature, but the nature of the line remains unclear. In Section 1.2, we discussed how the soft excess and iron complex could arise from relativistically blurred ionized reflection in the disk.

Several points need to be addressed. First, it should be determined whether or not there are models that can explain the broadband spectra in a consistent manner. By expanding the spectral analysis to include softer X-rays, the nature of the iron line may be revealed. In Section 3.2 it was shown that the iron line most likely is not originating from the BLR based on high velocity estimates, however that does not rule out the possibility of emission originating close to the black hole.

The possibility of absorption must also be considered. Instead of emission from the inner regions of the accretion disk resulting in an iron line being broadened and smeared by relativity, the broad feature could instead be an artifact of the curvature induced by absorption in the line of sight (Sec. 1.2.3).

Finally, a third scenario for the soft excess will be tested. Section 1.2.4 discussed the possibility

of a second Compton region that scatters disk emission into the soft X-rays producing the low energy hump. This scenario is independent of the reflection and absorption theories for a broadened iron line, as either could be applied to the continuum in order to explain an emission feature. Instead, a second Compton region simply adds another source to the spectrum that produces the soft excess.

5.1 Merging MOS Data

In Sec. 3.2 it was confirmed that the *XMM-Newton* MOS data agree well between the two instruments. Therefore, the MOS spectra at each epoch were merged using the FTOOLS program *addascaspec* in an effort to increase signal to noise in the data and simplify model fitting. This program was originally written by Ken Ebisawa for use with ASCA data although it also works with data from other instruments. A homemade script utilizing much of the same HEASARC tools as *addascaspec* was tested as well. Both scripts yielded comparable results and the following analysis was done using the *addascaspec*-produced merged MOS spectra.

To confirm the consistency of the merged spectrum with the spectra from individual instruments, the merged spectra were initially fit from 0.5 - 10.0 keV using basic toy models: a simple power law; power law plus black body; broken power law; and a power law with a black body and a Gaussian line. In general, the photon index of the XMM2 continuum is higher than that of XMM1 and the line feature around 6.4 keV that is significant in XMM1 is weaker in the later epoch. The results are consistent with the previous analysis of the individual MOS instruments.

Having found the toy models in agreement with the past analysis, multiple reflection and absorption models were explored next as well as the new model from Done et al. (2012) describing soft Comptonization originating from the inner regions of the accretion disk. In addition, there will be a concerted effort to fit the multi-epoch data in a self-consistent manner. Consequently, the single pn spectrum from XMM1 is ignored and only the MOS data that exists at all epochs are compared.

5.2 Partial Covering Absorption

Curvature in the spectrum can be induced by absorbers instead of relativistic effects. Turner & Miller (2009) explain in detail how gas with a range of column densities can influence the primary component of an AGN. As absorbers move in the field of view, some of the intrinsic radiation is both scattered and absorbed (Fig. 5.1). Both changes in the covering fraction and column density can create spectral variability over a range of timescales. A strong soft excess can appear at lower energies and even the Fe Kα line can be broadened by absorption with the red shoulder being enhanced by attenuation rather than by relativistic effects. In this section, a thorough attempt to fit the X-ray spectrum of HE 0436 with absorption is documented in an effort to determine the origin of the X-ray emission in this object.

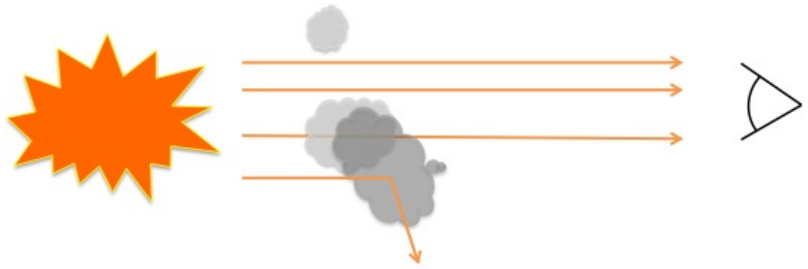

Figure 5.1: A simple illustration of a partial covering scenario. Ionized or neutral absorbers lie along the line of sight and attenuate the intrinsic radiation produced by the central engine. Both the covering fraction and column density vary over a range of timescales as the absorbers move across the field of view.

5.2.1 Neutral Absorbers

The model *zpcfabs* was used to begin testing for possible neutral absorption signatures. A single, neutral absorber was applied to a simple power law and fit to both epochs of the merged MOS data. In this initial test, both power law parameters were linked across the epochs in an attempt to attribute any spectral variability to the neutral absorber; only the covering fraction remained free to vary between XMM1 and XMM2. The fit was poor at χ^2 / d.o.f. = 2898 / 2033 and clear residual features remained in the soft band and above 5 keV. Linking the absorption parameters and allowing

the primary component to vary at each epoch instead improved the fit ($\Delta\chi^2$ = 44 for 1 additional free parameter), although the goodness-of-fit remained poor. If instead all parameters are allowed to vary, the fit improves by $\Delta\chi^2$ = 56 for 3 additional free parameters with consistent residuals. It is interesting to note that this scenario did require the column density of the absorber to roughly double from XMM1 to XMM2 while neither the covering fraction nor primary emitter varied.

A second neutral absorber was added to the model and the parameters reset so that only the covering fraction varied between epochs. The double neutral absorption described the data better with χ^2 / d.o.f. = 2253 / 2030 and the residual features improved, though the model continued to underestimate the data at higher energies (see Fig. 5.2). This scenario called for the two absorbers to have very different densities (see Table 5.1) and could potentially describe a single absorber with a density gradient along the line of sight, rather than two completely independent bodies. The column densities remain consistent in the two epochs and so would not (alone) explain any spectral variability seen over longer timescales.

If the primary emitter was then also allowed to vary, the goodness-of-fit did not improve significantly. Allowing only the primary emitter to vary instead of the covering fractions of the absorbers also did not improve the fit quality significantly. If there is any variability in the primary emitter from epoch-to-epoch, it is subtle.

5.2.2 Ionized Partial Covering

The data were fit with a single, ionized absorber applied to a simple power law. The ionized absorber was modeled by *zxipcf*. Once again, all parameters except for covering fraction were linked at the epochs in an effort to describe the long-term variability with changes in an absorber. The residuals showed a disparity between XMM1 and XMM2 $\sim$0.6 keV and the fit quality was poor (χ^2 / d.o.f. = 2415 / 2032). The covering fraction was not significantly different from one epoch to the next.

If the photon index of the primary component is allowed to vary while the absorber is frozen and linked across the epochs, the fit improves by $\Delta\chi^2$ = 213 for two additional free parameters and

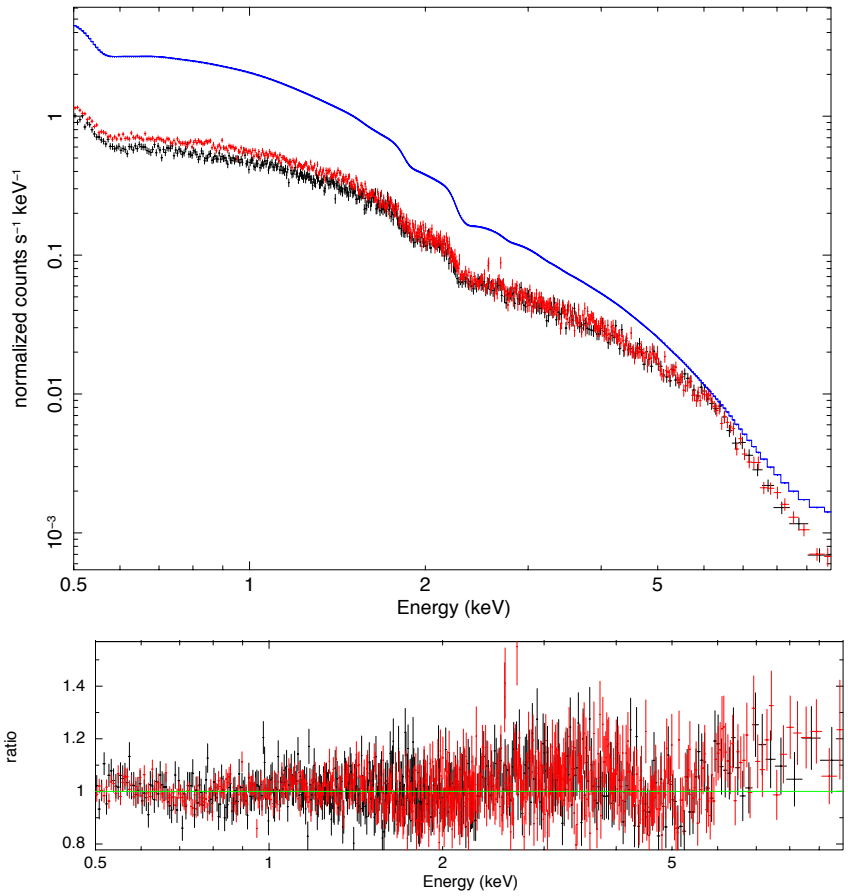

Figure 5.2: Neutral partial covering model and its relation to the merged MOS spectra. A pair of neutral absorbers were fit to the merged MOS X-ray spectra from 0.5-10.0 keV with the covering fraction as the only parameter varying at both epochs. The XMM1 (black) and XMM2 (red) data are shown with the constant intrinsic power law determined by the model (blue) in the top panel. The model residuals are shown below.

Model	Model Component	Model Parameter	XMM1	XMM2
single absorber	neutral absorption	N_H (cm^{-2})	$8.80^{+1.18}_{-1.13}$x10^{22}	...
		CF	0.49±0.01	0.37±0.02
	power law	Γ	2.38±0.01	...
	fit quality	χ^2_ν/d.o.f.	1.43/2033	
single absorber w/ PL free	neutral absorption	N_H (cm^{-2})	$4.93^{+1.84}_{-1.02}$x10^{22}	$11.25^{+2.27}_{-1.91}$x10^{22}
		CF	0.42±0.02	0.43±0.02
	power law	Γ	$2.37^{+0.04}_{-0.03}$	2.34±0.01
	fit quality	χ^2_ν/d.o.f.	1.40/2030	
double absorber	neutral absorption 1	N_H (cm^{-2})	$26.30^{+3.27}_{-2.94}$x10^{22}	...
		CF	0.61±0.02	0.56±0.02
	neutral absorption 2	N_H (cm^{-2})	$1.33^{+0.10}_{-0.09}$x10^{22}	...
		CF	0.48±0.02	0.42±0.02
	power law	Γ	2.66±0.03	...
	fit quality	χ^2_ν/d.o.f.	1.11/2030	
double absorber w/ PL free	neutral absorption 1	N_H (cm^{-2})	$25.78^{+3.27}_{-2.80}$x10^{22}	...
		CF	0.60±0.03	0.56±0.02
	neutral absorption 2	N_H (cm^{-2})	$1.32^{+0.10}_{-0.09}$x10^{22}	...
		CF	0.50±0.03	0.41±0.03
	power law	Γ	2.68±0.05	$2.65^{+0.04}_{-0.03}$
	fit quality	χ^2_ν/d.o.f.	1.11/2028	

Table 5.1: Merged MOS spectra fit with neutral, partial covering models in the 0.5-10.0 keV band. Two absorbers with very different densities provide the best goodness-of-fit for the neutral absorption scenario. Differences in the spectra at the two epochs can be described by changes in the covering fraction of the absorbers.

the epoch disparity $\sim$0.6 keV disappears. However, some positive residual features remain. The photon index in XMM2 rises, going from Γ = 2.16$\pm$0.01 to Γ = 2.24$\pm$0.01, consistent with the trend found in the toy model fits. It appears that the model with a single ionized absorber detects a slight, long-term variability from the primary emitter while the model with a single neutral absorber does not.

A second ionized absorber was added to the model and the parameters reset so that only the covering fractions were unlinked across the epochs. The fit was significantly better than that of the single absorber ($\Delta\chi^2$/ d.o.f. = 2150 / 2028) and no residual features remained (see Fig. 5.3), although the covering fractions for both absorbing bodies continued to be statistically unchanging across the epochs. Thus, as a final exercise, one absorber was kept constant throughout the epochs while the other was allowed to vary in $N_{\rm H}$ and ξ, with Γ free to vary as well. The goodness-of-fit remained unchanged and the parameters that were allowed to be independent in XMM2 did not significantly change from their XMM1 values (see Table 5.2).

None of the ionized absorption model variations defined the source of long-term variability with any significance. However, the scenario in which only the covering fraction varied between epochs did result in the best goodness-of-fit. The most satisfying absorption model overall describes two ionized absorbers, the first more ionized and with a higher column density than the second, with both having comparable covering fractions. Both absorbers are found to have redshifts comparable to the source that remained steady across the epochs.

In both the neutral and ionized absorption tests, the covering fraction was assumed to be the primary source of variability due to absorbers and not column density or ionization. This is an oversimplification because all three of the parameters are codependent to some extent and a change in one is likely to suggest a change in another. For example, by assuming covering fraction alone may vary over time, one is essentially adopting a homogenous slab model for an absorber rather than multiple discrete bodies that are more likely to be found in AGN central engines. However, all three absorption parameters were individually tested throughout the spectral fitting process and none of the parameters indicated that a more complex absorber was required. Thus, due to the quality of the

data and nature of the source, the simplified model of absorption is justified in this case. In addition, other tests are performed to further analyze the absorption models presented here (see Section 7.1).

5.3 Relativistic Blurring

The iron line analysis of Section 3.2 illustrates the possibility of accretion disk reflection as the source of the broad iron feature in the X-ray spectra of HE 0436. If reflection were indeed the source of the iron line, the reflection component would also be seen at lower energies as the soft excess (Section 1.2.4). The following describes an attempt to explain the full, broadband X-ray spectra of HE 0436 using the disk reflection scenario.

5.3.1 Initial Analysis: *kdblur2*

As an initial exercise, the broadband merged MOS spectra were fit from 0.5 - 10.0 keV with the ionized reflection model *reflionx* (Section 3.2) convolved by the relativistic smoothing effects of the *kdblur2* kernel. This kernel has been modified from the *laor* model by R.M. Johnstone and A.C. Fabian and uses the general relativity calculations outlined by Laor (1991). The parameters that describe *kdblur2* are: the inner disk radius ($R_{\rm in}$), outer disk radius ($R_{\rm out}$), disk inclination (θ), inner emissivity index ($\alpha_{\rm in}$), break radius ($R_{\rm br}$), and outer emissivity index ($\alpha_{\rm out}$). The latter three parameters define the emissivity profile and describe how the fraction of the reflected flux changes with radii. The profile changes from $\alpha_{\rm in}$ to $\alpha_{\rm out}$ at $R_{\rm br}$.

The emissivity profile follows the form $r^{-\alpha}$ where at large radii $\alpha \sim 3$, assuming the simplest case of a single point source and flat, Euclidean geometry. Relativistic effects and curved spacetime affect reflected emission closer to the black hole, changing the emissivity profile to have a steeper index at smaller radii. Thus a simple approximation for the emissivity profile can be a broken power law, though the true profile is likely more complex. (see Wilkins & Fabian 2011 for a review).

To begin the reflection model fitting, the parameters of *kdblur2* were left at their default values which include defining the emissivity profile as a single (unbroken) power law with $\alpha_{\rm in}$ = $\alpha_{\rm out}$ =

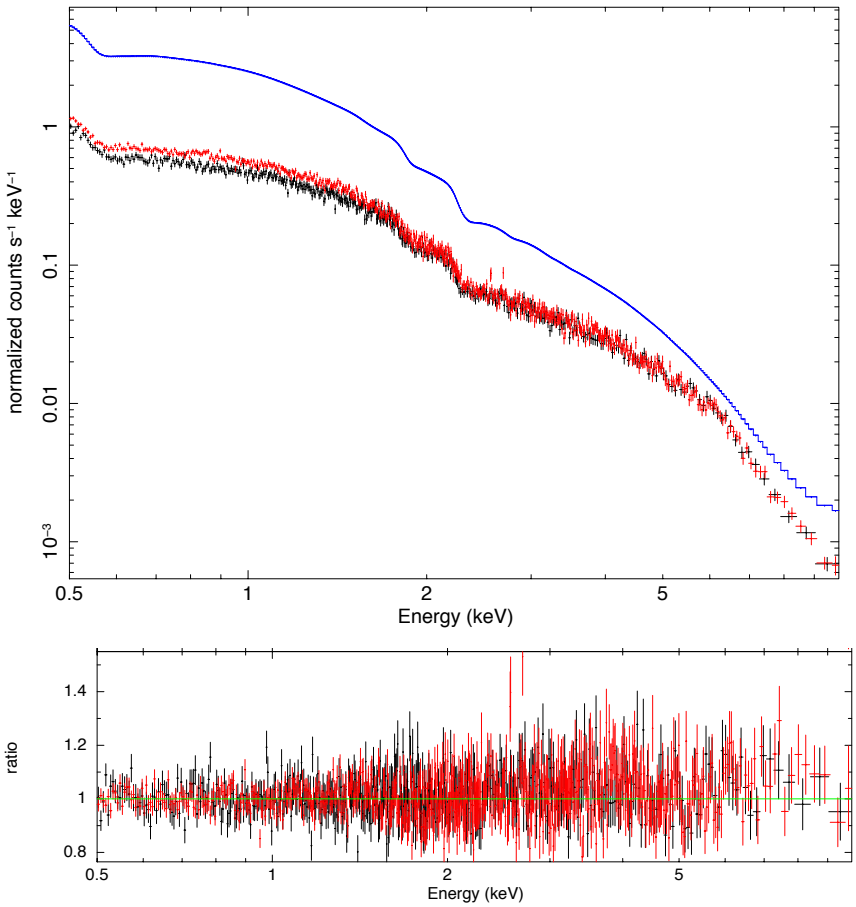

Figure 5.3: Ionized partial covering model and its relation to the merged MOS spectra. A pair of ionized absorbers were fit to the merged MOS X-ray spectra from 0.5-10.0 keV with the covering fraction as the only parameter varying at both epochs. The XMM1 (black) and XMM2 (red) data are shown with the constant intrinsic power law determined by the model (blue) in the top panel. The model residuals are shown below.

Model	Model Component	Model Parameter	XMM1	XMM2
single absorber	ionized absorption	N_H (cm^{-2})	$138.57^{+11.83}_{-16.52}$x10^{22}	...
		log(ξ) (log erg cm s^{-1})	$2.27^{+0.15}_{-0.08}$	...
		CF	$0.78^{+0.03}_{-0.04}$	$0.73^{+0.03}_{-0.05}$
	power law	Γ	2.22±0.01	...
	fit quality	χ^2_ν/d.o.f.	1.19/2032	
single absorber	ionized absorption	N_H (cm^{-2})	$135.79^{+12.99}_{-24.70}$x10^{22}	...
w/ PL free		log(ξ) (log erg cm s^{-1})	$2.33^{+0.24}_{-0.12}$	...
		CF	$0.71^{+0.04}_{-0.06}$	...
	power law	Γ	2.16±0.01	2.24±0.01
	fit quality	χ^2_ν/d.o.f.	1.11/2031	
double absorber	ionized absorption 1	N_H (cm^{-2})	$44.62^{+5.46}_{-6.27}$x10^{22}	...
w/ one linked		log(ξ) (log erg cm s^{-1})	$1.59^{+0.34}_{-0.30}$	...
		CF	$0.67^{+0.02}_{-0.03}$	0.63±0.03
	ionized absorption 2	N_H (cm^{-2})	$1.75^{+0.14}_{-0.13}$x10^{22}	...
		log(ξ) (log erg cm s^{-1})	$0.48^{+0.13}_{-0.10}$	...
		CF	0.52±0.03	0.44±0.04
	power law	Γ	2.63±0.05	...
	fit quality	χ^2_ν/d.o.f.	1.06/2028	
double absorber	ionized absorption 1	N_H (cm^{-2})	$44.34^{+5.44}_{-6.65}$x10^{22}	...
w/ PL free		log(ξ) (log erg cm s^{-1})	$1.60^{+0.34}_{-0.31}$	...
		CF	0.64±0.03	...
	ionized absorption 2	N_H (cm^{-2})	$1.82^{+0.23}_{-0.18}$x10^{22}	$1.71^{+0.15}_{-0.14}$x10^{22}
		log(ξ) (log erg cm s^{-1})	$0.61^{+0.25}_{-0.16}$	$0.44^{+0.15}_{-0.11}$
		CF	0.47±0.04	...
	power law	Γ	2.56±0.05	2.66±0.05
	fit quality	χ^2_ν/d.o.f.	1.07/2026	

Table 5.2: Merged MOS spectra fit with ionized absorption models in the 0.5-10.0 keV band. Two ionized absorbers with very different densities provide a good description of the data overall and the best scenario had all but the covering fractions of the absorbers constant from XMM1 to XMM2. The covering fractions also continued to remain consistent across the epochs for these fits and suggests long-term variability must originate from another source.

3. The inner radius was frozen at $6\,\mathrm{R_g}$ and iron abundance set to solar values. All parameters were linked across the epochs except for those defining the continuum power law components, which were left independent and free to vary.

The initial fit returned a χ^2 / d.o.f. = 3167 / 2032 and had clear positive residual features both below 1 keV and around 6 keV. Allowing the ionization parameter, ξ, to vary across the epochs did not influence the fit. Allowing $\alpha_{\rm in}$ to vary while remaining linked, however, improved the fit by $\Delta\chi^2$ = 766 for an additional free parameter, but required an extreme value of around 10. The emissivity profile parameters were then allowed to vary individually in an effort to refine the fit with more reasonable values for $\alpha_{\rm in}$. The best fit values remained consistently around $\alpha_{\rm in} \sim 7$, $R_{\rm br} \sim 5\,\mathrm{R_g}$, and $\alpha_{\rm out} \sim 4$ with the fit improving by $\Delta\chi^2$ = 120 for no additional free parameters. Thus, the data require at least one break in the emissivity profile, as expected.

Allowing θ to vary did not influence the fit significantly, although $R_{\rm in}$ favored a smaller radius at $\sim 4\,\mathrm{R_g}$ for the same goodness-of-fit. This suggests the black hole may be spinning as the disk around a spinning black hole has $R_{\rm in} \leq 6\,\mathrm{R_g}$. The iron abundance, too, favored a smaller value of $\sim$0.7 solar when allowed to vary, but it also did not change the fit statistic in this case.

As there remained a clear narrow iron line residual using a single reflector, a distant reflector was added to the model by including an additional *reflionx* with parameters set for neutral, unblurred reflection: iron abundance at solar, Γ = 1.9, ξ = $1\,\mathrm{erg\,cm\,s^{-1}}$, and the normalization free to vary. The distant reflector remained linked across the epochs. The initial fit did not change the fit statistic from that with blurred reflection alone, but allowing both iron abundance and $R_{\rm in}$ to vary improved the fit by $\Delta\chi^2$ = 198 for two additional free parameters and reduced the residual features. This clarifies the results from Section 3.2 which could not differentiate between a single and double iron line feature. A distant reflector is necessary to fit the X-ray spectrum in the reflection scenario (see Fig. 5.4).

No other parameters improved the fit significantly, although both $R_{\rm in}$ and iron abundance continued to drop if allowed to do so. The final model had a fit statistic of $\Delta\chi^2$ / d.o.f. = 2154 / 2033 (see Table 5.3).

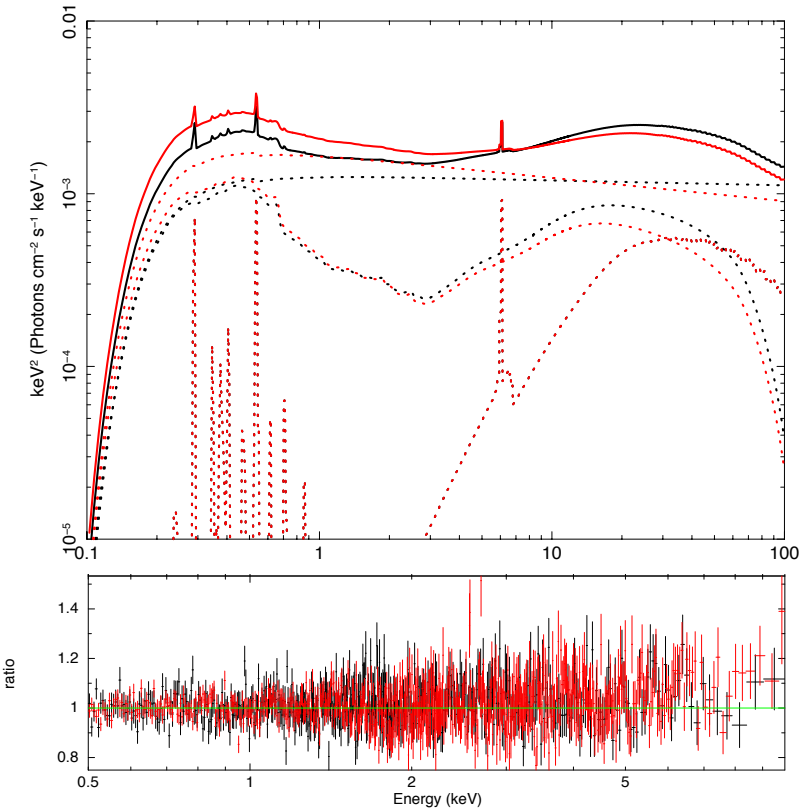

Figure 5.4: The best blurred reflection model utilizing the *kdblur2* convolution kernel with *reflionx*. The model was fit from 0.5 - 10.0 keV to the merged MOS spectra and all parameters except for those of the power law were linked across the epochs. XMM1 is black, XMM2 is red. A neutral, distant reflection component was necessary to fit the iron line. The total model (solid lines) is composed of a distant, neutral reflector (dotted lines with intrinsic atomic features), a blurred reflector (dotted lines with smoothed reflected profile), and the primary component (dotted power law lines).

Model Component	Model Parameter	XMM1	XMM2
primary source	Γ	2.03 ± 0.01	2.13 ± 0.01
	norm $(\mathrm{ph\,keV^{-1}\,cm^{-2}\,s^{-1}})$	$1.27^{+0.03}_{-0.06}\times10^{-3}$	$1.68^{+0.04}_{-0.06}\times10^{-3}$
blurred reflector	$\alpha_{\rm in}$	7.0	...
	$\alpha_{\rm out}$	3.0	...
	$R_{\rm br}$ ($\mathrm{R_g}$)	5.0	...
	$R_{\rm in}$ ($\mathrm{R_g}$)	2.0	...
	θ (°)	40.0	...
	Fe (solar)	$0.27^{+0.06}_{-0.05}$	...
	Γ	$\Gamma_{\rm primary}$	...
	ξ ($\mathrm{erg\,cm\,s^{-1}}$)	$200.76^{+8.00}_{-13.45}$	...
distant reflector	*Fe* (solar)	1.0	...
	Γ	1.9	...
	ξ ($\mathrm{erg\,cm\,s^{-1}}$)	1.0	...
	χ^2_ν/d.o.f.	1.06 / 2032	

Table 5.3: The best reflection model for *XMM-Newton* X-ray spectra using *kdblur2*. The model is composed of a power law, neutral reflection, and ionized reflection. Relativistic modification was performed by the *relconv* kernel. In this scenario, long-term variability is caused by fluctuations in the primary emitter.

The reflection interpretation seems to describe the X-ray spectra of HE 0436 well, however the iron abundance is very low (*Fe* ~ 0.3 solar, Fig. 5.5). Whether the low iron abundance is an intrinsic property of the source or an artifact of the model fitting is unclear at this time. The inner disk radius is also quite small, $R_{\rm in} \sim 2\,{\rm R_g}$, suggesting the black hole has a significant spin. A spinning black hole has a smaller ISCO, which in turn would amplify relativistic effects present in atomic features (Fig. 1.10). If the spin of HE 0436 were underestimated in the current reflection model, the iron abundance would be forced to drop as the model attempts to fit the broad iron line. Repeating the above procedure with reflection models that include a spin parameter (a) could help constrain the iron abundance (Fig. 5.5) and determine if this object does, in fact, have a high spin.

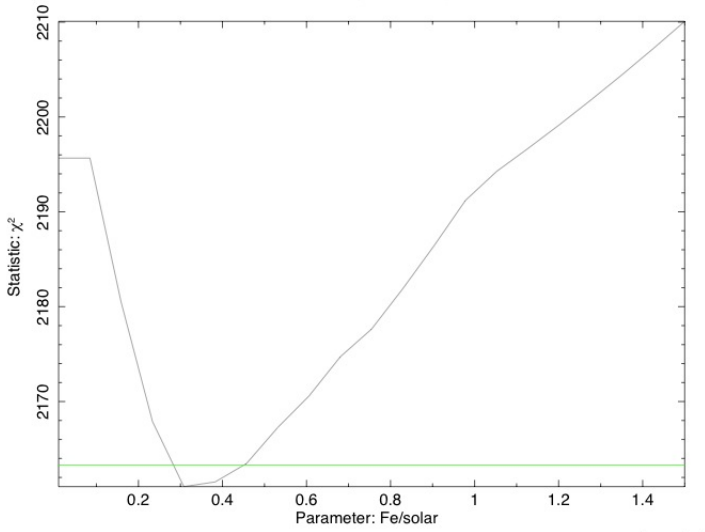

Figure 5.5: A confidence contour of iron abundance from the best reflection model utilizing *kdblur2* (black). The green line marks the fit statistic for the model, in this case χ^2 / d.o.f. = 2162 / 2032.

5.3.2 Examining the Low Iron Abundance

black hole spin dependency

Brenneman & Reynolds (2006) originally developed a model for accretion disk emission called *kerrdisk* which they later expanded upon and created a relativistic blurring modification that could

be applied to any emission. The new convolution kernel is called *kerrconv* and allows the user to define $\alpha_{\rm in},\ \alpha_{\rm out},\ R_{\rm br},\ a,\ \theta,\ R_{\rm in}$, and $R_{\rm out}$.

While *kerrconv* is widely used today, another model developed by Thomas Dauser (Dauser et al. 2010) has recently become available and takes the calculations a step further. Dauser's *relconv* performs essentially the same emission spectrum modification yet includes the possibility of retrograde spin. An antiparallel alignment of the black hole's angular momentum and its accretion disk requires a rather special set of circumstances and is not expected to be a common phenomenon. That being said, observations of Galactic binary systems have shown that the formation of a stellar mass black hole can at times result in a strong misalignment (i.e. "chaotic accretion", Brandt & Podsiadlowski 1995) and galactic mergers could potentially coalesce two supermassive black holes with vastly different spins, modifying the angular momentum of the central black hole from its original value (Moderski & Sikora 1996 and Volonteri et al. 2005). Whatever the cause may be, chaotic accretion is unstable and will settle over time into one of two configurations: a parallel or retrograde black hole spin. King et al. (2005) demonstrated that both extremes are stable and so retrograde spins are not theoretically excluded.

A simple exercise was performed to see if a retrograde orbit may be required for the *XMM-Newton* spectra and perhaps help explain the low iron abundance. The best *kdblur2* model was used with the iron abundance reset to solar and $R_{\rm in}$ to $9\,{\rm R_g}$: the ISCO for a retrograde-spinning black hole. Methodically, the other parameters were allowed to vary and the model refit until the best "retrograde" model was found.

The fit statistic for the retrograde spin model was χ^2 / d.o.f. = 2276 / 2031 compared to the 2161 / 2030 of the prograde analogue (see Fig. 5.6). While such a fit does not indicate the need for a retrograde spin, it does suggest that other mechanisms may be at work behind the seemly low iron abundance for HE 0436 and that more complex models are justified.

Both *kerrconv* and *relconv* were applied to ionized disk reflection (via *reflionx*) in a broadband model that included a power law in order to compare the two convolution kernels using the X-ray data of HE 0436. The two models - one using *kerrconv* to modify the source-frame emission, the

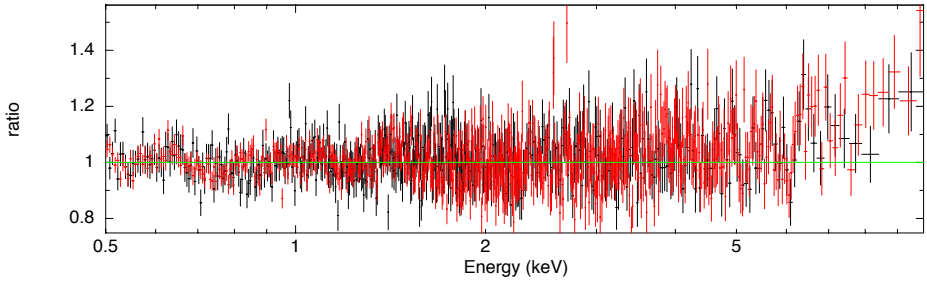

Figure 5.6: Model residuals from the retrograde spin exercise using the previously-defined best *kdblur2* model, fit to the merged MOS data. Iron abundance was reset to solar and $R_{\rm in}$ to $9\,{\rm R_g}$. The fit statistic was not as good as the prograde model, however it was surprisingly reasonable. Further analysis with models that include the spin parameter specifically may help clarify the seemingly low iron abundance in this object.

other using *relconv* - were evaluated side-by-side with the same parameters free to vary, the only restriction being to test prograde spins only. In each iteration of the fit not only did the parameters agree within their relative uncertainties, but the χ^2 statistics were consistent as well (i.e. $\Delta\chi^2 \leq 1$ for the same d.o.f.). With the two models proving their interchangability, preference was given to *relconv* in the following reflection models.

Having decided on utilizing the relativistic blurring kernel *relconv* to test the reflection scenario for the *XMM-Newton* spectra, a foundation model consisting of a power law, a distant neutral reflector, and blurred reflection from an ionized accretion disk was applied to the merged MOS data from 0.5 - 10.0 keV. Blurring parameters were initially set to the best-fit values found from the *kdblur2* analysis, while a was set to 0 and iron abundance reset to 1. Parameters were varied one at a time, with the exception of iron abundance and spin, to check their consistency with the *kdblur2* values and influence on the new *relconv* model. None alone significantly altered the goodness-of-fit, which remained around χ^2 / d.o.f. = 2264 / 2031.

When iron abundance was allowed to vary alone, it settled at a super-solar value around 1.5 solar although the fit statistic did not improve significantly ($\Delta\chi^2$ = 3 for one additional free parameter). The spin was then set to a high value of, $a = 0.8$, and iron abundance reset to 1. When iron abundance was then allowed to vary as the spin remained high, the fit improved (χ^2 / d.o.f. = 2166 / 2030) while returning an abundance of around 0.4 solar. Reflector normalizations were frozen after finding the

best fit values with no change in statistics. An effort was made to find an improved fit with an iron abundance closer to solar value – e.g. altering the emissivity profile, reducing the ionization parameter – but any significant improvement in iron abundance came with unreasonable conditions. A retrograde spin was also tested, with no success. The resulting model parameters are outlined in Table 5.4.

multiple blurred reflectors

With the iron abundance consistently low, the abundance was examined using a second blurred reflector. It is probably an oversimplification to model accretion disk reflection with a single reflector because the accretion disk itself is an extended source, emitting continuously from a range of radii. The observed reflected spectrum will actually be a composite of emission from points all along the accretion disk with radii closer to the black hole responsible for broad line features that are strongly distorted, and radii far from the black hole creating narrower features that are relatively unaffected.

The quality of most spectral data is such that the reflection component in most AGN spectra can simply be modeled by a single source. Adding a second blurred reflector did not significantly change the goodness-of-fit in this case as compared to the scenario with a single source. Iron abundance remained around 0.4 solar and freezing the abundance at solar metallicity did not improve the fit, but instead caused ξ to drop.

There are other over-simplifications in the reflection scenario that may influence iron abundance. For example, the *reflionx* model assumes the accretion disk has a constant density which is probably not the case in the actual physical systems. Illumination from the primary X-ray source is also not likely to be isotropic due to the effects of light bending close to the black hole and, therefore, a single ξ is too simple a model. These assumptions are acceptable, however, for the scope of the present work.

The best reflection model for HE 0436 requires high spin, low iron abundance, and with only the power law allowed to vary across the epochs; this describes a power law-dominated spectral state (see Fig. 5.7) which is in in agreement with the initial *kdblur2* fits (see Fig. 5.3.1). Despite the

Model Component	Model Parameter	XMM1	XMM2
primary source	Γ	2.04±0.01	2.14±0.01
	norm $(\mathrm{ph\,keV^{-1}\,cm^{-2}\,s^{-1}})$	$1.40\pm2.03\times10^{-3}$	...
blurred reflector	α_{in}	7.0	...
	α_{out}	4.0	...
	$R_{\mathrm{br}}\,(\mathrm{R_g})$	5.0	...
	a	0.8	...
	$\theta\,(^\circ)$	42.38	...
	Fe (solar)	0.40±0.09	...
	Γ	$\Gamma_{\mathrm{primary}}$	...
	$\xi\,(\mathrm{erg\,cm\,s^{-1}})$	$62.37^{+18.51}_{-7.96}$	...
distant reflector	*Fe* (solar)	1.0	...
	Γ	1.9	...
	$\xi\,(\mathrm{erg\,cm\,s^{-1}})$	1.0	...
	χ^2_ν/d.o.f.	1.07 / 2032	

Table 5.4: The best reflection model for *XMM-Newton* X-ray spectra. The model is composed of a power law, neutral reflection, and ionized reflection. Relativistic modification was performed by the *relconv* kernel. In this scenario, long-term variability is caused by fluctuations in the primary emitter.

use of the more involved reflection model, *relconv*, the iron abundance remained unusually low. A confidence contour of the iron abundance and spin illustrates the values favored in this scenario (see Fig. 5.8), where curves are shown for $\Delta\chi^2$ of 9.21, 4.61, and 2.3.

Since the iron abundance does not improve with extensive modeling, the consistent value of $\sim$0.3 solar may be the intrinsic metallicity and not an artifact of the fitting. The extreme parameters described by the model are unusual, however, especially considering the lower Eddington ratio found in Section 4.2 and lack of extreme spectral variability – both of which indicate HE 0436 is a rather average AGN. In general, the blurred reflection model fits the average, multi-epoch spectra well. The AGN is power law dominated at both epochs with a weak reflection component to account for the soft excess.

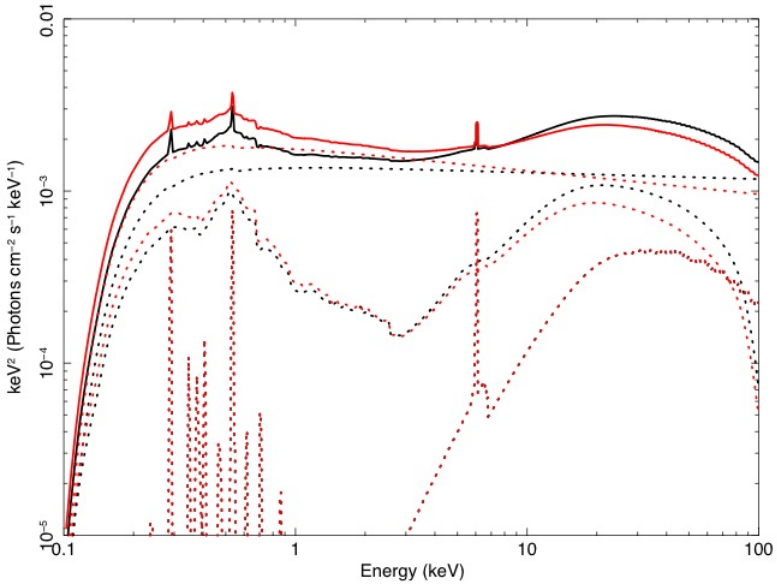

Figure 5.7: The best reflection model which is composed of a primary power law; a blurred, ionized reflector; and a distant, neutral reflector. This scenario requires high black hole spin, low iron abundance, and describes a power law-dominated state. Spectra were fit from 0.5-10.0 keV and the model extrapolated to higher energies. The model components are shown in dotted lines, the total model in solid lines. XMM1 is black, XMM2 is red.

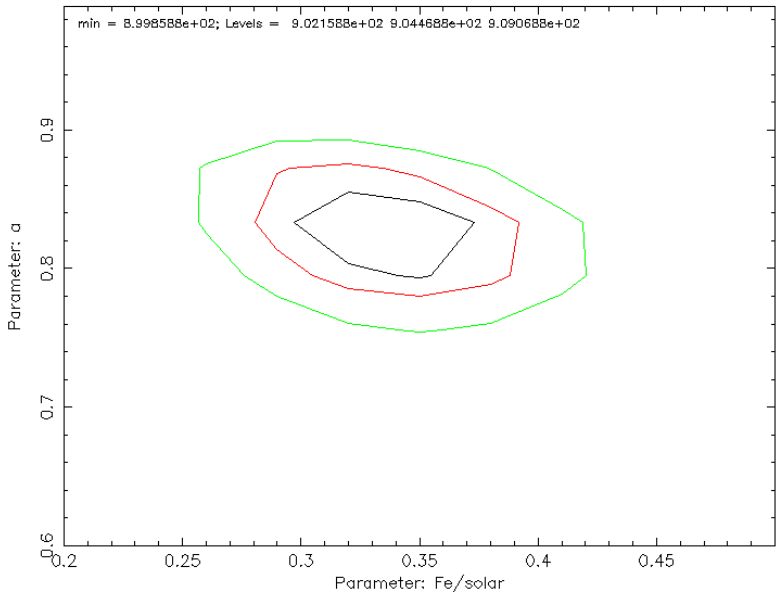

Figure 5.8: A two-dimensional confidence contour plot of iron abundance, *Fe / solar*, and spin parameter, *a* for best reflection model utilizing *relconv*. Curves are shown for $\Delta\chi^2$ of 9.21, 4.61, and 2.3.

5.4 Soft Comptonization

5.4.1 Mechanisms

Both the absorption and reflection scenarios addressed in the previous sections fit the soft excess in the spectra of HE 0436 well and it is statistically impossible to distinguish between the two without further analysis. Section 1.2.4 explained how disk reflection alone cannot produce the fluxes seen in most AGN soft excesses and thus absorption could be the most reasonable explanation. The reflection interpretation may continue to be valid if light bending is accounted for as in the best reflection model described in the previous section. Turner & Miller (2009) argued that multiple layers of ionized absorbers could reproduce the soft excesses seen in Mrk 766 and MCG 6-30-15 and so could account for most soft excess features in Seyfert galaxies. A third approach considers the possibility that the soft excess could be emerging from a second Comptonizing region. There are several physical possibilities for such a region, including hot clumps of material between the corona and the disk.

Observations of binary black holes have required two Comptonizing regions (Kubota & Done 2004) and simulations of a transient hotspot above the innermost region of a disk were able to confirm such a feature in Seyfert galaxy NGC 3516 (Iwasawa, Miniutti, and Fabian 2004). The temperature of these regions depends directly on optical depth and the ratio of incident (heating) to up-scattered (cooling) luminosity. If the soft excess arises from a hot spot somewhere between the disk and corona, one would expect the temperature of the soft excess to be variable over the range of AGN in which they are observed. In fact, the temperature of the soft excess is rather constant at around 0.1 to 0.15 keV (see Fig. 1.11 in Section 1.2.4). Without invoking some kind of tight correlation between the luminosity ratio and optical depth that scales with black hole mass, observations do not support a hot spot as a reasonable second component.

There is another possible location that was considered by Done et al. (2012, hereafter D12). D12 assumed such a source, which they called the “soft Comptonization”, is located in the accretion disk itself. They argued that disk structures could deviate from the standard Shakura-Sunyaev model

at inner radii, as has been proposed for some of the more extreme Seyfert galaxies like Narrow-Line Seyfert 1s (NLS1s). In particular they consider enhanced dissipation of disk outer layers that would create a Compton up-scattered flux in the soft X-ray band.

D12 took advantage of their experience modeling Comptonized disk emission in black hole binaries to create a similar model for AGN: *optxagnf*. This new model combines disk emission; optically thick, low temperature thermal Comptonization; and optically thin, high temperature thermal Comptonization to cover the full broadband AGN X-ray spectrum. The thick/low Comptonization accounts for the soft excess while the thin/high accounts for the traditional primary continuum. They condition *optxagnf* such that the gravitational energy released in the disk is emitted as the usual blackbody radiation only down to a transition point dubbed R_{corona} or $R_{\rm cor}$. Below $R_{\rm cor}$ the energy can no longer completely thermalize and is divided between the soft excess and the high energy power law tail (Fig. 1.14). D12 stress that the key to their model is that the total luminosity available to power the entire spectrum is defined by: $L_{tot} = \sigma \dot{\rm M} c^2$, where σ is the efficiency and $\dot{\rm M}$ the mass accretion rate. The efficiency is set by black hole spin assuming a standard, steady state accretion disk (Novikov & Thorne 1974)[1].

5.4.2 Spectral Fitting

The merged MOS data were fit with *optxagnf* from 0.5 - 10.0 keV. Black hole mass and luminosity distance were frozen at their known values of $5.9 \times 10^7\,{\rm M}_\odot$ and 233.1 Mpc, respectively. The Eddington fraction was set at $\log(L/L_{Edd})$ = -1.05 as determined by the SED fitting in Section 4.2. For the initial fit, the majority of the parameters were fixed at values recommended by Dr. Chris Done (private correspondence): the slope of the primary component, Γ, was set to 2. The fraction of coronal luminosity emitted as the primary component, $f_{\rm pl}$, was set to 0.3. The electron temperature, $kT_{\rm e}$, and optical depth, τ_e, of the soft excess were set to 0.2 keV and 15, respectively. The parameter $\log R_{\rm out}$ was fixed at 3, corresponding to $1000\,{\rm R_g}$ (the smallest outer radius available). Spin was set

[1] D12 argue that the accretion disk in this scenario deviates from the standard disk paradigm. However, the consequences of the deviation are not expected to influence efficiency.

to $a = 0$ to start and the normalization was perpetually fixed at unity as per model instructions[2]. For this initial model fitting, $R_{\rm cor}$ was the only variable parameter and all parameters were linked across the epochs.

Parameters were gradually unlinked and allowed to vary until the model was established. Corresponding to the primary X-ray emission source, Γ was allowed to vary and was unlinked between epochs. Since the primary component could vary, both $f_{\rm pl}$ and $R_{\rm cor}$ could in theory remain unlinked across epochs as well; however constraining the XMM2 parameters was not possible and so $f_{\rm pl}$ and $R_{\rm cor}$ were kept linked across the epochs but variable. The soft excess is expected to remain relatively constant over time, thus $kT_{\rm e}$ and τ_e were linked between the epochs and allowed to vary.

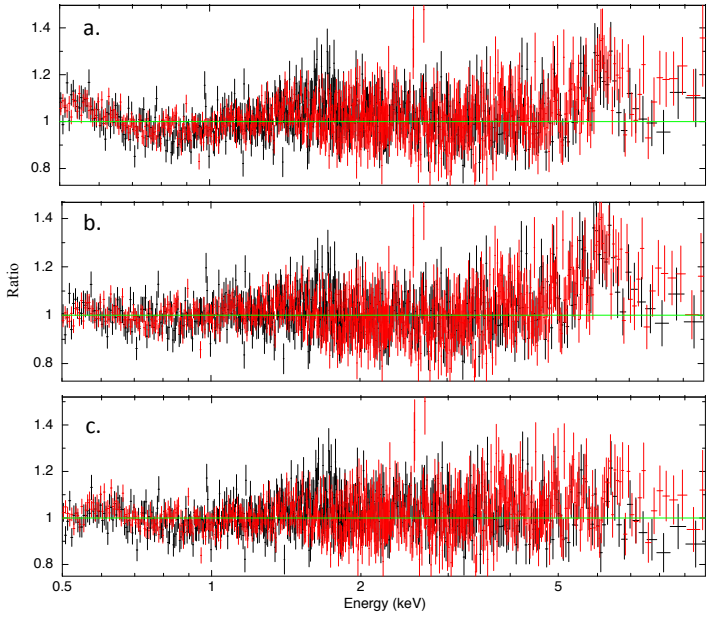

Figure 5.9: Soft Comptonization model residuals for merged MOS spectra fit from 0.5-10.0 keV. Model variations are compared with a. no spin, b. high spin ($a = 0.8$), and c. high spin with a distant, neutral reflector.

[2]https://heasarc.gsfc.nasa.gov/xanadu/xspec/models/optxagn.html

A zero-spin returned a χ^2 = 2522 for 2030 d.o.f. with a clear iron line residual feature and other residual features at $E \lesssim 1$ keV. Fixing the spin at the high value a = 0.8 greatly improved the goodness-of-fit, with $\Delta\chi^2$ = 174 for no change in free parameters. The high spin also took care of low energy residual features, although the iron line continued to be underestimated. Lastly, a distant reflector was added in the same manner as Section 5.3. The distant reflector improved the fit significantly, $\Delta\chi^2$ = 100 for one additional free parameter, and no model residual features remained (see Fig. 5.9).

Table 5.5: Summary for the best soft Comptonization model.

Parameters	**XMM1**	**XMM2**
M_{BH}	$5.9\times10^7\,M_\odot$	...
D_L	233.1 Mpc	...
$\log(L\,/\,L_{Edd})$	-1.05	...
$\log R_{out}$	3	...
a	0.8	...
$R_{cor}\,(R_g)$	12.39±6.86	...
kT_e (keV)	0.94±0.46	...
τ	5.91±1.67	...
Γ	1.80±0.03	1.98±0.02
f_{pl}	0.41±0.17	...
χ^2_ν/ d.o.f.	1.12 / 2031	

An attempt was made to vary a, however the uncertainties were then unconstrained and in many cases the model parameters fell outside reasonable bounds. The soft Comptonization model that most satisfies the data is summarized in Table 5.5 and shown in Fig. 5.10.

While the soft Comptonization model does provide a reasonable fit statistic and good model residuals, the physicality of its parameters may be questionable. The soft excess is described as

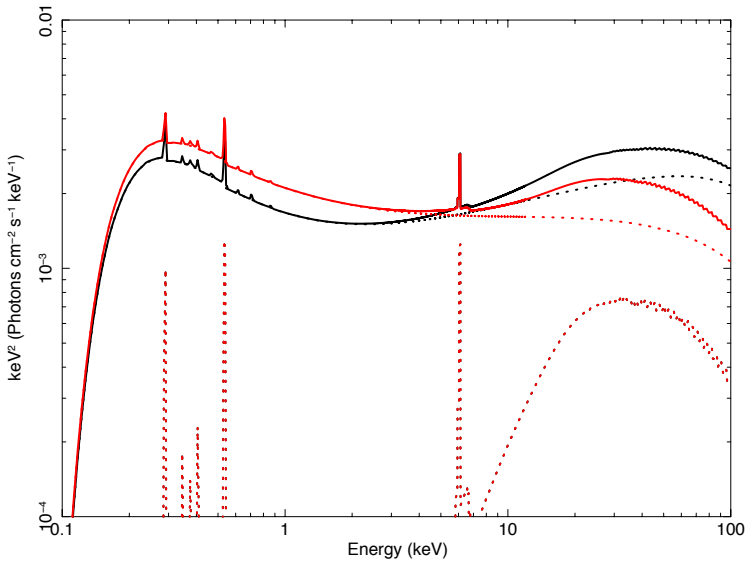

Figure 5.10: The best soft Comptonization model which includes a distant, neutral reflector corresponding to residuals (c) in Fig. 5.9. The model required a spin around a = 0.8 and about half of the primary flux redistributed to the soft Compton component. Spectra were fit to the merged MOS data from 0.5-10.0 keV and the model extrapolated to higher energies. XMM1 is black, XMM2 is red. Model components are dotted lines, the total model is a solid line at each epoch.

having a temperature of 0.94$\pm$0.46 keV: much higher than expected. The temperatures given by the disk model used in Section 4.2, however, range from about (2 - 7)$\times 10^{-3}$ keV. A rough calculation quickly gives the soft excess temperature expected for HE 0436 based on its mass. The M_{BH} - disk relationship gives: $kT \sim 10\,(\dot{m}\ /\ M_8)^{1/4}$ eV, where $\dot{m} = L\ /\ L_{\rm Edd}$ and $M_8 = M_{BH}/\ 10^8$. Using the mass adopted throughout this work for HE 0436 (5.9×10^7 M_{BH}) and the Eddington ratio predicted by the SED fitting in Section 4.2, the temperature of the soft excess in HE 0436 is approximately 6.25×10^{-3} keV. In comparison, the temperature given by soft Comptonization is over 200$\times$ larger. The soft excess component in the *optxagnf* model is composed of *both* the high energy tail of the Big Blue Bump (Section 1.1.4) and the soft Compton component. It is not possible to determine which fraction of the total soft excess temperature is made up by the Big Blue Bump and so any temperature comparison is purely speculative.

One must also consider that the theory behind this model requires the inner regions of the disk, $r \leq R_{\rm cor}$, to be in a non-standard state. It is assumed that the disk can no longer thermalize inward from $R_{\rm cor}$ and it is in this region that the soft excess emission originates for this scenario. Therefore, the temperature of the soft Compton region may be higher than that of the disk inside of $R_{\rm cor}$. This requires, however, that the soft Compton region – an optically thin plasma sandwiching the accretion disk – be thermally isolated from the disk. As standard accretion disks are considered to be in local thermodynamic equilibrium (LTE) for most purposes, a non-LTE approach (e.g. Hubeny et al. 2001) would be required to model any region inside $R_{\rm cor}$, but that is beyond the scope of this study. Based on the complex nature of the soft Comptonization scenario, all further analyses focused on the best models for absorption and reflection only.

Chapter 6

Timing Analysis

6.1 *XMM-Newton* Light Curves

Source photons were extracted to create light curves in a variety of energy bands between 0.2 - 12.0 keV, including a broadband 0.2 - 12.0 keV bin, in the same manner as described in Section 2.2. Upon visual inspection, XMM2 showed more variability than XMM1, although the XMM2 observation was nearly double the duration of XMM1 ($\sim$130.5 ks vs. 70.5 ks) and so the light curve of the former contained more information.

The light curves from all EPIC instruments that collected data proved consistent in the XMM1 and XMM2. All subsequent timing analyses utilized MOS data only. In an effort to improve the signal-to-noise ratios, MOS 1 and 2 light curves were combined at each epoch, taking care to match the exact observation start and stop times. The 0.2 - 12.0 keV merged MOS light curve for each epoch is shown in Fig. 6.1.

While light curves illustrate the changes in flux over time, it could be more useful to examine *how* the flux changes. For example, to see if the spectra vary in distinct energy bands or at specific moments in an epoch.

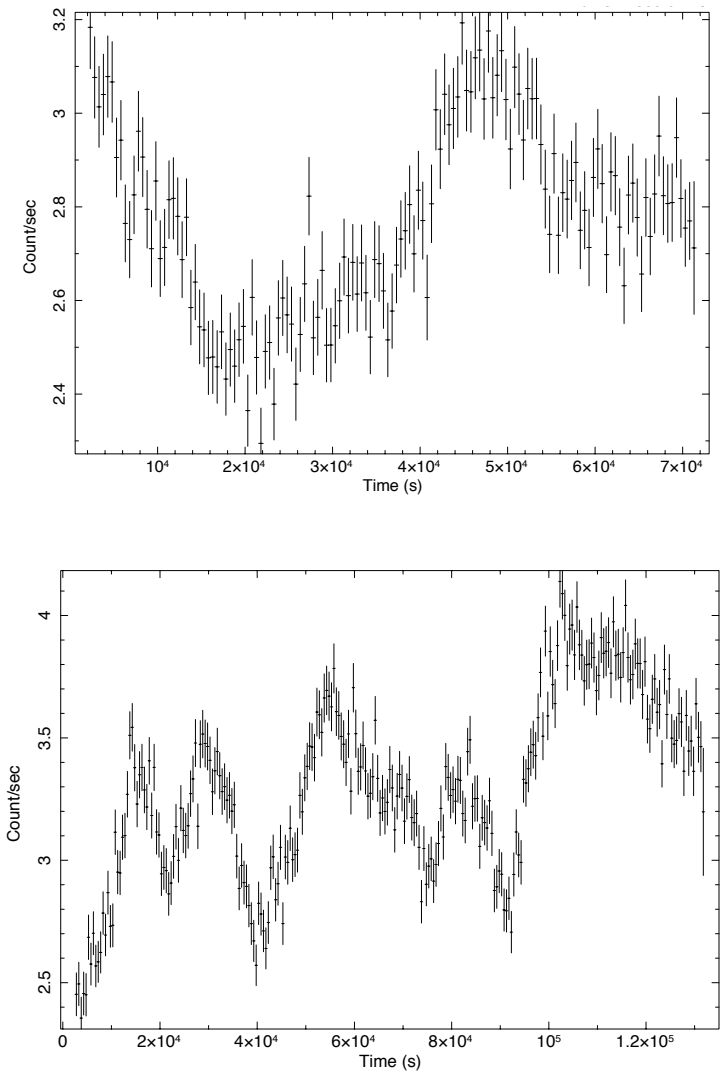

Figure 6.1: Merged MOS light curves for both XMM1 and XMM2 binned at 500 s each. XMM2 had nearly double the exposure time and also appears to display more variability.

6.2 Hardness Ratios

Ratios of softer energy band count rates over those of a harder energy band were calculated for four energy band pairs between 0.2 - 12.0 keV range. These hardness ratios (HR) were analyzed two ways at each epoch: flux-dependent HR; and as time-dependent, normalized HR. The flux-dependent HR (HRvF) examines if the spectra vary as the flux changes, while the time-dependent HR (HRvT) looks at when the spectra are varying. As the ratio values depend only on the energy bands being compared, any variability is exposed in the shape of the plots.

The HRvF does not reveal any significant variability in the spectra at either epoch with respect to the AGN flux (Fig. 6.2). This does not mean the spectra are not variable, but only that any variability is not restricted to a specific flux state.

The HRvT analysis has similar results (Fig. 6.3). For clarity, plots of the soft-band HRvT alone were compared side-by-side for both epochs. Fig. 6.4 shows the XMM2 data. Within the calculated uncertainties it appears there is little time-dependent variation in the soft bands over time. This is contrary to the XMM2 broadband light curve which shows several significant peaks throughout its $\sim$130.5 ks observation. However, G10 list a normalized HR value of -0.46$\pm$0.10 for the 0.3 - 1.0 keV vs. 1.0 - 10.0 keV bands – a value consistent with the trend seen in the 0.2 - 0.8 keV vs. 2.0 - 12.0 keV HRvT plot.

All HR trends for the X-ray data are nearly linear within uncertainties and so indicate little to no spectral variability with respect to either flux or time.

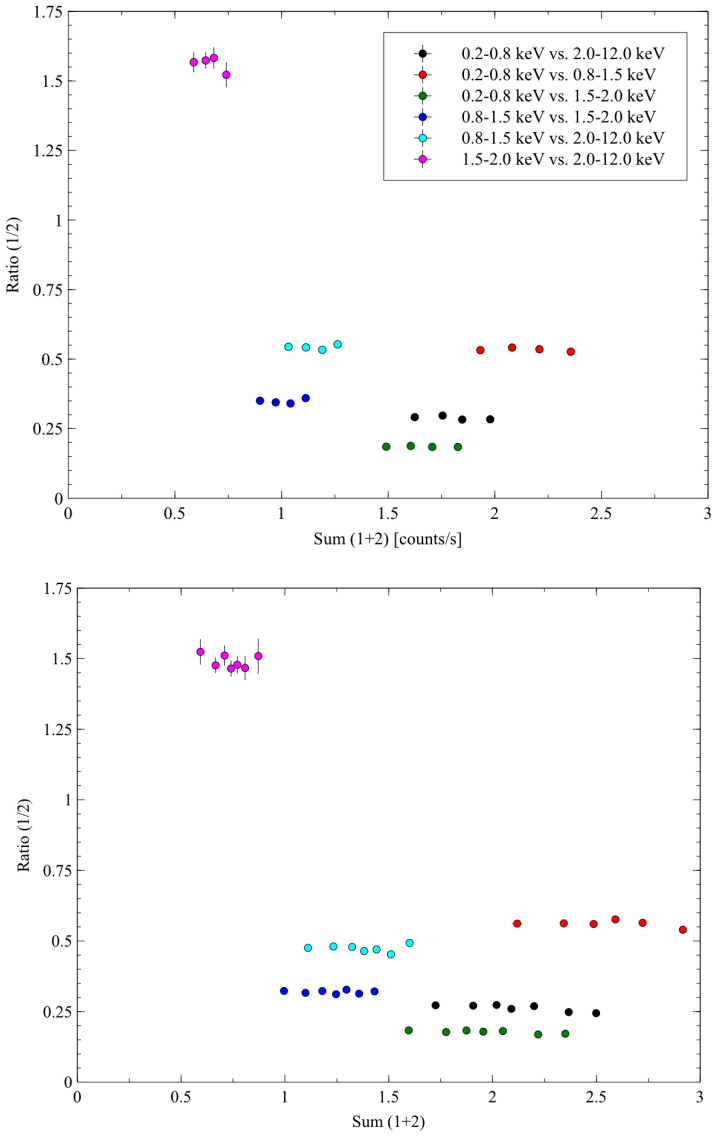

Figure 6.2: Hardness ratio dependence on flux in light curves for both XMM1 (left) and XMM2 (right). Light curves were binned at 500 s and divided into four energy bins with ratios determined for each pairing. All data points include error bars, however most are not resolved on this scale. XMM2 had nearly twice the exposure time allowing for more data points.

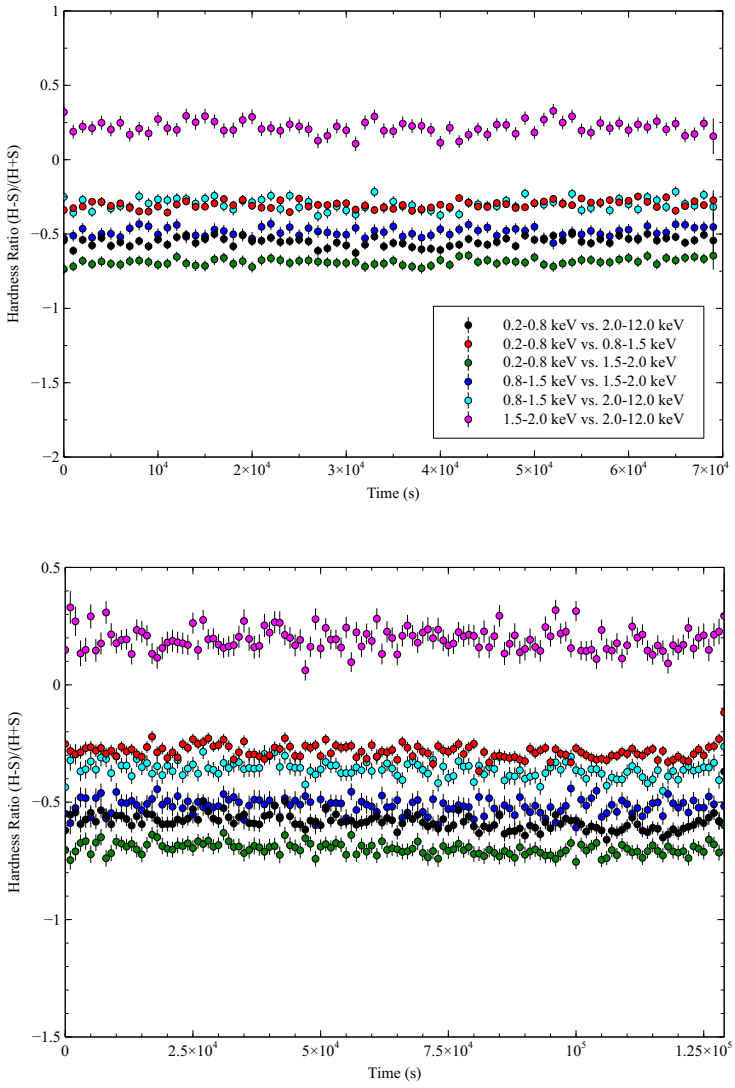

Figure 6.3: Normalized hardness ratio dependence on time in light curves for both XMM1 (left) and XMM2 (right). Light curves were binned at 500 s and divided into four energy bins with ratios determined for each. XMM2 had nearly twice the exposure time.

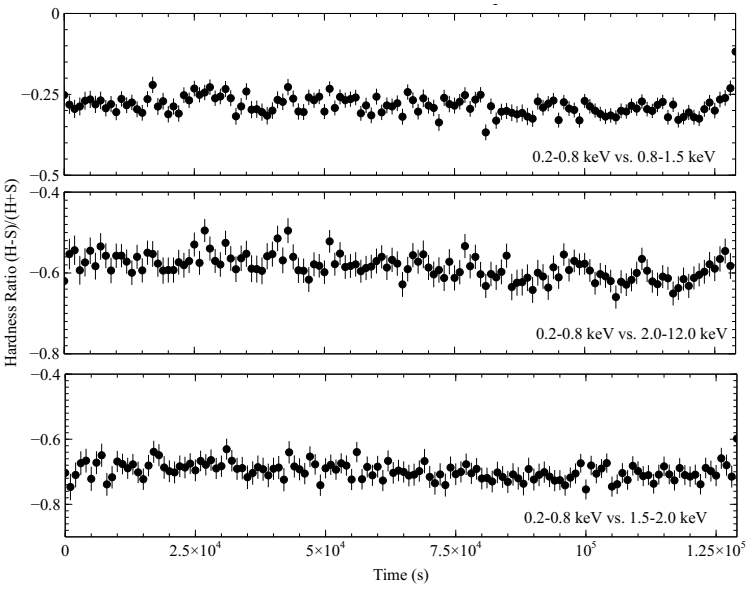

Figure 6.4: XMM2 normalized hardness ratio dependence on time for soft energy bands only. Light curves were binned at 500 s. Despite noticeable changes in flux in the XMM2 light curve, no time-dependent variability is detected in this measurement.

6.3 Fractional Variability

The fractional variability amplitude, $F_{\rm var}$, is a useful measurement used to quantify the intrinsic variability of a light curve while also accounting for uncertainty in the light curves. The $F_{\rm var}$ compares the amplitude of any variations present in each energy band to determine if the amplitudes in one energy band are larger than those in another. It is useful to follow the HR analysis with a look at fractional variability because there could be a scenario in which, say, the soft energy band varies with greater amplitude than the hard. However, if those variations appear at the same moment in time the HRvT profile will continue to be constant. The $F_{\rm var}$ thus compares the relative "strengths" of observed variability across two energy bands, independent of time or flux.

The $F_{\rm var}$ is defined as,

$$F_{\rm var} = \frac{1}{\langle X \rangle} \sqrt{S^2 - \langle \sigma_{\rm err}^2 \rangle} \tag{6.1}$$

where $\langle X \rangle$ is the mean count rate, S^2 the total variance of the light curve, and $\langle \sigma_{\rm err}^2 \rangle$ the mean error squared. In calculating the uncertainties on $F_{\rm var}$ ($\sigma_{F_{\rm var}}$), Edelson et al. (2002, hereafter E02) assume all variance within a time bin to be caused by measurement error and thus defined $\sigma_{F_{\rm var}}$ to be:

$$\sigma_{F_{\rm var}} = \frac{1}{F_{\rm var}} \sqrt{\frac{1}{2N}} \frac{S^2}{\langle X \rangle^2} \tag{6.2}$$

where *N* is the number of time bins (see Appendix in E02). The uncertainties determined in this fashion are quite conservative.

Ponti et al. (2004, hereafter P04) offered an alternative method whereby $\sigma_{F_{\rm var}}$ is calculated using standard error propagation:

$$\sigma_{F_{\rm var}} = \frac{\sqrt{\sum_{i=1}^{N} [(x(E, \Delta t_i) - \langle x(E) \rangle) \sigma_{x(E,\Delta t_i)}]^2}}{\langle x(E) \rangle \sqrt{(N-1) \sum_{i=1}^{N} [x(E, \Delta t_i) - \langle x(E) \rangle]^2}} \tag{6.3}$$

In the uncertainty defined by P04, *x(E,*Δt_i*)* is the count rate in the energy bin *E* during time bin

Δt_i[1], $\langle x(E) \rangle$ is the mean count rate of the entire observation at energy bin *E*, and $\sigma_{x(E,\Delta t_i)}$ is the uncertainty associated with $x(E,\Delta t_i)$. P04 assumed any error in $\langle x(E) \rangle$ would be negligible compared to $\sigma_{x(E,\Delta t_i)}$. This method is more sensitive to small variations in $F_{\rm var}$, but should be used with high count rates in order to satisfy its condition that the bins chosen for the calculation be such that there will be insignificant random noise (see Appendix in P04).

$F_{\rm var}$ was calculated for both epochs using merged MOS light curves. The light curves were binned at 1000 s and a total of nine energy bins were used spanning 0.2 - 10.0 keV, the data above 10 keV ignored due to the low signal-to-noise. Both equations 6.2 and 6.3 were used to calculate $\sigma_{F_{\rm var}}$ for the preliminary analysis. However, only the plots calculated with P04 uncertainties are shown. These reveal slight differences in the amplitude of the variations from one energy band to the next. XMM2 displays a higher $F_{\rm var}$ than XMM1 overall, which is apparent in the light curves.

It could be useful to see if the best spectral models (Chapter 5) could describe the $F_{\rm var}$ seen from the light curves. We considered if solely variation in the power law could account for the shape of the $F_{\rm var}$ spectrum. The fraction that the power law contributes to each energy band ($F_{\rm var}^{\rm M}$) is overplotted on the $F_{\rm var}$ spectrum for both the best-fit partial covering and blurred reflection models (Fig. 6.5).

The best absorption model predicts an $F_{\rm var}$ profile that is very different from the observed $F_{\rm var}$ (top panel, Fig. 6.5). It is unusual, though, to assume that the primary emitter would be the sole cause of variability in the absorption scenario instead of the covering fraction (e.g. Turner & Miller 2009). Such a condition would require the variations be due only to changes in the incident primary emission.

On the other hand, the best reflection model predicts a variability that is closer to agreement with observations (lower panel, Fig. 6.5). The assumption about the primary emitter is more justified in the reflection scenario, but the $F_{\rm var}$ model profiles illustrate that there continue to be some discrepancies in how the variability is described by best-fit spectral models.

[1] $\Delta t_i \times$ [exposure time] = *N*

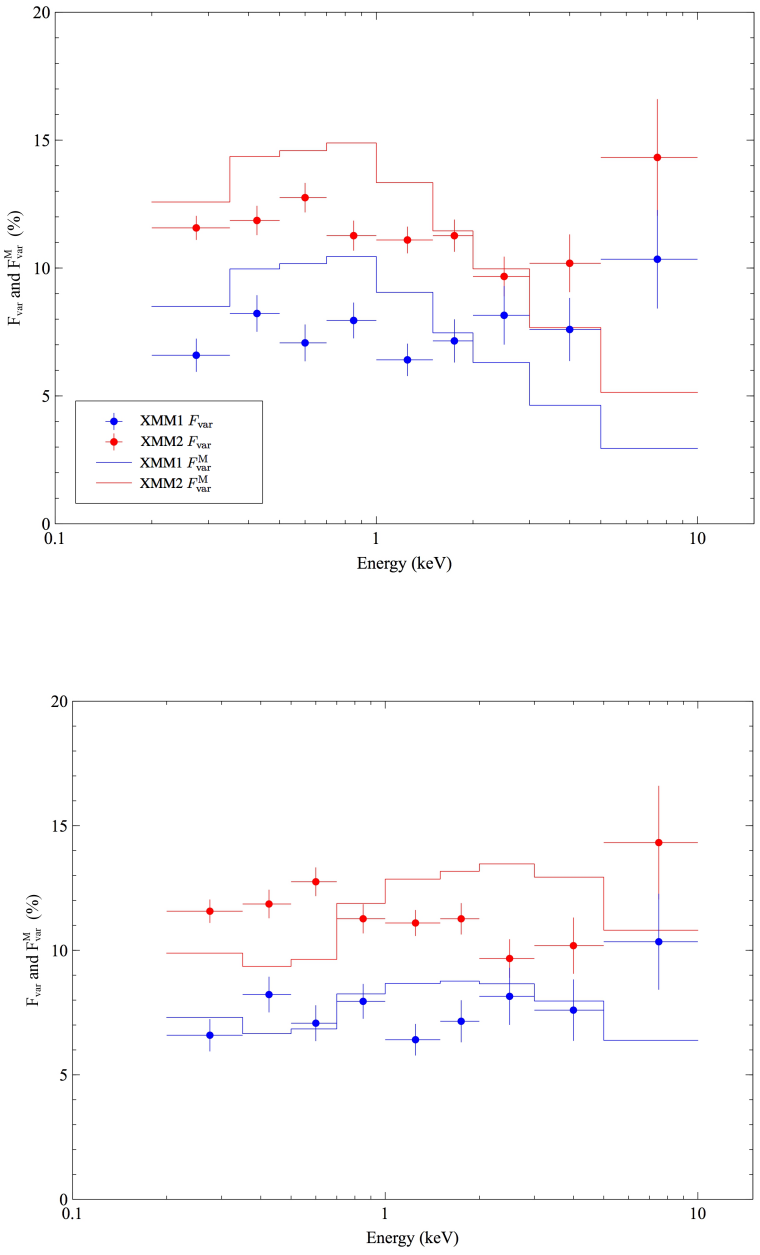

Figure 6.5: Fractional Variability analysis with the best absorption (top) and reflection (bottom) model predictions. The fraction that the power law contributes to each energy band is overplotted on the $F_{\rm var}$ spectrum for both XMM1 (blue) and XMM2 (red).

6.4 Flux-Resolved Spectra

Flux-resolved spectra were made in a final effort to resolve the mechanism(s) behind short-term variability in HE 0436. As the XMM2 observation was considerably longer and shows larger amplitude variations, data from the second epoch alone were used to create X-ray spectra with $< 3\,\mathrm{count\,s^{-1}}$ and $> 3\,\mathrm{count\,s^{-1}}$.

A difference spectrum (high flux – low flux) was created between the two spectra. A power law was fit to the 3 - 10 keV band and extrapolated to lower energies (Fig. 6.6). If changes in the normalization of the spectral components alone were truly responsible for variability in the broadband X-ray spectra, a lone power law should describe the difference spectrum well. The 3 - 10 keV data are fit well with a power law with a slope of 2.00 ± 0.16, but this does not extend to lower energies. Normalization changes may be responsible for the majority of variability in the broadband spectra, however changes in the shape of the spectral components are also expected.

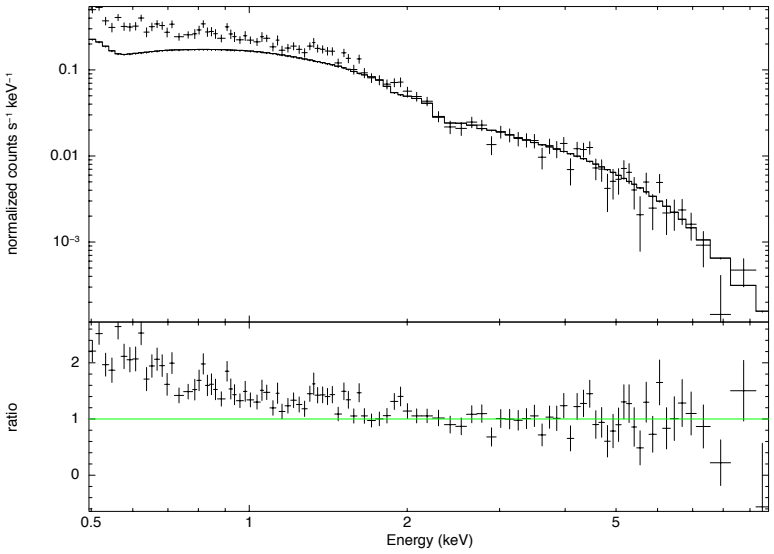

Figure 6.6: The XMM2 difference spectrum fit with a power law from 3 - 10 keV and the model then extrapolated to lower energies. If the normalization changes alone were responsible for variability, a lone power law should describe the difference spectrum well. Residual features remain in the soft X-ray band indicating some variability must be attributed to another source.

absorption

The two flux-resolved spectra were then fit with the best models for absorption and reflection (see Table 6.1) in hopes of constraining the individual parameters responsible for the rapid variability. In the absorption model, changes in X-ray flux could be caused by either the primary emitter or by the absorbing material. Two sources of ionized absorption explain the broadband spectra best (Section 5.2), one with higher column density than the other. Geometrically, these could represent two distinct absorbing materials or a single absorber with a density gradient. Ionization could also vary across a single larger body as the material closer to incident radiation would experience more illumination than that on the far side. As absorbing material moves, overlaps, or condenses/disperses a spectrum can change (see Fig. 5.1). The simplest scenario assumes variability caused only by a change in covering fraction, with all other properties of the absorbers remaining constant.

Allowing only the covering fractions to vary between flux states in the absorption model returned χ^2= 909 for 768 d.o.f. and moderate residual features. There was a small discrepancy in the spectra around 5 keV where the model over-predicted the low flux state and under-predicted the high flux state. In addition, only the covering fraction of the denser absorber changed significantly and so the model was revised. With the covering fraction of the denser absorber alone providing the variability, the fit statistic stayed approximately the same for an additional free parameter and the residuals improved. The model described the data equally well if the column density of the denser absorber was allowed to vary with the covering fraction (Fig. 6.7). This scenario makes sense as two overlapping bodies would alter both the total covering fraction and column density along the line of sight.

A comparative fit was found when the power law parameters alone were allowed free to vary between flux states. It was mentioned above how this scenario is much more difficult to justify; a change in the covering fraction could easily account for short-term variability on kilosecond timescales, but it is challenging to imagine a mechanism that would force the slope of the power law

to fluctuate so quickly. Therefore, the best explanation for the short-term variability using absorption is a partial covering model (hereafter PC model) where a cloud of denser material is moving into the line of sight as another cloud with lower density continues to obscure the same solid angle.

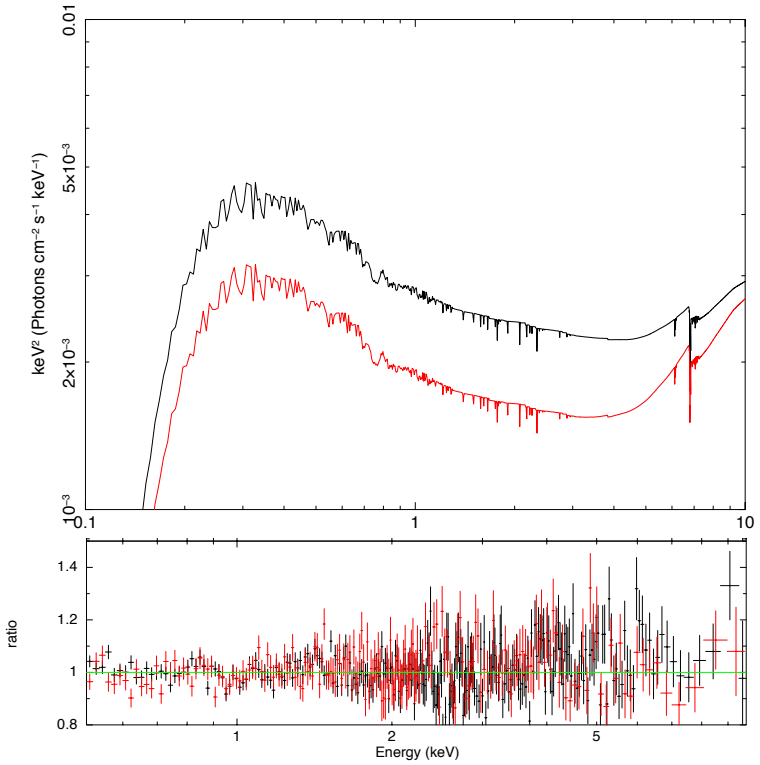

Figure 6.7: The best partial covering model fit to the flux-reduced spectra. The models for both the high-flux (black) and low-flux (red) spectral states are shown in the top panel. Model residuals for both states are shown in the panel below.

blurred reflection

A similar procedure was followed for testing reflection with the flux-resolved spectra. From past analysis (Section 5.3) it appears the the X-ray spectra are power law dominated and that changes in the normalization of the primary emitter itself drive most of the short-term variability (Fig. 6.5). As the primary emitter brightens or perhaps moves along the axis of rotation, the emissivity profile of the disk alters and material at closer radii experiences a change in ionization. When considering the scenario of a moving "lamp post" corona emitting isotropically, upward motion would decrease primary X-ray radiation on the inner disk and result in a harder, power law-dominated X-ray spectrum. Downward motion of the corona would cause the disk to be illuminated anisotropically due to light bending, increasing the reflected flux from the inner region and producing a softer, reflection-dominated spectrum (Fig. 6.8).

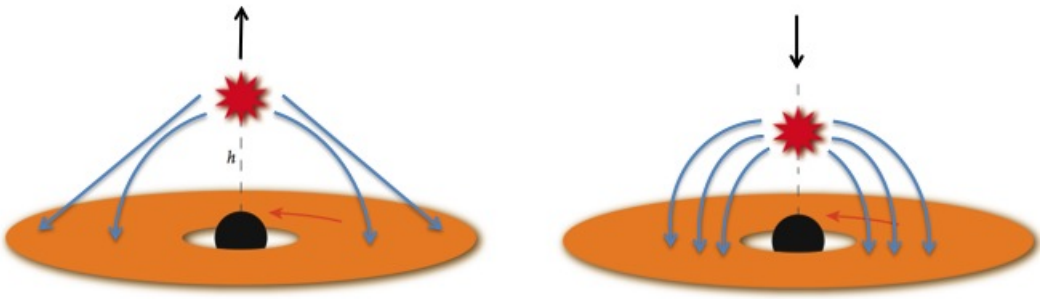

Figure 6.8: Coronal motion along the axis of rotation can perhaps explain X-ray spectral states. This scenario assumes a "lamp post" corona emitting isotropically. As the corona increases in height above the disk (left) the reflection component decreases, resulting in a harder, power law-dominated spectrum. As the corona lowers (right), the inner disk is disproportionately illuminated due to light bending, increasing the reflected flux and producing a softer, reflection-dominated spectrum. Figure credit: adapted from Wilkins & Fabian 2012, Fig. 3.

The best reflection model was applied to the flux-resolved spectra with all but the power law parameters frozen and returned a fit of χ^2 / d.o.f. = 937 / 774. The slope of the power law of the high state was unusually high, around Γ = 2.17, although the slope of the minimum state was reasonable, around Γ = 2.09. Allowing ξ to vary dropped the power law slopes and improved the

statistics by $\Delta\chi^2$ = 23 for one additional free parameter. Unlinking ξ improved the fit further by $\Delta\chi^2$ = 37 for another additional free parameter and brought Γ into comparable range across the flux states. Linking Γ produced the best representation of the data with the same goodness-of-fit for an additional degree of freedom. While remaining high, Γ was more reasonable at around 2.12 – lower than the value found for the absorption model. Other parameters were allowed to vary one at a time to judge their influence on the model, but none improved the fit. The emissivity profile parameters were also allowed to vary between states both individually and as a set of three, with no improvement.

The best reflection model utilizing *kdblur2* (Section 5.3.1) was also fit to the flux-resolved spectra (Fig. 6.9). Like the *relconv* model before it, the *kdblur2* model also produced better fits when Γ was linked across states and ξ remained free. The best fit to the flux-resolved spectra returned residual features that appeared identical to those of *relconv* and improved the fit statistic by $\Delta\chi^2$= 4 for the same d.o.f. While both models describe the same scenario, there appear to be some complications with the *relconv* fits that are unclear. Therefore the *kdblur2* interpretation is favored as it finds a lower Γ, around 2.10, for an improved fit statistic and is an overall simpler model. An unusually low iron abundance and moderate black hole spin continues to be required in either case.

It is interesting to note that changes in neither ξ nor power law normalization were required for the reflection model describing the average X-ray spectra (see Table 6.1). On the contrary, Γ was the variable parameter in the average case. Ionization is expected to vary with the primary emitter and so it could be that the average spectra were simply not sensitive to the smaller changes in ξ that accompanied the changes in primary flux. Also, the flux-resolved spectra are sensitive to short-term variability only. The increase in Γ seen across epochs XMM1 and 2 is a long-term variation most likely due to a separate mechanism than the one causing fluctuations in power law normalization observed within an epoch itself.

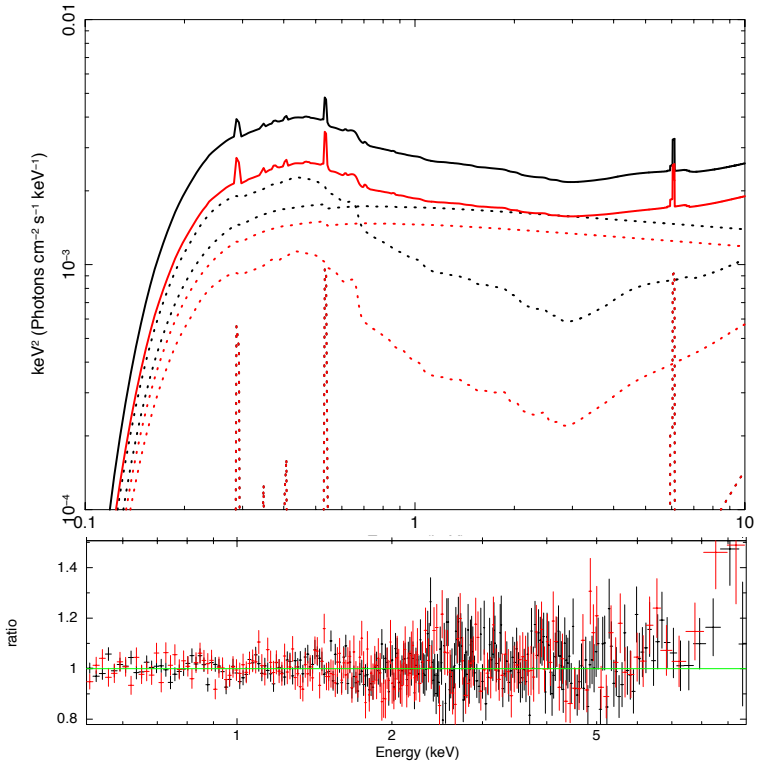

Figure 6.9: The best reflection model utilizing *kdblur2* fit to the flux-reduced spectra. The models for both the high-flux (black) and low-flux (red) spectral states are shown in the top panel. Model residuals for both states are shown in the panel below. A model using *relconv* resulted in comparable fits.

Table 6.1: Summary of absorption and reflection models for the flux-resolved spectra.

Model	Component	Parameters	high-flux state	low-flux state
PC Absorption	Absorber 1	Γ	$2.40^{+0.04}_{-0.01}$	...
		$N_{\rm H,1}$ ($\rm cm^{-2}$)	$51.17^{+7.67}_{-8.17}$	...
		CF_1	$0.62^{+0.05}_{-0.06}$	$0.74^{+0.03}_{-0.04}$
	Absorber 2	$N_{\rm H,2}$ ($\rm cm^{-2}$)	$6.00^{+1.14}_{-1.44}$	...
		CF_2	$0.32^{+0.06}_{-0.03}$	...
		χ^2_ν/d.o.f.	1.18 / 769	
PLD Reflection	Blurred Reflector	Γ	2.10±0.01	...
		norm ($\rm ph\,keV^{-1}\,cm^{-2}\,s^{-1}$)	$1.76\pm0.11 \times 10^{-3}$	$1.50^{+0.05}_{-0.07} \times 10^{-3}$
		$\alpha_{\rm in}$	7.0	...
		$\alpha_{\rm out}$	3.0	...
		$R_{\rm br}$	5.0 $\rm R_g$	...
		$R_{\rm in}$	2.0	...
		θ (°)	40.0	...
		Fe (solar)	0.27	...
		Γ	$\Gamma_{\rm primary}$	...
		ξ ($\rm erg\,cm\,s^{-1}$)	$292.04^{+19.97}_{-1826}$	$187.82^{+17.14}_{-18.53}$
	Distant Reflector	Fe (solar)	1.0	...
		Γ	1.9	...
		ξ ($\rm erg\,cm\,s^{-1}$)	1.0	...
		χ^2_ν/d.o.f.	1.13 / 773	

Chapter 7

Discussion and Conclusions

The multi-epoch, multi-band analysis of HE 0436 has resulted in two distinct scenarios that describe the spectra of the object equally well on a purely statistical basis. In the first interpretation, emission from the central engine passes through at least one ionized body of gas that absorbs the incident radiation. The spectrum produces an apparent soft excess that is an artifact of the absorption.

The second model describes the X-ray emission as a composite of multiple sources. Here, the primary source dominates over emission from blurred, ionized reflection and a distant, neutral reflector. The Fe Kα line seen in this case is a sum of the relativistically broadened iron line originating from the inner regions of the accretion disk and a narrow line from the distant reflector. The soft excess is a consequence of blurred ionized reflection from the inner regions of the accretion disk.

It is not unusual for both absorption and reflection to model a spectrum equally well (e.g. Mrk 335: Longinotti et al. 2013, Gallo et al. 2013; NGC 1365: Risaliti et al. 2013, Miller & Turner 2013). While it is reasonable to assume that both reflection and absorption mechanisms can be present in a single object, the degeneracy between the models can lead to confusion when attempting to reconstruct source geometry. Timing analysis can be used in an attempt to constrain the physicality of either of the two models, in hopes of discovering a more favorable scenario, but more

often than not both the reflection and absorption interpretations are statistically indistinguishable below $\sim$10 keV. It is only when the models are extrapolated to the harder X-ray that the spectral profiles predicted by absorption and reflection begin to differ significantly (Fig. 7.1).

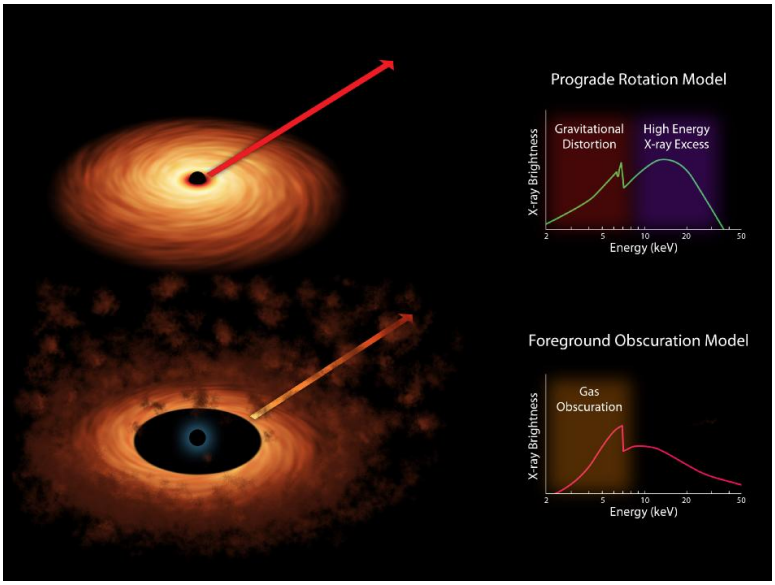

Figure 7.1: Illustrations of the relativistic and absorption effects used to explain a broadened iron line in the X-ray reflection spectrum. Emission originating from close to the black hole experiences multiple relativistic effects that broaden the iron line (top). Emission originating from a larger ISCO can be absorbed which attenuates the reflection spectrum redward of the iron line (bottom). In both scenarios, a "red wing" is produced in the line and the two scenarios can often be statistically indistinguishable. The degeneracy may be broken by examining the spectra $>$10 keV. Image credit: NASA/JPL-Caltech.

The PC and reflection models predict certain broadband spectral profiles and short term behavior that can be observed. The following sections describe efforts to compare these predictions to observations in an effort to break the degeneracy of the two models.

7.1 Absorption Predictions

Section 5.2 discussed how photoelectric absorption would also result in additional atomic features in an X-ray spectrum as a fraction of the incident radiation re-emitted by fluorescence. The strength of the fluoresced lines is dependent upon the fluorescent yield of an element. Since

iron has a high fluorescent yield (0.347 for neutral iron), it is reasonable to expect that significant absorption would lead to a strong Fe Kα line that can be observed.

In the absorption models analyzed previously, no iron line feature of any kind was included in order to establish a conservative prediction on the strength of the iron line expected to be present with such a model. If an iron feature is not seen with the flux that would have been produced by the absorbers alone, then this calls into question the source of the observed iron line. A discrepancy between the predicted line strength and that observed would also make it all the more difficult to consider a scenario in which the absorption attenuates a distant, reflected spectrum (e.g. originating from an accretion disk at large radii) without resorting to a fine-tuned model.

The strength of an Fe Kα emission line that would be produced from the denser of the two absorbers in the partial covering model was calculated by multiplying the absorbed 7 - 20 keV photon flux by the fluorescent yield of neutral iron (0.347). A Gaussian line with the predicted (neutral) iron flux (in the frame of the source) was then inserted in the absorption model. The model prediction was visibly compared to the data at both epochs and the respective equivalent widths (EWs) of the predicted iron lines were calculated.

The predicted fluxes were found to be $2.70\times10^{-13}\,\mathrm{erg\,cm^{-2}\,s^{-1}}$ for XMM1, $2.55\times10^{-13}\,\mathrm{erg\,cm^{-2}\,s^{-1}}$ for XMM2. If such lines were present in the average X-ray spectra, their respective EWs would be 0.21 keV and 0.20 keV. The EWs found during the initial analysis of the 3 - 10 keV band spanned from $\leq$0.05 keV to around 0.35 keV and so it seems such lines could be possible.

However, any Fe Kα emission produced by the warm absorbers would manifest as a narrow feature and the lines with comparable EWs from the initial iron line analysis were all broad. A narrow Gaussian line with the predicted strengths for both epochs was inserted into the PC model and the residuals are shown in Fig. 7.2. A strong iron line is predicted by the absorption model that is not seen in the data.

As explained above, an Fe Kα flux produced from absorption alone would be a lower limit on iron features observed from distant reflectors. Since the PC model predicts a line strength greater than what is seen in the spectra, it seems unlikely that absorption alone can describe the X-ray

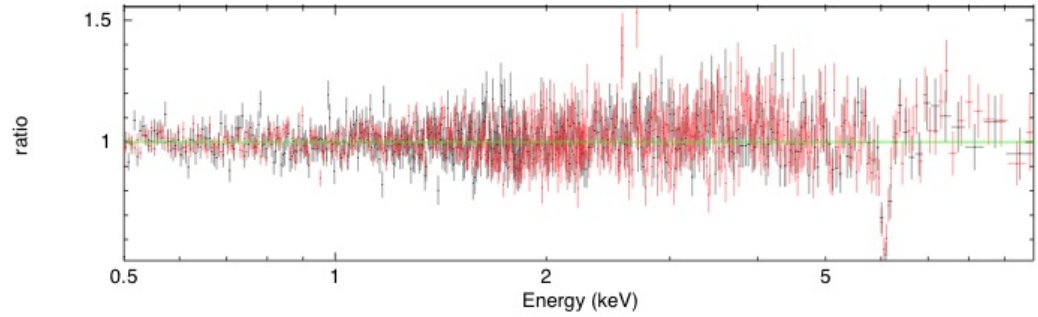

Figure 7.2: Residuals produced by the PC model when a Fe Kα line feature is added with the strength predicted by the 7-20 keV absorbed flux, assuming the fluorescent yield of neutral iron only. The line strength is a lower limit on any iron feature produced by distant reflection attenuated by absorption. The model is compared to the merged MOS data where XMM1 is black, XMM2 is red.

spectra of HE 0436.

The atomic features produced by absorption are not limited to the iron line band, though. The reflection fraction, *R* = EW / 180 eV, predicted by the absorption scenario is 1.17 and 1.10 for XMM1 and 2, respectively. An isotropic corona illuminating a flat, neutral accretion disk is expected to have a reflection fraction of R $\sim$ 1 (Ballantyne et al. 2003) and so the value found here for the absorption-predicted iron line agrees with the standard case.

Using the *R* values, the flux from 20 - 50 keV that would be produced by partial covering was estimated using *pexrav*: a model that describes neutral reflection of an exponentially cut off power law spectrum (Magdziarz & Zdziarski 1995). The high energy flux also overestimates the data (red curve in Fig. 7.3). Like the predicted iron line strength, this too is a lower limit for the absorption scenario as Compton scattering is prominent above 10 keV and is not accounted for in this model.

Miller & Turner 2013 (hereafter MT13) stress the importance of including Compton scatter effects produced by absorption in the higher energy bands, particularly for Compton-thick absorbers (i.e. $N_{\rm H} \gtrsim 1.5 \times 10^{24}\,{\rm cm}^{-2}$). They point to the hard X-ray excess observed in local AGN by Tatum et al. (2013) to emphasize the ubiquity of the Compton hump (Section 1.1.4) in Type I objects. Current absorption models commonly used to fit AGN broadband X-ray spectra do not include scattering and thus underestimate the hard X-ray flux. In the analysis of HE 0436, however, this work has shown that a PC scenario requires a higher flux in the 20 - 50 keV band without yet including scattering

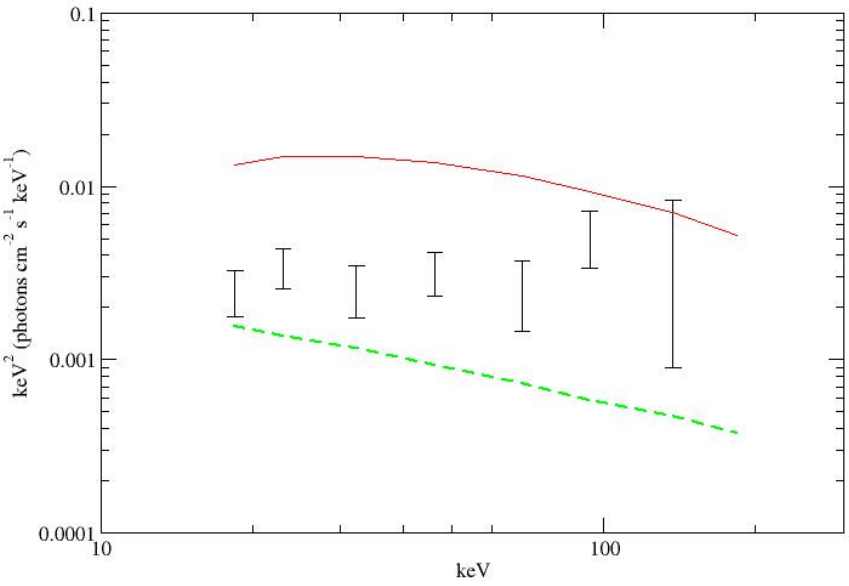

Figure 7.3: The reflection fraction predicted by the partial covering model is used to estimate the flux between 20-50 keV (red), extrapolated here for comparison with the *Swift* BAT data (black). Like the predicted Fe flux, this too is a lower limit for the absorption scenario as Compton scattering is prominent above 10 keV and is not accounted for in this model. The partial covering model alone is also extrapolated (green, dashed) and does not include the additional remitted flux from absorption.

effects.

It is also important to note that Γ remained high in both the ionized and neutral absorption scenarios at $\sim$2.60 (see Tables 5.1 and 5.2). The initial broadband analysis in Section 3.1 found $\Gamma = 2.23^{+0.10}_{-0.05}$ and the maximum slope found in the 3 - 10 keV fitting (Section 3.2) was $\Gamma = 1.86^{+0.07}_{-0.06}$. A value of around Γ = 2.60 exceeds the range found in the majority of Type I AGN of $\sim$1.9.

The partial covering model describes the X-ray spectra from HE 0436 statistically well and cannot be ruled out based on goodness-of-fit alone. However, a consequence of the absorption scenario requires other spectral features that are simply not seen. Predictions from the reflection scenario must also be analyzed in a similar fashion in order to determine which case – if either – best describes the observations.

7.2 Reflection Predictions

Like the partial covering scenario, a reflection interpretation also predicts a certain high-energy spectral profile that can be compared to the *Swift* BAT data. The power law-dominated reflection model outlined in Section 5.3 was extrapolated up to 100 keV and compared to the *Swift* BAT data (Fig. 7.4). The model is consistent with most of the high-energy data and while the uncertainties for BAT are larger than those of the MOS, the consistency confirms that a reflection prescription in general is a better fit for HE 0436. For simplicity, XMM1 alone is shown in Fig. 7.4; the model for XMM2 also fell within the BAT ranges. The simpler *kdblur2* reflection model was also tested and was in agreement.

Variability is also described well with reflection, as it appears that changes in flux of the primary emitter can be seen influencing both the short- and long-term behavior of the object. Assuming an isotropic, "lamp post" corona, changes on kilosecond timescales reflect an increase/decrease in primary X-ray flux with respect to the accretion disk. The changes in flux could either be intrinsic or due to the motion of the corona which in turn increases/decreases the ionization of the disk at inner radii. Over longer, multi-year timescales fluctuations in power law slope can be seen which would be caused by physical changes in the corona itself (i.e. an alteration in temperature and optical depth). HE 0436 remains in a power law-dominated state throughout the observed epochs.

The X-ray spectra of HE 0436 continues to leave a few challenges, however. While the reflection interpretation is robust enough to describe this object in general it insists on an unusually low iron abundance. Observations have shown that most AGN have solar to super-solar metallicity values independent of redshift (e.g. Storchi-Bergmann et al. 1998, Hamann et al. 2002). In several independent studies, it was shown that most AGN are also located in massive galaxies with classical bulges (Green & Ho 2004, Barth et al. 2005). As stellar mass is strongly correlated with metallicity (Tremonti et al. 2004), it is reasonable to expect the majority of AGN to thus have solar metallicity values or higher. The question then arises: under what circumstances would AGN be observed with (apparently) intrinsic sub-solar metallicities?

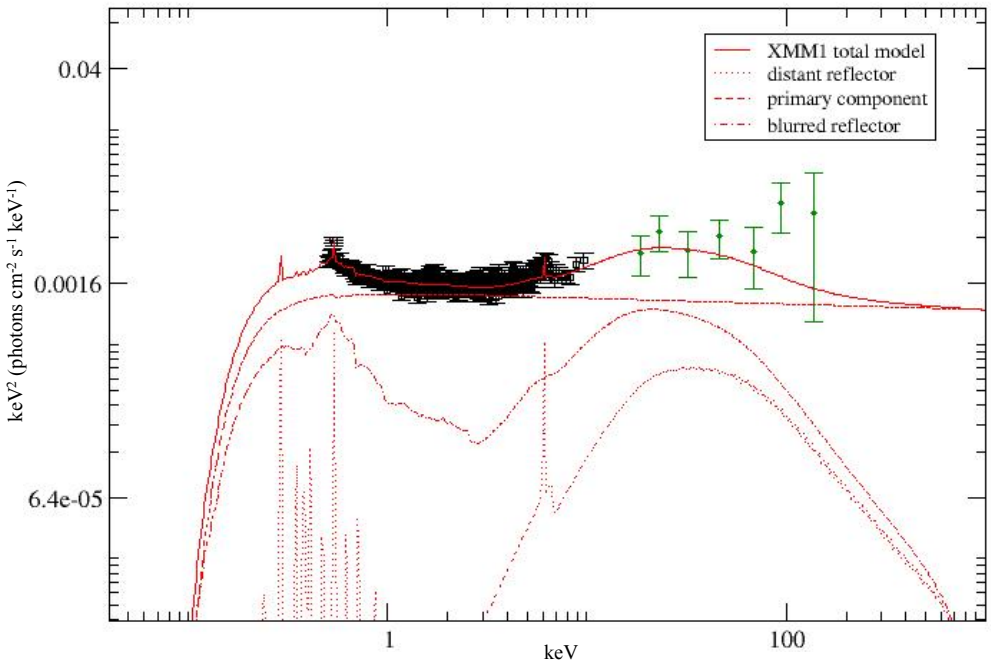

Figure 7.4: The *relconv* reflection model fit to the merged MOS XMM1 data (black) in the 0.3-10.0 keV band and extrapolated into the *Swift* BAT regime. The BAT data are green. For simplicity, only the first epoch of this model is shown although that of XMM2 and the simpler *kdblur2* variation are both consistent. The high-energy turnover above 100 keV is not included in the power law model here.

Groves et al. (2006) set out to find such AGN and searched SDSS observations of Seyfert 2 galaxies to find those that have sub-solar metallicities. Out of a sample of around 23,000 they found only $\sim$40 candidates based on optical line ratios from the NLR. The authors suggest that most AGN are only observed after periods of intense star formation in their host galaxies and so the infalling gas supplying the central engine is already abundant with heavy elements. This implies that AGN with inherently sub-solar metals may somehow be feeding off gas that has yet to be processed by stars. It could be that HE 0436 has an unusually low star formation rate for its redshift and/or less Type 1a supernovae to produce iron. Another possibility is that low-metallicity gas from outside of the galaxy has made its way to the central black hole either through a merger or filament, as in the scenarios proposed to explain the unusually low abundances in the NLR of radio-quiet quasar HE 2158-0107 (Husemann et al. 2011).

Other Seyfert 1 galaxies in particular have been known to show sub-solar iron abundances, such as NGC 4593 (Reynolds et al. 2004), NGC 3227 and 4051 (Patrick et al. 2012), and MCG+8-11-11 (Bianchi et al. 2010). Patrick et al. (2012) suggest that a persistently low abundance could represent a component of the Fe Kα line originating from a Compton thin material such as the BLR or NLR. The BLR was ruled out as a possible origin for the broad iron line in HE 0436 (Section 3.2). A narrow iron feature from a distant reflector is required to describe the data and while the narrow line could originate from the NLR, it is unlikely that such a significant fraction of the radiation originates from the region (e.g. Kaspi et al. 2002, Fukazawa et al. 2011).

Perhaps the intrinsic amount of iron in the central engine is not sub-solar, but the amount of other metals higher, since the abundance of other metals in the spectral models is fixed at their respective solar values. The iron abundance in this object is low enough, however, that the other metals in the system would have to be super-solar in order to account for the apparent lack of iron. It is a challenge to determine a mechanism that would substantially increase other metals in a gas without affecting the iron, although a lack of Type Ia supernovae (mentioned previously) may do this. More specifically, an decrease in the ratio between Type Ia/Type II supernovae could decrease the relative abundance of iron as both produce the heavy metals that decay into iron, however Type

Ia more efficiently disperse material into the surrounding interstellar medium (i.e. no supernova remnant remains).

The possibility of HE 0436 having intrinsic sub-solar iron abundance is intriguing as such objects are so rare. Deep analysis of the host galaxy would help to further constrain the metallicity of this object and also advance understanding of AGN-host relations.

7.3 Conclusions

To summarize, the X-ray spectra of Seyfert 1 galaxy HE 0436-4717 includes a broad Fe Kα feature and modest soft excess. The iron feature was determined to contain at least one narrow line originating from a distant, neutral source like the torus while the broad iron component cannot originate from the BLR. Both a partial covering scenario and reflection interpretation describe the X-ray data well and deeper analyses were considered to determine if one scenario is more appropriate than the other for this object.

A partial covering model provides a good fit to the X-ray spectra, but the predicted flux that would accompany such absorption in both the iron and high-energy bands are not seen. The total flux of the observed Fe Kα feature is not enough to attribute the source to remitted absorption predicted with partial covering. A search for absorption edges in the soft band did not find any significant features. The lack of absorption signatures in this object suggest HE 0436 is a "bare" Seyfert 1 galaxy: one with low to no intrinsic extinction. Such AGN have been noted before (e.g. Vaughan et al. 2004, Emmanoulopoulos et al. 2011) and most recently have become the subject of larger sample studies (Patrick et al. 2011, Walton et al. 2013). Bare Seyfert galaxies offer an unobstructed view of the AGN central engine and are invaluable in efforts to better understand the physics behind AGN emission.

A reflection model also provides a good fit to the X-ray spectra and seems to be a better interpretation for this object overall. The broadband reflection component can describe the moderate soft excess and iron line feature well and, if extrapolated to higher energies, agrees with BAT

observations. The spectral and temporal analyses indicate that HE 0436 is in a power law-dominated spectral state where short-term variability is driven by changes in the primary emitter.

Further work must be done on HE 0436 to account for a few discrepancies, most notably the object's apparent low iron abundance, but also the possibility of other X-ray features that are unable to be resolved in current data. A variety of spectral models were tested in this work and, while informative, they are also limited. More high-quality data would be necessary, however, to constrain parameters like black hole spin. Longer, pointed observations with *XMM-Newton* would also advance timing studies by providing multiple epochs of $\sim$200 ks like the variable XMM2. Lag analysis could then be justified as well and might not only confirm the source of X-ray variability but provide an estimate to the scale of the emitting region.

Finally, the new generation of X-ray telescopes such as *Astro-H* (Takahashi et al. 2013) will be able to expand high-energy spectra into the gamma-ray regime and provide observations that may break the degeneracy between reflection and absorption scenarios described previously. The effort is already underway for intermediate- type AGN NGC 1365 (Risaliti et al. 2013, Miller & Turner 2013) using recent observations by *NuStar*. *Astro-H*, predicted to launch in late 2015, is expected to have comparable sensitivity to *NuStar* at 40 keV ($3\times10^{-8}\mathrm{ph\,cm^{-2}\,s^{-1}}$) with a wider field of view above 80 keV and more soft-band sensitivity ("*Astro-H Quick Reference*"[1]). Both telescopes will be able to provide an unprecedented look at AGN spectra beyond the Compton hump and could reveal the true nature of objects such as HE 0436-4717.

[1] http://astro-h.isas.jaxa.jp/ahqr.pdf

Bibliography

[1] Adelman-McCarthy J. K., Agüeros M. A., Allam S. S., et al. 2008, ApJSS 175, 297.

[2] Anderson S. F., Voges W., Margon B., et al. 2003, AJ 126, 2209.

[3] Augusto P., Gonzalez-Serrano J. I., Gizani N. A. B. et al. 2001, AApTr 20, 275.

[4] Avni Y. & Tananbaum H. 1982, ApJ 262, L17.

[5] Ballantyne D. R., Vaughan S., Fabian A. C. 2003, MNRAS 342, 239.

[6] Barth A. J., Greene J. E., Ho L. C. 2005, ApJ 619, L151.

[7] Baumgartner W. H., Tueller J., Markwardt C. B., et al. 2012, ApJSS in process [arXiv:1212.3336]

[8] Bianchi S., De Angelis I., Matt G., et al. 2010, A&A 522, A64.

[9] Blaes O., Krolik J. H., Hirose S., et al. 2011, ApJ 733, 110.

[10] Boyer S., Lampton M., Lewis J., et al. 1996, ApJ Sup. 102, 129.

[11] Brandt W. N. & Hasinger G. 2005, ARA&A 43, 827.

[12] Brandt N., & Podsiadlowski P. 1995, MNRAS 274, 461.

[13] Brenneman L. W., Reynolds C. S. 2006, ApJ 652, 1028.

[14] Burrows D. N., Hill J. E., Nousek J. A., et al. 2000, Proc. SPIE 4140, 64.

[15] Cappi M., Tombesi F., Bianchi S., et al. 2009, A&A 504, 401.

[16] Carroll B. W. & Ostlie D. A., *An Introduction to Modern Astrophysics*, 2nd Edition. Pearson Addison-Wesley, 2007.

[17] Chevallier L., Collin S., Dumont A. M., et al. 2006, A&A 449, 493.

[18] Christian D. J., Craig N., Cahill W., et al. 1999, AJ 117, 2466.

[19] Clavel J., Boksenberg A., Bromage G. E. et al. 1990, MNRAS 246, 668

[20] Crummy J., Fabian A. C., Gallo L., et al. 2006, MNRAS 365, 1067.

[21] Cusumano G., La Parola V., Segreto A., et al. 2010, A&A 524, id.A64.

[22] Czerny B., Nikołajuk M., Różańska A., et al. 2003, A&A 412, 317.

[23] D'Onofrio M., Marziani P., Sulentic J. W. *Fifty Years of Quasars*. Springer-Verlag, Berlin Heidelberg, 2012.

[24] Dauser T., Wilms J., Reynolds C. S., et al. 2010, MNRAS 409, 1534.

[25] Davis S. W. & Laor A. 2011, ApJ 278, 19.

[26] Done C., Davis S.W., Jin C., et al. 2012, MNRAS 420, 1848.

[27] Done C., Jin C., Middleton M., et al. 2013, MNRAS in process [arXiv:1306.4786]

[28] Edelson R., Turner T. J., Pounds K., et al. 2002, ApJ 568, 610. (E02)

[29] Elvis M., Plummer D., Schachter J., et al. 1992, ApJS 80, 257.

[30] Elvis M., Wilkes B. J., McDowell J. C., et al. 1994, ApJS 95, 1.

[31] Emmanoulopoulos D., Papadakis I. E., McHardy I. M., et al. 2011, MNRAS 415, 1895.

[32] Fabian A. C., Rees M. J., Stella L., et al. 1989 MNRAS 238, 729.

[33] Fan X., Strauss M. A., Schneider D. P., et al. 1999, AJ 188, 1.

[34] Fender R. & Belloni T. 2012, Science 337, 540.

[35] Ferland G. J. & Osterbrock D. E. 1986, ApJ, 300, 658.

[36] Fukazawa Y., Hiragi K., Mizuno M. 2011, ApJ 727, 19.

[37] Gallo L.C. 2006, Astron. Nachr. 327, 1076.

[38] Gallo L. C. 2011, Journal of RASC, 105, 143.

[39] Gallo L.C., Fabian A. C., Grupe D., et al. 2013, MNRAS 428, 1191.

[40] Gallo L. C., Tanaka Y., Boller Th., et al. 2004, MNRAS 353, 1064.

[41] Garofalo D. 2009, ApJ 699, 400.

[42] Gehrels N., Chincarini G., Giommi P., et al. 2004, ApJ 611, 1005.

[43] Ghez A. M., Becklin E., Duchjne G., et al. 2003, ANS 324, 527.

[44] Ghisellini G., Haardt F., Matt, G. 2004, A&A 413, 535.

[45] Giacconi R., Gursky H., Paolini F. R., et al. 1962, Phys. Rev. Lett. 9, 439.

[46] Giacconi R., Kellogg E., Gorenstein P., et al. 1971, ApJ 165, L27.

[47] Gierliński M. & Done C. 2004, MNRAS 349, L7.

[48] Grazian A., Omizzolo A., Corbally C., et al. 2002, AJ 124, 2955.

[49] Greene J. E. & Ho L. C. 2004, ApJ 610, 722.

[50] Groves B. A., Heckman T. M., Kauffmann G. 2006, MNRAS 371, 1559.

[51] Grupe D., Beuermann K., Thomas H. C., et al. 1998, A&A 330, 25.

[52] Grupe D., Komossa S., Leighly K. M., et al. 2010, ApJS 187, 64. (G10)

[53] Guainazzi M., Bianchi S., Dovčiak M. 2006, Astron. Nachr. 327, 1032.

[54] Halpern J. P. 1984, ApJ 281, 90.

[55] Halpern J., Marshall H. L. 1996, ApJ 464, 760.

[56] Hamann F., Korista K. T., Ferland G. J., et al. 2002, ApJ 564, 592.

[57] Häring N. & Rix H. W. 2004, ApJ 604, L89.

[58] den Herder J. W., Brinkman A. C., Kahn S. M., et al. 2001, A&A 365, L7.

[59] Hubeny I., Blaes O., Krolik J. H., et al. 2001, ApJ 559, 680.

[60] Husemann B., Wisotzki L., Jahnke K., et al. 2001, A&A 535, A72.

[61] Hynes R. I. & Britt C. T. 2012, ApJ 755, 66.

[62] Iwasawa K., Miniutti G., Fabian A. C. 2004, MNRAS 335, 1073.

[63] Janiuk A., Czerny B., Madejski G. M. 2001, ApJ 557, 408.

[64] Jansen F., Lumb D., Altieri B., et al. 2001, A&A 365, L1.

[65] Kalberla P. M. W., Burton W. B., Hartmann D., et al. 2005, A&A 440, 775.

[66] Kaspi S., Brandt W. N., George I. M. 2002, ApJ 574, 643.

[67] Kellerman K. I., Sramek R., Schmidt M, et al. 1989, AJ 98, 1195.

[68] King A. R., Lubow S. H., Ogilvie G. I., et al. 2005, MNRAS 363, 49.

[69] King A. L., Miller J. M., Raymond J., et al. 2013, ApJ 762, 18.

[70] King A. R., Pringle J. E., Hofmann J. A. 2008, MNRAS 385, 1621.

[71] Kormendy J. & Richstone D. 1995 ARA&A 33, 581.

[72] Krolik, *Active Galactic Nuclei*, Princeton University Press, 1999.

[73] Kubota A, Done C. 2004, MNRAS 353, 980.

[74] Laor A. 1991, ApJ 376, 90.

[75] Laor A. 2006, ApJ 643, 112.

[76] Lawrence A. & Elvis M. 1982, ApJ, 256, 410.

[77] Longinotti A. L., Krongold Y., Kriss G. A., et al. 2013, ApJ 766, 104.

[78] Lumb D. H., Schartel N., Jansen F. A. 2012, Opt. Eng. 51(1).

[79] Magdziarz P., Blaes O. M., Zdziarski A. A., et al. 1998, MNRAS 301, 179.

[80] Magdziarz & Zdziarski 1995, MNRAS 273, 837.

[81] Magorrian J., Tremaine S., Richstone D., et al. 1998, AJ 115, 2285.

[82] Mahony E. K., Croom S. M., Boyle B. J., et al. 2010, MNRAS 401, 1151.

[83] Marconi A. & Hunt L. K. 2003, ApJ 589, L21.

[84] Middleton M., Done C., Gierliński M. 2007, MNRAS 381, 1426.

[85] Middleton M. J., Miller-Jones J. C. A., Markoff S. et al. 2013, Nature 493, 187.

[86] Miller J. M. 2007, Annu. Rev. A&A, 45, 441.

[87] Miller J. S., Goodrich R. W., Mathews W. G. 1991, ApJ 378, 47.

[88] Miller L. & Turner T. J. 2013, ApJ Letters in process [arXiv:1303.4309] (MT13)

[89] Mineshige S., Kawaguchi T., Takeuchi M., et al. 2000, PASJ 52, 499.

[90] Miniutti G., Brandt W. N., Schneider D.P., et al. 2012, MNRAS 425, 1718.

[91] Miniutti G. & Fabian A. C. 2004, MNRAS 349, 1435.

[92] Mitsuda K., Bautz M., Inoue H., et al. 2007, PASJ 59, 1.

[93] Mlodinow L., *Feynman's Rainbow: a search for beauty in physics and life*, Vintage Books, NY, 2003.

[94] Moderski R. & Sikora M. 1996, A&AS 120, C591.

[95] Müller-Sánchez F., Prieto M.A., Hicks E. K. S., et al. 2011, ApJ 739, 69.

[96] Nandra K., O'Neill P. M., George I. M., et al. 2007, MNRAS 382, 194.

[97] Netzer H. 2008, NewAR 52, 257.

[98] Novikov I.D. & Thorne K.S.,"Astrophysics of Black Holes," in *Black Holes*, Eds. C. DeWitt & B. DeWitt (Gordon and Breach, Paris, 1973), pp. 343-450.

[99] Osterbrock D. E. 1978, *Symposium on Quasars and Active Nuclei of Galaxies*, Physica Scripta, 17, 285.

[100] Osterbrock D. E. 1984, QJRAS 25, 1.

[101] Patrick A. R., Reeves J. N., Porquet D., et al. 2011, MNRAS 411, 2353.

[102] Patrick A. R., Reeves J. N., Porquet D., et al. 2012, MNRAS 426, 2522.

[103] Peterson B. M. 1993, ASP, 105, 247.

[104] Peterson B. M., *An Introduction to Active Galactic Nuclei*, Cambridge University Press, 1997.

[105] Peterson B. M. 2006, Lect. Notes Phys. 693, 77.

[106] Ponti G, Cappi M., Dadina M., et al. 2004, A&A 417, 451. (P04)

[107] Porquet D., Reeves J. N., O'Brien P., et al. 2004, A&A 422, 85.

[108] Predehl P.& Schmidt J. H. M. M. 1995, A&A 293, 889.

[109] Reynolds C. S., Brenneman L. W., Wilms J., et al. 2004, MNRAS 352, 205.

[110] Reynolds C. S. & Nowak M. A. 2003, Phys. Rep. 377, 389.

[111] Risaliti G., Harrison F. A., Madsen K. K., et al. 2013, Nature 494, 449.

[112] Ross R. R. & Fabian A. C. 2005, MNRAS 358, 211.

[113] Ross R. R., Fabian A. C., and Young A. J. 1999, MNRAS 306, 461.

[114] Rowan-Robinson 1977, ApJ, 213, 635.

[115] Sanders D.B., Phinney E. S., Neugebauer G., et al. 1989, ApJ, 347, 29.

[116] Saxton R. D., Read A. M., Esquej P., et al. 2008, A&A 480, 611.

[117] Schödel R., Ott T., Genzel R., et al. 2002, Nature 419, 694.

[118] Seyfert Carl K. 1943, ApJ 97, 28.

[119] Shakura N.I., Sunyaev R. A. 1973, A&A 24, 337.

[120] Sippel A. C. & Hurley J. R. 2012, MNRAS 430, L30.

[121] Snowden, S. L., Kuntz, K. D. *Cookbook for Analysis Procedures for XMM-Newton EPIC MOS Observations of Extended Objects and the Diffuse Background*, 2011, v. 4.3. (http://heasarc.gsfc.nasa.gov/docs/xmm/xmmhp_xmmesas.html)

[122] Storchi-Bergmann T., Schmitt H. R., Calzetti D., et al. 1998, AJ 115, 909.

[123] Strüder L., Briel U., Dennerl K., et al. 2001, A&A 365, L18.

[124] Takahashi T., Uchiyama Y., Stawarz Ł. 2013, Aph 43, 142.

[125] Tatum M.M., Turner T. J., Miller L., et al. 2013, ApJ 762, 80.

[126] Tran H. D., Miller J. S., Kay L. E. 1992, ApJ 397, 452.

[127] Tremaine S., Gebhardt K., Bender R., et al. 2002, ApJ 574, 740.

[128] Tremonti C. A., Heckman T. M., Kauffmann G., et al. 2004, ApJ 613, 898.

[129] Trümper J. 1991, Physikalische Blätter 47, 29.

[130] Tucker W. H. & Giacconi R. 1980, Astronautics and Aeronautics 18, 30.

[131] Turner M. J. L., Abbey A., Arnaud M., et al. 2001, A&A 365, L27.

[132] Turner T. J. & Miller L. 2009, A&ARv 17, 47.

[133] Turner J. J. & Pounds K. A. 1989, MNRAS 240, 833.

[134] Urry M., "The AGN Paradigm for Radio-Loud Objects", in *Active Galactic Nuclei: from Central Engine to Host Galaxy*, meeting held in Meudon, France, July 23-27, 2002, Eds. S. Collin, F. Combes and I. Shlosman. ASP Conference Series, Vol. 290, pp. 2-12.

[135] Vagnetti F., Antonucci M., Trevese D. 2012, A&A 550, 12.

[136] Vagnetti F., Turriziani S., Trevese D., et al. 2010, A&A 519, 16.

[137] Vasudevan R. V. & Fabian A. C. 2009, MNRAS 392, 1124.

[138] Vasudevan R. V., Mushotzsky R. F., Winter L. M., et al. 2009, MNRAS 399, 1553. (V09)

[139] Vaughan S., Fabian A. C., Ballantyne D. R., et al. 2004, MNRAS 351, 193.

[140] Volonteri M., Madau P., Quataert E., et al. 2005, ApJ 620, 69.

[141] Walter R., Fink H. H., 1993, A&A 274, 105.

[142] Walton D. J., Nardini E., Fabian A. C., et al. 2013, MNRAS 428, 2901.

[143] Wandel A., Peterson B. M., Malkan M. A. 1999, ApJ, 526, 579.

[144] Wang T., Otani C., Cappi M., et al. 1998, MNRAS 293, 397.

[145] Warwick R. S., Saxton R. D., Read A. M. 2012, A&A 548, 15.

[146] Weisskopf M. C., Brinkman B., Canizares C., et al. 2002, ASP 114, 1.

[147] Wilkins D. R. & Fabian A. C. 2011, MNRAS 414, 1269.

[148] Wilkins D. R. & Fabian A. C. 2012, MNRAS 424, 1284.

[149] Wilson A. S., Braatz J. A., Heckman T. M., et al. 1993, ApJ 419, L61.

[150] Wisotzki L., Christlieb N., Bade N., et al. 2000, A&A 358, 77.

[151] Wolter H. 1952, Ann. Physik. 10, 94.

[152] Zhong X. & Wang J. 2013, ApJ 773, 9.

[153] Zoghbi A., Fabian A. C., Gallo L. C. 2008, MNRAS 391, 2003.

[154] Zoghbi A., Fabian A. C., Uttley P., et al. 2010, MNRAS 401, 2419.

Websites:

http://astro-h.isas.jaxa.jp/ahqr.pdf

http://chandra.si.edu/

http://cxc.harvard.edu/ciao/index.html

http://heasarc.gsfc.nasa.gov/docs/xte/Snazzy/snazzy_sci.html

http://heasarc.gsfc.nasa.gov/Tools/w3pimms.html

https://heasarc.gsfc.nasa.gov/xanadu/xspec/models/optxagn.html

http://heasarc.nasa.gov/docs/swift/about_swift/bat_desc.html

http://swift.gsfc.nasa.gov/docs/swift/results/bs70mon/

http://www.astro.ucla.edu/∼wright/CosmoCalc.html

http://www.sdss.org

http://www.x-ray-optics.de

http://xmm.esac.esa.int

http://xweb.nrl.navy.mil